OPTICAL OBSERVATIONS OF CRITICAL IONIZATION VELOCITY CHEMICAL RELEASES IN THE IONOSPHERE: THE ROLE OF COLLISIONS

A
THESIS

Presented to the Faculty
of the University of Alaska Fairbanks

in Partial Fulfillment of the Requirements
for the Degree of

Doctor of Philosophy

By

Donald Loyd Hampton, B.S., M.S.

Fairbanks, Alaska

May 1996

OPTICAL OBSERVATIONS OF CRITICAL IONIZATION VELOCITY CHEMICAL RELEASES IN THE IONOSPHERE: THE ROLE OF COLLISIONS

By

Donald Loyd Hampton

RECOMMENDED:

Advisory Committee Chair

Department Head

APPROVED:

Dean, School of Natural Sciences

Dean of the Graduate School

3-11-96

Date

Abstract

In recent years researchers have pointed out the importance of collisional processes in ionospheric chemical releases performed to study Alfvén's critical ionization velocity effect (CIV). Ionizing collisions, including charge exchange with ambient O^+, and associative ionization, can not only help initiate CIV, but can also lead to 'contamination' of the ion cloud. Most of the proposed collisions have associated emissions which should be observable with sensitive detectors, but until now have not been attempted since atomic processes had not been considered important.

The first four releases of the CRRES satellite were performed to study CIV. The releases were at local dusk over the south Pacific in September, 1990, and were observed from two aircraft with low light level cameras, both filtered and broadband. Ion inventories of the releases show ionization yields (number of ions per number of available neutrals) of 0.02% for Sr, 0.15% for the first Ba release, 0.27% for Ca and 1.48 for the second Ba release.

The release clouds were seen to glow quite strongly, *below the terminator*. The measured light is found to be primarily from line emissions which indicates that it is due to collisional processes in the release cloud. Two measurements were made on the release cloud data; 1) the absolute intensity of the release clouds and 2) the ratio between a broadband intensified CCD (ICCD) and an imaging photon detector filtered for the Ba^+ 455.4 nm emission line. The measured ratio is compared to the expected ratio for charge exchange collisions, and to electron impact excitation of Ba. The measured ratio is consistent with emissions being from charge exchange collisions. However, when compared to the total intensity of emissions expected from charge exchange, the absolute intensity in the release cloud measured by the ICCD is five times greater. The two measurements are in conflict, and with this limited set of data cannot be fully resolved. The ratio measurement does indicate that any CIV discharge in the Ba releases was extremely weak, and that charge exchange is the dominant collisional process in Ba releases.

Contents

List of Figures

List of Tables

Acknowledgements

There are many people who have helped me with my thesis and in my graduate career. First an foremost is my committee. To Hans Nielsen I owe especial thanks for encouraging participation in a broad range of research. He not only had the courage to trust me to finish my task at hand, but saw how the different experiences would only broaden my education. I hope it is not too forward to consider that our working relationship is also an honest friendship as well. To Gene Wescott I owe many thanks for giving me the chance to participate in many of the different experiments. Gene showed me that hard work and persistence pay off in the end. I would like to thank Tom Hallinan for a thorough reading of the thesis and many helpful comments. To Roger Smith I also owe thanks for the opportunity to work on so many instruments and projects. A hearty thanks to Joe Hawkins for his support and good comments on the thesis. I would also like to especially thank Dave Sentman for providing me with the opportunity to be involved as a major player in a very exciting new field. I thank him for his support and promotion, as well as sitting in on the committee at the last minute, with very little warning.

The list of colleagues and friends at the GI is very long, and I hope that any omissions are not seen as a slight. To the older... uh, more experienced crowd, Joe Minow, Nettie Labelle-Hamer, Jim Conner, Bill Bristow, and others, thanks for a pleasant introduction to graduate life and the GI. To the newer crowd, Peter Delamere, Curt Szuberla, Matt Heavner, their partners and friends, thanks for still talking to the old man in the office, and keeping me young at heart.

To Anne, the thanks I feel are hard to put into words. I hope I can give enough hugs in the rest of our lives to make up for all your support and devotion. Thanks to the animals for providing me with something to do with all my spare time at home, and to the memory of Fat Cat, Rodent and Camorra. Thanks to our families, who took a keen interest in my progress – something that families don't always do.

I would like to thank the Fischer ski company, Black Diamond Equipment Corp., and the Merrell Boot Company for saving me untold money on psychiatrist bills.

The Road goes ever on and on
Down from the door where it began.
Now far ahead the Road has gone,
And I must follow, if I can,
Pursuing it with eager feet,
Until it joins some longer way
Where many paths and errands meet.
And whither then? I cannot say.

J. R. R. Tolkein

The Fellowship of the Ring

Chapter 1

Introduction

This thesis is an examination of experimental evidence for a phenomenon termed critical ionization velocity (CIV). The current theories of CIV are explanations of the hypothesis first proposed by *Alfvén* [1954] as part of a theory for planetary formation. According to this hypothesis, a neutral gas traveling with bulk velocity v through a magnetized plasma will experience ionization when the individual gas particle's kinetic energy perpendicular to the magnetic field ($K_\perp = mv_\perp^2/2$) exceeds its ionization potential. For a gas composed of particles with ionization potential ϕ_i and mass m the critical ionization velocity is defined as

$$v_{cr} = \sqrt{\frac{2e\phi_i}{m}} \tag{1.1}$$

By Alfvén's hypothesis, the gas will undergo spontaneous ionization when $v_\perp \geq v_{cr}$

While not specifying the exact mechanism by which the neutral gas would ionize, Alfvén did note that electrons are far more efficient at ionizing neutrals than are ions, and suggested that the free kinetic energy of the neutrals would go into heating electrons to energies at which they could ionize the neutral gas by collisions [*Alfvén*, 1954, p. 31]. Alfvén's hypothesis as it applies to planetary formation has met with skepticism (see discussion by *Brush* [1990]).

Laboratory experiments to study the CIV effect have generally been successful in demonstrating that Equation (1.1) holds [see, for example *Danielsson*, 1973; *Brenning*, 1992], but fail to satisfy Alfvén's original postulates on two accounts [*Möbius*, 1983]. First, in the laboratory the free energy resides in the accelerated plasma, not in the neutral gas as imagined by Alfvén. Second, there are walls and probes present in the laboratory experiments that would not be present in proto-

Table 1.1 – Ionospheric CIV Chemical Releases

Release	Angle, type[a] and Material	Yield	Reference
Porcupine	35° c Ba	10-30%	*Haerendel*, 1982
Bubble Machine	90° r Ba/Sr	10^{-4}%	*Deehr et al.*, 1982
Star of Lima	90° c Ba	$\leq$ 0.2%	*Wescott et al.*, 1986a
Star of Condor	90° c Sr	$\leq$ 0.36%	*Wescott et al.*, 1986b
CRIT I	45° c Ba	0	*Stenbaek-Nielsen et al.*, 1990a
CRIT II	45° c Ba	3%	*Stenbaek-Nielsen et al.*, 1990b
SR90	45° c Sr	0	*Wescott et al.*, 1990
Active	- gas Xe	0	*Wescott et al.*, 1992

[a]Shaped charges: r = radial, c = conical

planetary space. While great pains have been taken to minimize or to estimate the effects of wall interactions it is uncertain what role these play in the experiments.

In space-based chemical releases the free energy of the system resides in the neutral gas, and the energy or momentum loss to walls is non-existent. To date there have been several chemical releases conducted specifically to test the CIV effect (Table 1). Of the space based releases listed in the table, there have been two with substantial ionization; "Porcupine" [*Haerendel*, 1982], and "CRIT-II" [*Stenbaek-Nielsen et al.*, 1990b; *Torbert et al.*, 1992]. In the latter, *in situ* particle detectors measured substantial fluxes of energetic electrons – further evidence supporting CIV in the early stages of the release. Many others releases have resulted in very little ionization, all of which is attributed to other ionization sources, [*Deehr et al.*, 1982; *Stenbaek-Nielsen et al.*, 1990b; *Wescott et al.*, 1990].

1.1 CIV Theories and Simulations

The current theories of CIV center on the idea that it is a plasma discharge. The external energy available to the system is in the form of the kinetic energy of the neutral gas. However, there must also be some coupling between the streaming neutral gas and the background plasma or magnetic field. If there is no initial ionization of the neutral gas, and the regime is collisionless, then the neutral gas will travel unimpeded at the streaming velocity. If there is some source of ionization in the neutral gas, the difference in gyroradii between the electron and the newly

formed ions will result in a charge separation which will persist for half a gyroperiod and the maximum extent of this separation will be on the order of a gyroradius.

Nearly all theories of CIV involve ionization of the streaming neutrals by a population of energetic electrons [*Brenning*, 1992]. The theories can be divided into two basic sets, based upon the mechanism by which the electrons are energized. The first uses the fact that the separation between the ions and electrons, if it occurs along a well defined front, will produce an electric field. The component of the electric field perpendicular to the magnetic field will cause the electrons to $\mathbf{E} \times \mathbf{B}$ drift. CIV will be initiated if the electron drift energy exceeds the ionization potential of the neutrals. Theories that use this scenario are termed "ionization front" [*Goertz et al.*, 1990] or "inhomogeneous" [*Brenning*, 1992]. The second set of theories involves wave particle interactions to energize the electrons. The most common wave modes are lower-hybrid waves excited by the modified two-stream instability. Initial ionization in the neutral gas produces a plasma streaming with respect to the background plasma which initiates the modified two-stream instability. This instability produces plasma waves in the lower hybrid frequency range which heat electrons parallel to the magnetic field. These electrons collide with the neutral particles which have moved into the heated electron region. These newly created ions will stream through the ambient plasma, further exciting the modified two-stream instability, creating a positive feedback loop. Theories involving this scenario are termed "collective" [*Goertz et al.*, 1990] or "homogeneous" [*Brenning*, 1992].

Much of the early computer simulation work on CIV also concentrated on the mechanism responsible for energizing the electrons, and therefore highlighted the fundamental electrodynamic processes. *Tanaka and Papadopoulos* [1983] simulated unmagnetized ions moving through a background of magnetized electrons which excites several modes of the modified two-stream instability. The same type of simulation was carried out by *Machida et al.* [1984], who were specifically looking for a critical velocity. They added a calculation of the ionization rate of a non-interacting neutral stream moving with the ion stream. *Abe and Machida* [1985] added a stationary background ion plasma to the same type of simulation domain. All three works are seminal in that they show that exciting the modified two-stream instability results in energized electrons and a reduction in the streaming ion energy – both due to wave particle interactions. However, it is difficult to apply the results directly to chemical injection experiments since they are one-dimensional simulations with steady, uniform plasma flow, and periodic boundary conditions.

There is also little attention paid to collisional or other atomic processes, except for a very crude electron impact ionization cross section used by *Machida et al.* [1984]

The importance of collisional processes was introduced in the simulations of *Machida and Goertz* [1986, 1988]. They included effects from charge stripping, charge exchange and electron impact collisions. By including collisions they were able to outline a new CIV regime, termed resistive CIV, which is collisionally dominated rather than resulting from collective plasma effects. *Biasca et al.* [1993] and *Moghaddham-Taaheri and Goertz* [1993] also included collisions in their models of specific ionospheric release experiments. *Biasca et al.* [1993], while limited by the simplifications required for 1-D particle-in-cell (PIC) techniques, were able to adjust parameters so that they could place upper limits on the ion production rates for several specific ionospheric CIV releases. They found that the release experiments carried out were not large enough to support a fully developed CIV process. However, small amounts of ionization and electron energization would result, in reasonable agreement with most of the experiments. The exception is the "Porcupine" experiment in which more ionization was observed than can currently be explained, and thus remains the enigma of CIV experiments. *Moghaddham-Taaheri and Goertz* [1993] used a set of quasi-linear equations to examine the evolution of the ion and electron distributions for a CIV reaction. This technique allowed them to use realistic cross sections for electron impact and excitation. They also found a dramatic change in yield by changing the magnitude of the charge exchange cross section. Like *Biasca et al.* [1993] they found, using realistic parameters, that the yields they predicted for several of the chemical releases would result in only small ionization yields due to CIV. These three simulations pointed out the important role atomic and molecular processes play in early times of chemical releases.

1.2 Collisional Processes and Their Importance

In general CIV releases take place at altitudes where the ratio of the ion-neutral collision frequency to the ion gyrofrequency in the *ambient* atmosphere is low. This region is generally termed collisionless [*Kelley*, 1989]. Chemical releases, on the other hand, introduce particle densities that are much greater than the background during the first few seconds of the release. The ambient neutrals and ions that the release cloud engulfs during this early time will now have a high collision frequency with the release material. Some of these collisions result in the ionization of the release material, and change the density of both the neutral and ionized part of the

release cloud. According to CIV theories the growth rate of the plasma instability that heats the electrons will, in large part, be controlled by the density of the ions that are streaming with the neutral release cloud. The rate at which ionizing collisions occur in the early part of the release is therefore decisive in determining the ability of a release to initiate a CIV process [*Lai et al.*, 1992b].

The importance of atomic processes in chemical releases has not gone unnoticed, and several authors have speculated on the relative importance of many atomic processes [*Newell and Torbert*, 1985; *Murad and Lai*, 1986; *Murad*, 1987; *Lai et al.*, 1988, 1989; *Person et al.*, 1990; *McNiel et al.*, 1990; *Swenson et al.*, 1991; *Lai et al.*, 1992a, 1992b]. The collisions that can ionize the neutral release species include electron impact ionization,

$$A + e^- \rightarrow A^+ + 2e^- \tag{1.2}$$

charge stripping,

$$A + B \rightarrow A^+ + B + e^- \tag{1.3}$$

charge exchange,

$$A + B^+ \rightarrow A^+ + B \tag{1.4}$$

and associative ionization,

$$A + B \rightarrow AB^+ + e^- \tag{1.5}$$

$$AB^+ + h\nu \rightarrow A^+ + B \tag{1.6}$$

Collisions that do not directly result in ionization, but which play an important role in the energy budget of a CIV release, include electron impact excitation of allowed transitions,

$$A + e^- \rightarrow A^\dagger + e^- \tag{1.7}$$

$$A^\dagger \rightarrow A + h\nu \tag{1.8}$$

and excitation of metastable states,

$$A + M \rightarrow A^* + M \tag{1.9}$$

where M is any species, including electrons. The reactions are defined in terms of (but not limited to) a chemical release, where A is the release species (generally Ba, Sr, or Ca), and B is an ambient species (usually O).

Collisions are not only important as sources of ionization, but also play a role in the transfer of energy in CIV. Both *McNiel et al.* [1990] and *Newell and Torbert* [1985] stress that the large excitation cross section of Ba neutral lines by

electron impact is an energy drain on any CIV process that is initiated. The energy that for other species might go into ionization by energetic electrons is radiated away by the 553.5 nm line in Ba, and similar lines in Sr and Ca.

Thus, collisions are recognized as playing a more important role in CIV releases than was previously thought. The work on collisions in CIV releases has so far been primarily speculative. Using some unique optical signatures of each collision the relative rates at which the collisions are taking place can be measured. A measurement of this type could help determine the extent to which CIV is happening in a chemical release, something which is not possible when considering the ion inventory alone.

1.3 Measuring Collisional Processes in Chemical Releases

The measurements used in most CIV releases are unable to distinguish among ionization methods. Electric and magnetic field measurements can be used to infer charge distributions, electromagnetic waves, and currents, but there is no unique signature of the atomic processes. Similar arguments apply to particle measurements. Optical methods to date have made use of ion inventories in CIV releases to determine the ionization yield of the release. Again no distinction can be made between ionization mechanisms. The ionization rates must be inferred, or more generally, a total ionization rate is calculated [*Stenbaek-Nielsen et al.*, 1990b].

When a cloud of neutral barium gas is released in sunlight above the atmosphere, it will photo-ionize with a time constant of 28 s [*Carlsten*, 1975; *Hallinan*, 1988]. This means at early times in the release ($t \ll 28$ s) the ion production rate is nearly 4% per second of the initial number of neutrals available. The total yields for the CIV releases listed in Table 1.1 are generally less than 4%. Compared to CIV, solar photo-ionization of Ba releases is a much more efficient process, and for this reason most CIV releases are conducted in the earth's shadow, near the terminator. The barium is released so that ions produced early in the release will move across the terminator into sunlight where they can be observed via one of several resonant emission lines. The release cloud has generally been assumed to be un-observable.

For alkaline-earth chemical releases in the ionosphere, many of the collisions listed in the previous section will have optical emissions associated with them,

some of them with unique signatures. Electron impact excitation and ionization will show certain ratios between emission lines for different electron temperatures. Charge exchange with O^+ will result in an excited state in Ba, Sr, and Ca. The set of emissions as the electron cascades back to its ground state will result in a set of emissions with well defined ratios. With the right instrumentation and viewing conditions, the release cloud could be observed below the terminator, and the relative efficiencies of each process can be measured.

The data collected from four chemical releases from the Combined Release and Radiation Effects Satellite (CRRES) offer an opportunity to study these collisional processes by optical methods. The CRRES satellite carried 24 thermite release cannisters as part of its main mission. The first four releases, in September, 1990, were dedicated to experiments to test CIV in a space setting. Two of the releases were of Ba while the two other releases were of Ca and Sr, respectively. In these experiments, the release cloud were observed for several seconds, *below the terminator*. While the instrumentation was not ideal, the observation of the release clouds make possible a limited set of measurements of the type described above. In this thesis, these measurements are described and used to examine the relative efficiencies of some of the processes.

1.4 Thesis Overview

In the next chapter the CRRES South Pacific chemical release experiments are described including the instruments, data analysis and observations. In Chapter 3 the cross sections for the atomic processes listed above are examined. Those that have been measured are presented, and the uncertainties are listed. Those that have not been measured are either calculated or discussed as to limits. In Chapter 4 the morphologies of the ion clouds as they appear in sunlight are discussed. From this the ion yield of the release is measured as well as time evolution of the ionization, and the ion distribution up the field lines. In Chapter 5 the release clouds, observed with low light level cameras below the terminator, are examined for evidence of collisional processes and CIV. In the concluding chapter the results are further discussed, especially how they relate to theories of CIV, and the interpretation of other space based CIV releases.

Chapter 2

Overview of CRRES CIV Releases

The Combined Release and Radiation Effects Satellite (CRRES) was launched from Cape Canaveral Air Force Station on July 25, 1990 on an Atlas I rocket. The satellite was a joint NASA and USAF project designed to support several experiments [see set of papers introduced by *Vampola*, 1992], including the effects of radiation and particles in space on electronic components, measuring electromagnetic waves and particle populations, and a series of chemical releases in the Earth's magnetosphere and ionosphere. The configuration of the satellite included 24 chemical release cannisters, sixteen of Ba, six with a mixture of Eu and Li, one of Ca and one of Sr. The cannisters were released either individually or in pairs between September, 1990 and August, 1991. The goals of all of the chemical release experiments are described elsewhere [*Bernhardt*, 1992; *Reasoner*, 1992].

The first four experiments were conducted specifically to examine Alfvén's CIV hypothesis (introduced in the Chapter 1, and discussed further in Chapter 6). The requirements for CIV releases are different than for releases performed to observe plasma effects or map magnetic field lines. For field line mapping, the goal is to produce a plasma of a highly visible species. This is achieved for Ba by releasing in sunlight where (above the majority of the earth's atmosphere) UV sunlight will ionize atomic barium gas with a time constant of 28 seconds [*Carlsten*, 1975; *Hallinan*, 1988] or less [*Hoch and Hallinan*, 1993]. For CIV in the ionosphere the ionization time constant is expected to be much longer than 28 seconds, so most of the Ba CIV releases (Porcupine, Star of Lima, and CRIT I and II) have been conducted below the terminator in the earth's shadow to eliminate the much more efficient photoionization. To measure the ionization that does occur, the releases have been oriented such that ions created below the terminator will transit quickly

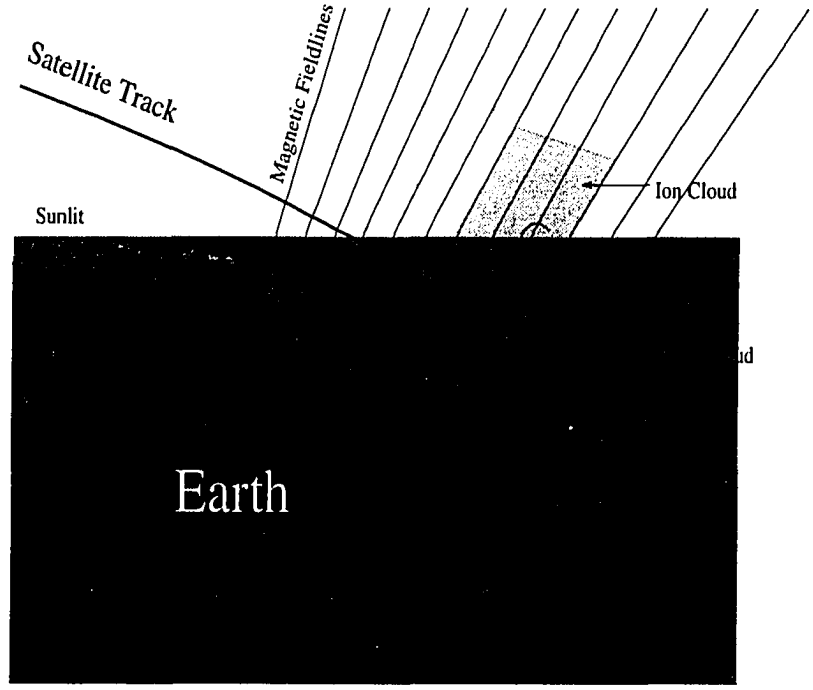

Figure 2.1: A schematic of a CRRES below-the-terminator chemical release. The release occurs in darkness. Any ions created should have a pitch angle such that they will quickly transit into sunlight.

into sunlight where they can be observed by one of several resonant fluorescent emissions (455.4, 493.4 nm are the most intense).

Since the ionization time constant for Sr is on the order of 2000 s, strontium CIV releases have been conducted in full sunlight [*Wescott et al.*, 1990, 1986a]. This has the advantage that all of the ions produced by CIV (or other processes) are available to be detected. For a 'below-the-terminator' release, there may be an unknown fraction of the ions that do not make it into sunlight. None of the Sr rocket releases has produced significant ionization greater than would be expected from solar photoionization (see Table 1.1).

All of the CRRES releases were from thermite cannisters rather than from shaped charges. The reaction, $Ti + 2B \rightarrow TiB_2$ is exothermic and produces sufficient heat to vaporize the release material. For a CIV release a dense neutral gas moving at high speeds ($> v_{cr}$) is needed. For rocket experiments the release

is usually near apogee, when the rocket is relatively slow, so the needed velocity comes from igniting a high velocity shaped charge (radial or conical). For the thermite cannisters on CRRES, the release velocities away from the cannister were low ($\sim$ 2 km/s). The high velocity for the releases comes from the satellite motion near perigee, which is on the order of 10 km/s. A schematic of the CRRES CIV releases is shown in Figure 2.1.

Two pairs of releases, labeled G-13 and G-14, were conducted at local dusk over the South Pacific in September 1990. The G-13 releases occurred on September 10, 1990, near Roratonga, at $\sim$ 515 km altitude, and the G-14 releases occurred on September 14, 1990 west of New Caledonia, at $\sim$ 595 km altitude. The satellite motion was from west to east so that the satellite moved from sunlight into darkness. The release times were staggered by 2.5 seconds for each pair to separate the ion clouds as well as to aid in determining the location of each release. This separation also allowed for some of the analysis of the release cloud brightness, described in Chapter 5. The first release of the first experiment, G-13A, was a Sr release, and the first release of the second experiment, G-14A, was a Ca release. In both experiments, the second releases, G-13B and G-14B were of Ba.

The CRRES CIV releases saw the first use of Ca as a release material. With different ionization potentials and masses, the critical velocities for both Sr and Ca are somewhat different than that for Ba (5.4 km/s and 3.5 km/s for Ca and Sr, respectively, compared to 2.7 km/s for Ba). Thus the three different materials made for a fairly wide range of parameters for the releases. Sr has been used in CIV releases before, both as a dopant in the Ba liner in shaped charges [*Deehr et al.*, 1982], and as the primary metal in the release [*Wescott et al.*, 1986a, 1990]. But, until CRRES a full Sr release had never been conducted at the same time, and therefore under the same ionospheric conditions, as a Ba release.

2.1 Instrumentation

The original experimental design (based primarily on the Porcupine results) anticipated significant ionization. Therefore no consideration was given to detecting processes leading to ionization less than 1%. Further, all of the ionization was assumed to be from CIV, with little consideration given to competing collisions. Therefore the instrumentation was designed to measure ion inventories from each release.

The primary measurements for the releases came from low light level cameras. The data were collected from two aircraft, an Air Force KC-135 from the 4950th test wing, Wright-Patterson AFB, Dayton, OH, and a Learjet from Aeromet Inc, Tulsa, Oklahoma. Each aircraft had an intensified CCD camera (ICCD), and an imaging photon detector (IPD). Each of these camera systems was mounted on a stabilized platform to compensate for aircraft motion. There was an additional unfiltered intensified SIT camera on the KC-135.

ICCD

The ICCD system uses a third generation image intensifier to increase the signal to levels that can be recorded using a CCD TV camera. A primary large-aperture lens focuses the image onto the front of the image intensifier. The image from the back of the intensifier is focused and reduced to fit onto a CCD camera via a set of relay lenses. The intensifier was chosen so that its spectral response was enhanced in the blue in order to improve the detectability of the Ca^+ emission lines. The analog output of the CCD was recorded on video tape (primary 3/4" U-matic, backup VHS). Both systems had a removable filter system. When unfiltered, each camera was run at TV frame rates (30 frames, interlaced, per second), and when filtered, was run in integration mode, and recorded to the video tape by a frame storage device. Integrations ranged from 2 to 4 seconds. The field of view is $11° \times 15°$.

IPD

The imaging photon detector (IPD) uses photon counting and position detecting techniques to build up an image photon by photon. It has been described extensively elsewhere [*Rees et al.*, 1981]. A photon strikes a photocathode creating a photoelectron which accelerates through a large ($\approx$ 700 V) electrostatic potential to a set of three microchannel plates. Within the microchannel plates the single electron is amplified into a large number of ($\sim 10^8$) electrons which fall through another large electric potential onto a resistive anode. Measuring the total charge from four leads on the resistive anode, the position of the center of the electron bundle is determined. The electron bundle corresponds to a single photon event and the position on the resistive anode corresponds to the position where the photon hit on the photocathode. The image is stored digitally on computer as well as being backed up by video recording. The field of view is 20°. The cameras were always filtered, primarily with a 455.4 nm filter for the Ba^+ emission line.

2.2 Digital Images: Preparation, Analysis and Uncertainties

The amount of light that is captured in the images for these experiments is small. The low intensity combined with the diffuse nature of many of the release clouds make the signal that will have to be examined look not much different than the noise in the images. It is important to know to what extent this will limit the accuracy of the results.

The data analyzed for this study came in the form of digital images, either video images digitized for analysis, or digital IPD images. A number of artifacts of the recording process will be introduced to the images. These artifacts, or errors, can be categorized as either systematic (vignetting, distortions, differences in sensitivity), or random (noise due to photon counting statistics, instrumental noise). Each will in some way mask the true character of the original object. Most images, as will be seen, have been subject to at least one of each type of error.

2.2.1 Systematic Errors

There are two major systematic errors that must be corrected in this data set; vignetting and filter bandpass effects. Vignetting is the decrease in intensity at increasing incident angle. It is due, in part, to the decrease in effective collecting area of the lens for light off of the optical axis (the line normal to the front of the lens). Vignetting is generally a smoothly varying effect across the image, being proportional to the cosine of the incident angle, and can be approximated with a quadratic best fit to an image of a uniform scene. Ideally this uniform scene should be a uniformly illuminated lambertian screen taken just before or after the data are collected. This was not practical for these experiments since the cameras were only a few inches from the aircraft window which made it difficult to place a lambertian screen that was *uniformly* illuminated in front of the camera inside the aircraft, and it was inconvenient (to say the least) to place a screen outside the airplane. Instead uniform emissions from the sky were used in correcting for vignetting.

The method often called 'flat fielding' was used to correct the vignetting function for the CRRES ICCD images. A best fit 2-D polynomial is found for an average of several images of a uniform sky. This best fit polynomial was then used to create an array of the same dimensions as the image, normalized to its maximum value. Each image that was analyzed was divided by this array (pixel by pixel).

The filter bandpass correction is not as straightforward to calculate as vignetting. The bandpass of an interference filter changes with incident angle of the light passing through it. The center wavelength changes toward shorter wavelengths and the width of the bandpass increases. This means that for a camera system whose first element is an interference filter (such as the IPDs, and ICCD), the bandpass at the center of the image is different than the bandpass at the edge of the image. The actual form of the relationship is fairly complicated when considering the detailed parameters of the filter construction. A parameterized formula for the change in center wavelength of the filter bandpass is found to be $d\lambda = -P\theta^2/2$, where θ is the incident angle from the surface normal of the filter, and P is a parameter related to the construction of the filter [*Blifford*, 1966; *Eather and Reasoner*, 1969]. The change in width has no simple relationship and is generally specific to each filter [*Eather and Reasoner*, 1969]. The bandpass center is also affected by the temperature of the filter.

The filter bandpass effect is most apparent in the filtered IPD images of the G-14 release ion cloud, but is also seen in the G-13 IPD images. No bandpass effects are seen in the ICCD images, probably due to the low intensity of the Sr ion cloud, and the broader bandpass of the Ca filters. The Ba filter bandpass was designed so that at normal incident angle the 455.4 nm Ba^+ line would be at the blue end of the flat top of the bandpass function. Conditions in the plane, probably the temperature, changed the filter bandpass so that it was slightly red of the 455.4 nm line, and at normal incidence the transmission was less than the maximum of $\sim$ 60%, seen in Figure 2.2 for the change in center wavelength with incident angle. At increasing incidence angle, the bandpass shifts to the blue so that the ion line is now in the peak transmission region of $\sim$ 60%. Near the edge of the images the filter bandpass shifts so far that the 455.4 nm line is now on the red end of the filter bandpass. This creates a 'doughnut' shaped ring of high transmission with lower transmission near the center and around the edges.

To correct for this effect, the transmission of the 455.4 nm emission line through the filter had to be calculated as it would be seen in the images. Since there are too many free parameters for an analytical determination, a best-fit method was used varying only the center wavelength of the filter bandpass. The change in the width of the bandpass is not known, and it was found that using only the wavelength shift, most of the error could be corrected. The method was possible based on a pair of images, 30 seconds apart, for which the viewing azimuth had changed horizontally by about 1/3 of the images size, with little change in the

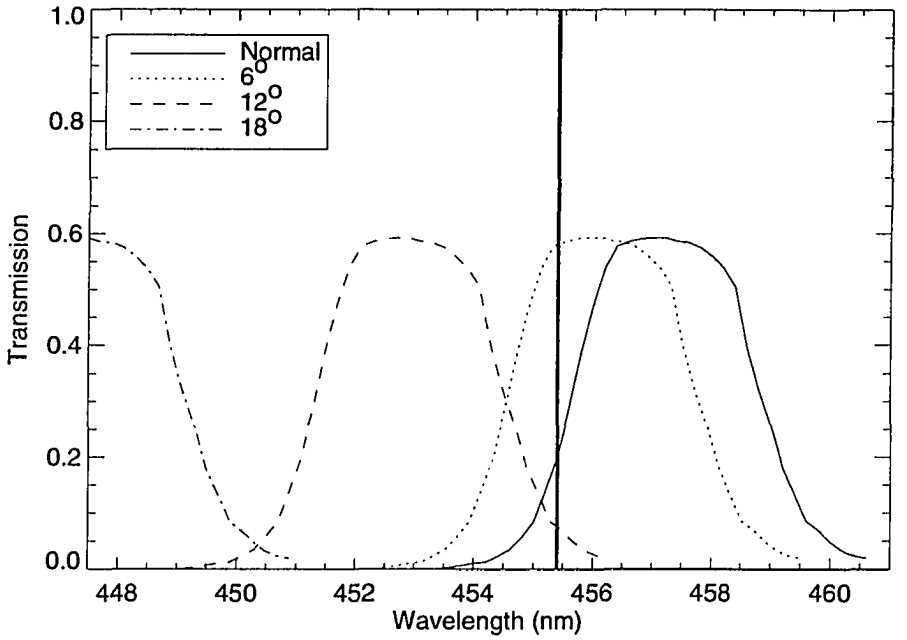

Figure 2.2: Change in bandpass center with incident Angle. The manufacturer's curve for the Ba^+ filter, for normal incidence, is shown shifted to different incident angles. In this plot only the bandpass center is shifted, the width is not adjusted. The 455.4 nm line is shown as the thick vertical line. By 12° the bandpass has essentially shifted beyond the emission line.

elevation. The ion cloud development before and after these images proceeded gradually so the change in the real ion cloud profile between the times of the two images is considered negligible. Upon taking horizontal traces of the two images and comparing them, (see Figure 2.3) it is clear that the shift in image has altered the measured profiles considerably.

The form of the correction is calculated by taking the ratio of the two profiles after they have been shifted so that the sharp left edges match, as shown in Figure 2.3. The two shifted image profiles are labeled C_1 and C_2, each one being the product of the true cloud profile, I, and the 455.4 nm transmission function of the filter, T, one of which has been shifted by δ pixels. The ratio of the two image

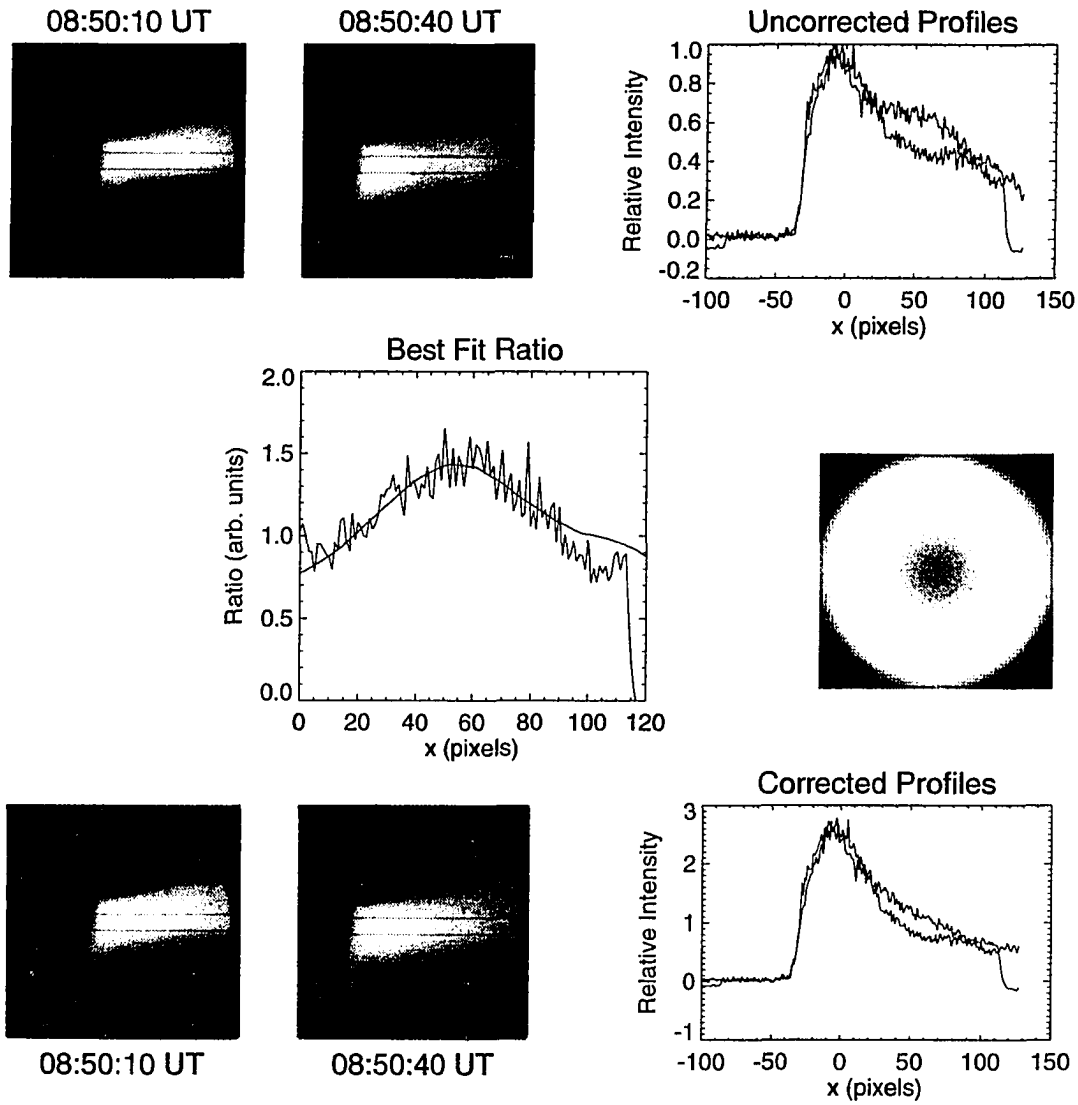

Figure 2.3: Bandpass correction to IPD images. The two images in the upper left are used for the correction. The average profiles from between the two gray lines from the two images, $T(x)$ and $T(x-\delta)$, are compared in the upper right plot. The ratio of the two profiles are shown in the center plot and the bandpass correction based on the best fit is shown center right. The corrected images are shown lower left with the correct profiles shown lower right.

profiles can be written in terms of the 455.4 nm transmission function

$$\frac{C_1}{C_2} = \frac{I_1 T(x)}{I_2 T(x-\delta)} \tag{2.1}$$

With the assumption that the ion cloud profile, I_i, is the same in both images, ($I_1 = I_2$) the problem becomes one of finding the transmission function that, when divided by a shifted version of itself reproduces the ratio of the image profiles, shown in the center of Figure 2.3. The transmission profile was taken from the manufacturer's calibration (Barr and Associates) and the shift was modeled with two free parameters; the center wavelength for normal incident light, and the factor P. The ratios of the non-shifted and shifted transmission profiles was calculated for a range of values of both parameters, and the square difference between this ratio and the image ratio was calculated. The best fit was the set of parameters corresponding to the minimum in the square difference. The results are shown in Figure 2.3.

2.2.2 Random Errors

The digitized images of the data are subject to a component of stochastic error, primarily from photon counting statistics. This is most obvious in scenes near the detection limit of the camera, where the images appear rough or noisy. The IPD images are verifiably subject to photon statistics since each pixel count is a number corresponding to the number of photons measured in that pixel location. There are many more steps leading to the formation of a digitized video image, but it is found that the subsequent electronic transfer of the image from tape to digitized image introduces much less noise than the intensifier tube.

Before discussing the problems with image analysis, the basics of photon, or counting statistics will be outlined. Consider a detector consisting of a single pixel, which is looking at a scene of constant intensity. The detector samples for a time interval Δt and collects m events in that time. If this experiment is replicated many times the result m will vary from experiment to experiment, and the distribution of m is the well known Poisson distribution. The probability of getting m events in time interval Δt is $P(m) = \frac{\lambda^m}{m!} e^{-\lambda}$, where λ is the average number of counts, or the average detection rate multiplied by the time interval ($\nu \Delta T$) [See *e.g. Frieden*, 1991]. There are two well known results for a Poisson distribution. First, the variance in the mean is the square root of the mean, $\sigma_\lambda = \sqrt{\langle m \rangle} = \sqrt{\lambda}$. Second, for high average backgrounds, *i.e.* large λ, the distribution can be approximated

with a gaussian distribution.

In the previous case the distribution was found by taking the results from a single pixel for many experiments, but the same can be done for an array of pixels (a digital image) if the average detection rate for each pixel is the same. This is the case of a camera looking at a uniformly illuminated blank wall (lambertian screen). In this case the multiple experiments are achieved by having multiple pixels sampling during one time interval. The distribution can be found by binning over all the pixels in the image, and again will be Poissonian.

Knowing that a digital image of a uniform surface produces a Poisson distribution in the counts per pixel should allow for a good estimation of the average background count to be subtracted from the image in order to find the total signal from the chemical release. In cases where the surface brightness of the cloud is very low, a good estimation of the background is important since the background signal can be a significant fraction of the total signal in the image. Therefore, it is important to see how well estimation methods work to reproduce a known signal. For this reason a set of tests was conducted on synthetic images of known intensity corrupted by a noisy background.

The synthetic images were each composed of two parts. The first part is the object, or synthetic cloud, which is given the form of a centered radial gaussian function $g(r) = A \exp\left[(r/r_w)^2\right]$ where r is the distance from the center of the image in pixels, r_w is the width of the function in pixels, and A is the maximum amplitude, or brightness of the synthetic cloud. The exact form is not crucial to the analysis, but it does resemble a chemical release cloud as seen by the the cameras. The second part of the synthetic image was a noisy background. Each noisy background was given a mean level λ and gaussian noise with variance $\sqrt{\lambda}$, to simulate a Poisson image. The image size was 200×200 pixels. The synthetic image was the simple pixel by pixel addition of the two parts, as seen in Figure 2.4

Four methods were used, each of which involved estimating the mean background level and subtracting this from the synthetic image. The total count in the resulting image was compared to the total count in the synthetic cloud. The methods differed in how the mean background level was estimated, and include;

1. Using the known background level λ. This can be considered a control to see if the correct mean value returns the correct answer: 'Control'

2. Finding the best fit gaussian function to the histogram of the entire image, and using center of the gaussian as the background level, λ: 'Best

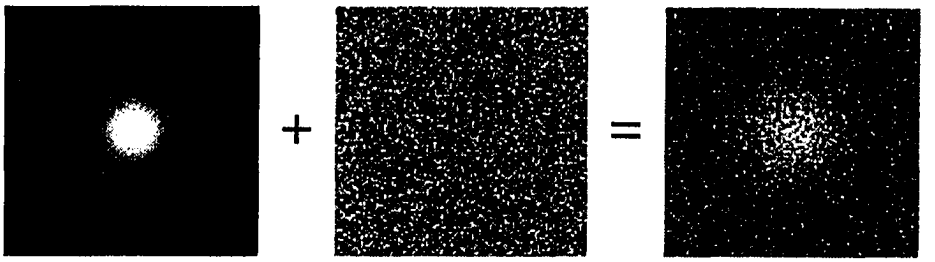

Figure 2.4: Construction of synthetic images. The centered gaussian is seen in the first panel, and the noisy background is seen in the center panel. The synthetic image is a pixel by pixel addition of the two and is shown on the right.

fit'

3. Using four sub-images, one from each corner of the synthetic image, to estimate the mean level of the background. This should have advantages over the other methods in that the corners should not be 'contaminated' by the synthetic cloud and should better represent the background level: 'Corner'

4. Finding the median value of the entire synthetic image, and setting this as the mean background level: 'Median'

For the tests, two parameters were varied, the amplitude A of the synthetic cloud and the mean level of the noisy background, λ. For each set of parameters a synthetic image was created and all four methods were applied. The results for a range of λ are shown for a given amplitude, $A = 25$, in Figure 2.5. It is seen that the control returns a good estimation of the total count from the synthetic cloud, but the other cases generally do not. In these tests the noise is from 10% to 30% of the maximum signal of the synthetic cloud, and away from the center (see Figure 2.4) is comparable to the signal of the synthetic cloud. In most of the analysis to come the signal to noise is much better than this. Only in the cases of the Sr ion cloud in Chapter 4, and the late time of the release clouds in Chapter 5, do the images show similar signal to noise characteristics. In these cases the inability to easily determine the background and therefore the actual counts, as shown in these controlled examples, will be indicated by numerical uncertainties.

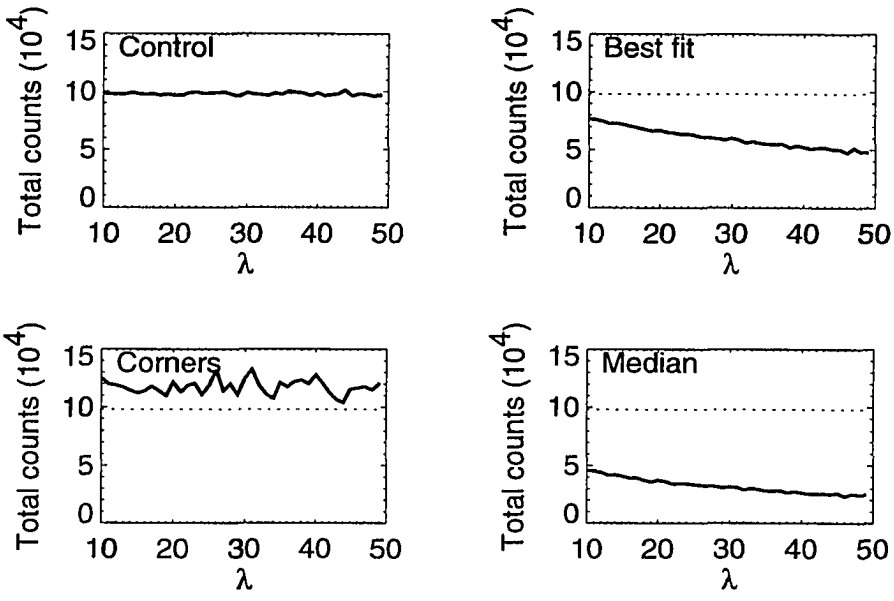

Figure 2.5: Synthetic image test results. The four test discussed in the text are shown. In each panel the dotted line is the actual count from the synthetic cloud. The solid lines are the results for different values of the increasing background level, λ. All test were for a maximum signal from the synthetic cloud, A, of 25.

2.3 General Observations and Data Quality

The planned experimental/observational procedure was as follows. The ephemerides of the satellite were well known and updated by NASA daily, so that the position of the satellite could be predicted accurately. The location where the satellite reached -15 km screening height was calculated. This was set as the release position and the time that it was predicted to occur was set as the release time. It was important to have this predictive capability since the chemical cannisters were ejected from the satellite 25 minutes before the releases occurred. With the release position set, the aircraft flight plans were formulated such that the release and subsequent ion cloud could be observed, given the look angle constraints of the camera mounts in the aircraft. The personnel were given the predicted look angles to the release and ion cloud positions. The final camera positions were verified prior to the release by comparing the observed star field on the real time video image to star maps with

the calculated star fields for the release position. This method worked for all but one of the data sets.

Next are described the observations for each instrument for each pair of releases. The descriptions are to document the data quality and coverage, and to set the stage for the analysis and discussion in the following chapters. The expectation was that, at the time of the release, the escaping B - Ti - metal mixture would be seen as a bright flash (called the burst from here on), localized at the cannister, and then the ion cloud would be seen developing a few 10's of seconds later above the terminator. The observed bursts established a release time, and observations from two planes allowed for triangulation of the release position. What was surprising was that the release clouds were observed, *below the terminator*, for up to 20 seconds after the burst . This result, as well as a second bright neutral Sr cloud, led to some confusion in the observations, and led to some data gaps in the G-13 release ion cloud observations.

2.3.1 G-13

Of the five cameras trained on the G-13 release, four captured the Sr burst at 06:10:22.5 UT. The burst was apparently just out of the field of view of the ICCD on the KC-135. This camera also did not record the Ba burst 2.5 seconds after the Sr burst. The Sr filter was placed on the ICCD at about 06:11:30. Due to the low brightness of the Sr ion cloud, the ion cloud was never imaged with this camera

The ICCD on the Learjet did record the Sr burst, but the satellite motion placed the Ba burst just off the screen. The camera then catches up to the pair of bright release clouds at about 4 seconds after the Sr burst and tracks them for another 15 seconds. The Sr filter is placed on the camera at about 06:12:00. The Sr ion cloud was not thought to have been observed, but subsequent analysis showed that the Learjet ICCD did observe the cloud for less than 2 minutes starting at 06:11:57 UT.

The Sr and Ba bursts were observed by both IPDs, but the Sr burst was not recorded digitally to the computer on the KC-135 IPD. There is a videotape backup of these images which was used for triangulating the burst point. The Ba burst was recorded digitally by both IPDs. The Learjet IPD followed the release cloud measuring strong 455.4 nm emission for more than 20 seconds. The KC-135 IPD tracked a second bright cloud, moving perpendicular to the release cloud motion. This cloud is found to be a neutral Sr cloud that expands radially away on the plane

perpendicular to the magnetic field, and is discussed further in Chapter 5. Several similar neutral disks were seen in later sunlit barium releases from CRRES over the Caribbean in July and August, 1991 [*Delamere et al.*, 1996]. Because of this confusion the release cloud was not tracked with the KC-135 IPD, and the ion cloud was not recorded until nearly 2.5 minutes after the burst. Both IPDs observed the Ba ion cloud until $\sim$ 10 minutes after the burst at which time it became too diffuse to observe.

The one system on the KC-135 that did record both bursts also had a technical problem. The video cable from the ISIT to the tape recorder had an intermittent short, which resulted in video drop-outs. This made subsequent digitization difficult (but not impossible).

2.3.2 G-14

The data coverage of the G-14 releases was much improved. All five cameras observed both of the bursts, and short segments of the emitting release clouds. Both ICCDs were left unfiltered for nearly one minute until the Ba ion cloud could be seen developing. Both were then filtered and the Ca ion cloud was observed by both ICCD cameras for nearly five minutes. The IPDs, both filtered, observed the bursts and the subsequent release cloud. The Ba ion cloud development was recorded from both IPDs, except for a few interruptions when automatic safety circuits shut off the camera due to the increasing intensity. After adjusting the lens aperture, the cameras were restarted and continued to take data until nearly 20 minutes after the burst.

2.4 Release Geometries and Parameters

The first analysis done on the releases was to establish release times and positions. To the accuracy of the timing on the video data, the release times for both releases was that of the predicted release times. The positions were determined using triangulation from the two aircraft, and required a well established aircraft position which were provided by inertial navigation systems on each aircraft. Based on the release position and the ephemerides of the satellite, several parameter important to the subsequent analysis were calculated. The magnetic field is calculated using the IGRF model [*Peddie*, 1982]. The electron density was measured by the LASSII instrument on board CRRES [*Baumback et al.*, 1992, and P. Rodriguez, personal communication 1990]. The release parameters are listed in Table 2.1.

Table 2.1 - CRRES CIV Releases Parameters

	G-13		G-14	
	September 10, 1990		September 14, 1990	
Metal	Sr	Ba	Ca	Ba
Release time (UT)	06:10:22.5	06:10:25.0	08:47:10.0	08:47:12.5
Release position:				
Latitude (S)	17.54°	17.58°	18.07°	18.08°
Longitude (E)	198.85°	199.07°	161.55°	161.75°
Altitude (km)	516.8	513.6	592.5	596.4
Atoms, (10^{25})	1.04	0.95	1.14	0.95
$n(e)$, 10^6 cm^{-3}	3.5	3.4	1.6	1.5
n(O),[a] 10^7 cm^{-3}	4.9	5.1	2.5	2.4
n(He)[a], 10^6 cm^{-3}	2.1	2.1	1.9	1.9
T^a_{exo}, K	923	923	1134	1134
$\|\mathbf{B}\|^b$, nT	30530	30557	34937	34852
Ω_i, Hz	5.33	3.41	13.33	3.89
Gyro radius, m	243	435	110	376
Dip angle of **B**	33.6°	33.3°	44.3°	44.3°
Angle, **B** to Sun direction	114.0°	114.0°	117.31°	117.31°
Pitch angle of center[c]	79.8°	79.7°	77.9°	77.8°
$v_{\|\|}$, km/s	1.67	1.68	1.97	1.98
$v_\perp$, km/s	9.31	9.31	9.20	9.18
$v_0{}^d$, km/s	1.62	1.33	2.4	1.33

[a]Based on MSIS-86[*Hedin*, 1987]
[b]Based on IGRF model[*Peddie*, 1982]
[c]For southern hemisphere releases, pitch angles < 90° will result in upward motion
[d]see Equation 2.5

2.4.1 Release Clouds

To examine the development of the ion cloud it was necessary to have a velocity-pitch angle distribution of the release cloud. For this the velocity distribution of the release was needed, and was calculated from observations of the release clouds. The release clouds in white light cameras all exhibited a distinctive 'doughnut' shape. This was used to verify the distribution function of the release.

For a neutral gas expanding freely from a single point into a perfect vacuum the velocity and spatial coordinates of the distribution function are coupled. The velocity can be found from the time after the burst and the radius from the release point. In this case, the full 6N distribution function can be written as,

$$f(\mathbf{x},\mathbf{v},t) = F(\mathbf{v})\delta(\mathbf{x}-\mathbf{v}t) \tag{2.2}$$

where $\mathbf{v} = \mathbf{V} - \mathbf{v}_{\mathbf{sat}}$ is the velocity centered on the release cannister moving at $|\mathbf{v}_{\mathbf{sat}}|$. Assuming no ionization for the moment, the density function can be found by integrating over all velocity space,

$$n(\mathbf{x}) = \int\int\int F(\mathbf{v})\,\delta(\mathbf{x}-\mathbf{v}t)\,d^3\mathbf{v} \tag{2.3}$$

To make use of the delta function we convert the velocity to radius via $\mathbf{v} = \mathbf{x}/t$ and $d^3\mathbf{v} = d^3\mathbf{x}/t^3$, to obtain

$$n(\mathbf{x}) = \int\int\int F\left(\frac{\mathbf{x}'}{t}\right)\delta(\mathbf{x}'-\mathbf{x})\frac{d^3\mathbf{x}'}{t^3} = \frac{1}{t^3}F\left(\frac{\mathbf{x}}{t}\right) \tag{2.4}$$

From images of the release cloud the distribution is determined to be that of an expanding spherical shell, velocity v_0, with a width, v_{th} which is assumed to be gaussian due to collisions very early in the release [*Wescott et al.*, 1994]. The distribution is then,

$$F(v) = N_0 A \exp\left[\frac{-(v-v_0)^2}{v_{th}}\right] \tag{2.5}$$

where N_0 is the total number of neutrals available in the release, and A is a normalization factor. Converting to number density via Equation 2.4, the density function for the release is found to be

$$n(r,t) = \frac{N_0}{t^3}A\exp\left[-\eta^2\left(\frac{r}{v_0 t}-1\right)^2\right] \tag{2.6}$$

where η is the ratio of the radial to thermal velocities, $\eta = v_0/v_{th}$, and A can now be calculated as,

$$A = \left\{4\pi v_0^3\sqrt{\pi}\left[\frac{1}{\eta}+\frac{1}{\eta^2}\left(1+\frac{e^{-\eta^2}}{2}\right)\right]\right\}^{-1} \tag{2.7}$$

such that,

$$\int_0^{2\pi}\int_0^{\pi}\int_0^{\infty} n(r,t)\, r^2\, dr\, \sin\theta\, d\theta\, d\phi = N_0 \tag{2.8}$$

If the cloud is ionizing uniformly with time constant τ then the neutral density becomes

$$n(r,t) = \frac{A}{t^3}\exp\left[-\eta^2\left(\frac{r}{v_0 t}-1\right)^2\right] N_0 e^{-t/\tau} \tag{2.9}$$

The parameters v_0 and v_{th} were found to be 1.33 and 0.29 km/s respectively for the Ba releases from G-13 and G-14, [*Wescott et al.*, 1994] so that the value of η is 4.5. The expansion velocities, v_0 for Sr and Ca were measured to be 1.62 and 2.4 km/s respectively, which scale with the square root of the mass, as is expected from energetic arguments. The ratio η is assumed to be the same for Sr and Ca as it is for Ba.

Bernhardt et al. [1993] used a distribution function that included the part of the distribution from the opposite hemisphere, (*e.g.* $F(v) \propto \exp(-(v-v_0)^2/v_{th}) + \exp(-(v+v_0)^2/v_{th})$). In Figure 2.6 the density function in Equation 2.5 is compared to the double peaked distribution of *Bernhardt et al.* [1993]. Both functions are plotted in normalized units for similar values of η. The difference at the origin is seen to be very small (one part in 10^8), and therefore Equation 2.5 is used for ease of calculation.

2.4.2 Ion Clouds

The combination of the aircraft and satellite positions, the earth's magnetic field and the terminator complicate the geometry in the images of the ion clouds. Figure 2.7, while not to scale, shows the general characteristic found in the images. The difference in altitude between the aircraft and release (10 km vs. 500 km) means that the camera elevation angle is generally $\sim 45°$ (the cameras are looking up). Ions created in the release will follow the magnetic field lines, and the geometry of the field line for the releases is such that the cameras are viewing the underneath side of the release (like looking at a ceiling). Hence, the low altitude portion of the field line is the upper portion of the image and vice versa. There are two features in all the images of the ion clouds that are important to recognize; the terminator and the release field line. The terminator, being at lower altitudes is generally a sharp boundary near the top of the image, while the field lines run generally from top to bottom. There is a sharp boundary at the field line on which the release occurred which becomes more distinct as the cloud develops. Figure 2.8 shows where the

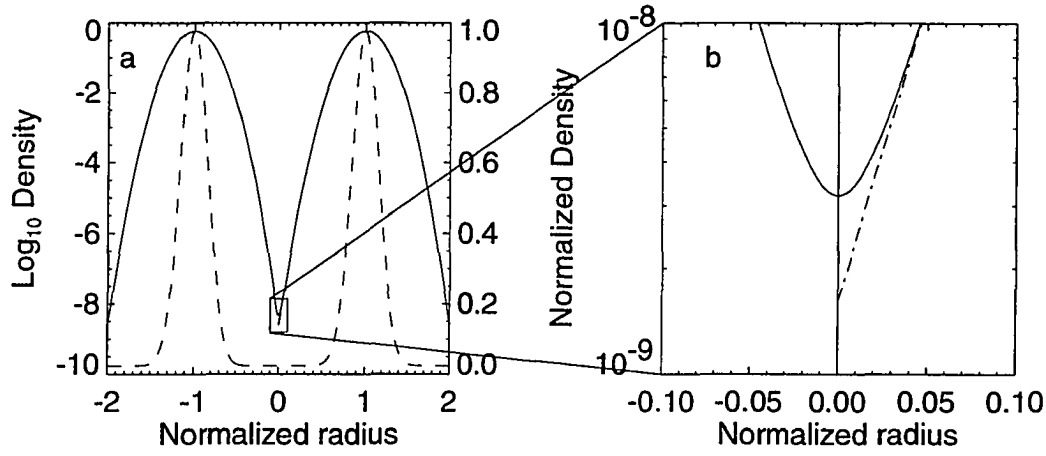

Figure 2.6: Comparison between distribution functions. a) The function used by *Bernhardt* [1992] is shown plotted on a linear scale (dashed line) and on log scale (solid line). Also plotted is Equation 2.5 (dot-dash line). The two functions are indistinguishable except near the origin. b) Comparison near the origin, where at $r = 0$ the difference is seen to be less than one part in 10^8.

terminator and release field line are for both IPDs for each release, as well as the approximate satellite motion in the image.

G-13 Sr

The development of the Sr^+ cloud is not well known due to its very low density. Only one of the two planes observed the ion cloud. Figure 2.9 shows an integrated image of the ion cloud as seen from the Learjet at approximately 1.5 minutes after the release. The integration time was 8 seconds. The signal from the ion cloud near the upper right of the image is not much above the background level. The image has not been corrected for vignetting, but has been smoothed to reduce noise. The most obvious portion of the cloud is seen in the upper right at the release field line.

G-13 Ba

The early development of the Ba^+ cloud is not recorded. The earliest image of the cloud is at 06:11:40 UT, shown in Figures 2.10 and 2.11. The cloud is characterized by a jet of ions on the initial field line, followed by a diffuse cloud that had not extended as far up the field line as the jet. The cloud extends about 180 km along

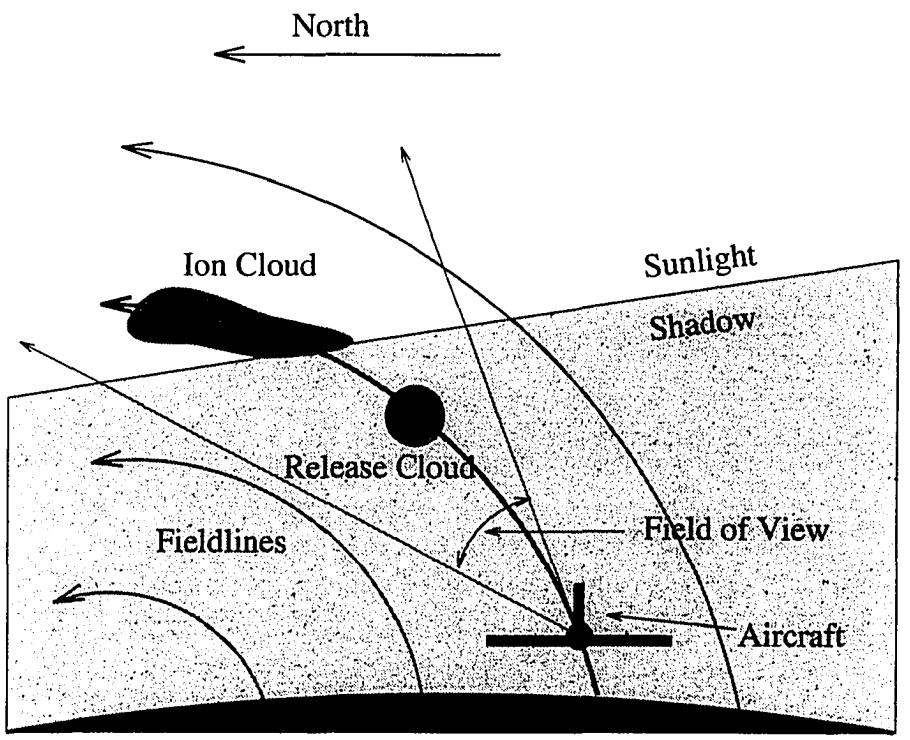

Figure 2.7: Image Geometry for CRRES South Pacific Releases. The geometry is shown for the aircraft lying in approximately the same N-S magnetic plane as the release. The image elevation was generally 45°. The cartoon is not to scale.

the satellite track, equivalent to 20 seconds of ionization.

G-14 Ca

The early development of the Ca ion cloud is not known. The Ca filters were not applied to the ICCDs until about 1.5 minutes after the release. By this time the ion cloud was already in sunlight. The ion cloud was visible from both aircraft and was imaged from both. Figure 2.12 shows the Ca ion cloud at 08:48:40. The image is a 12 second integration. The signal is relatively weak owing to the low sensitivity of the intensifier tube in the near UV (393.3 and 396.8 nm).

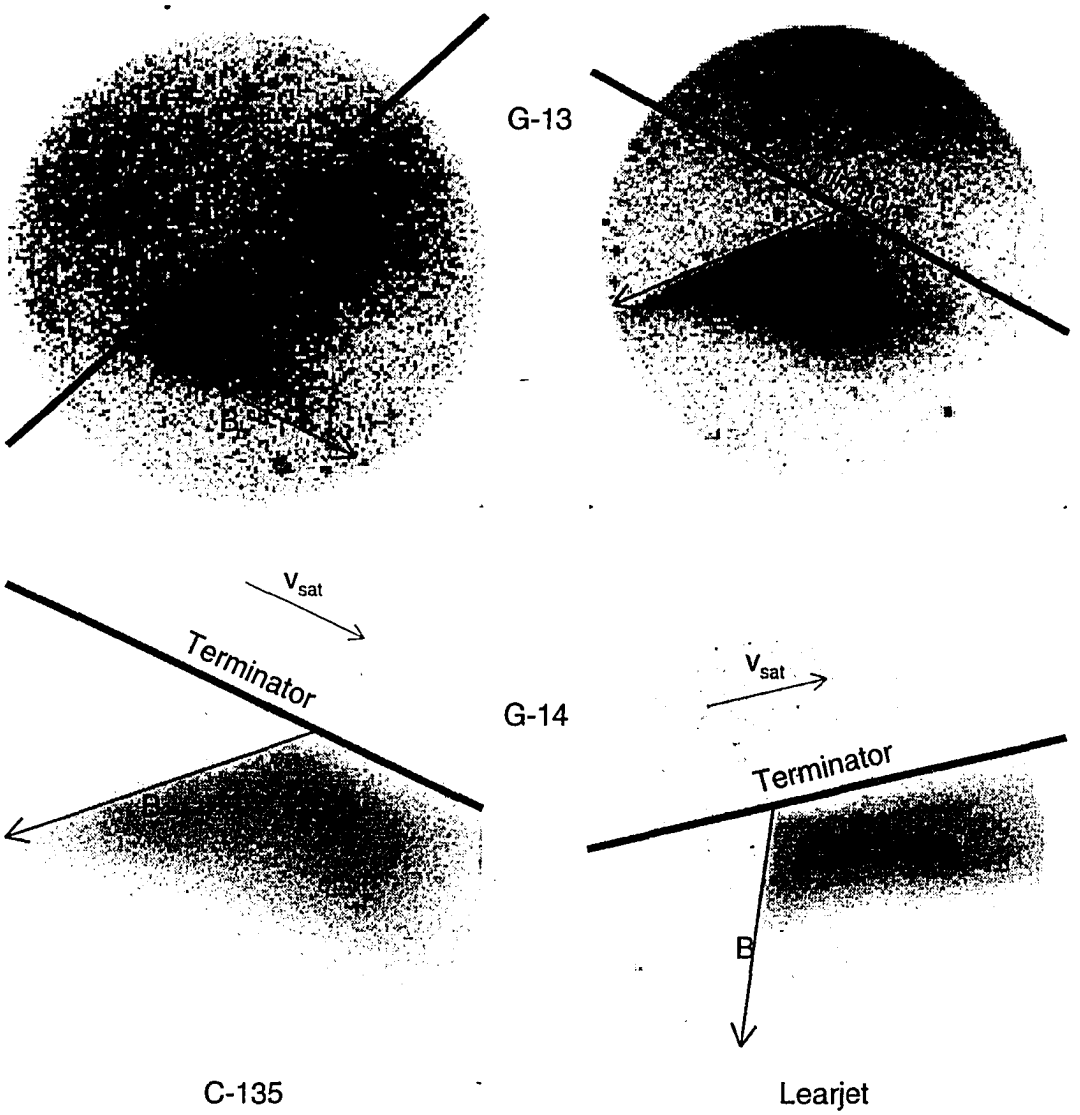

Figure 2.8: IPD image geometries. The important landmarks are marked for each Ba ion cloud from each plane. The terminator is shown as the heavy gray line. The direction of the release magnetic field line row and the approximate satellite motion are shown by arrows.

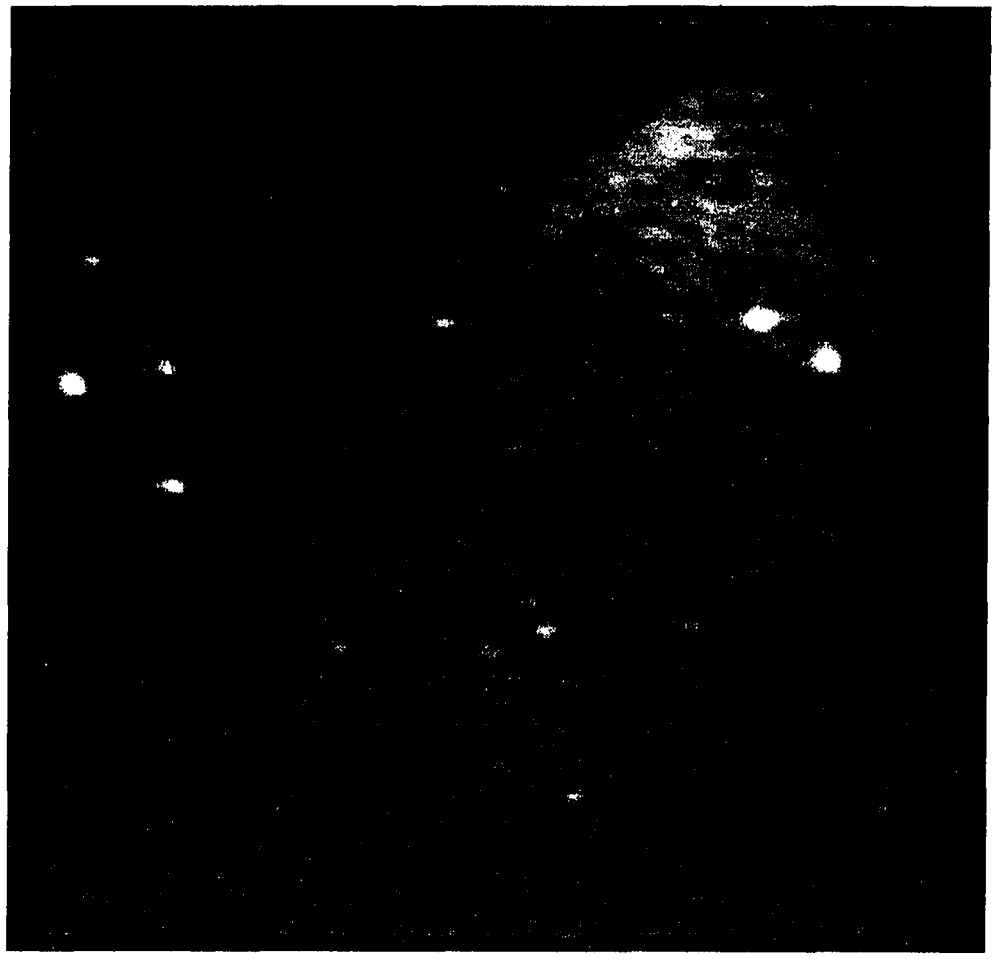

Figure 2.9: G-13 Sr Ion Cloud. An image of the G-13 Sr ion cloud is shown. The image is from the ICCD on the Learjet at about 1 min 30 s after the release.

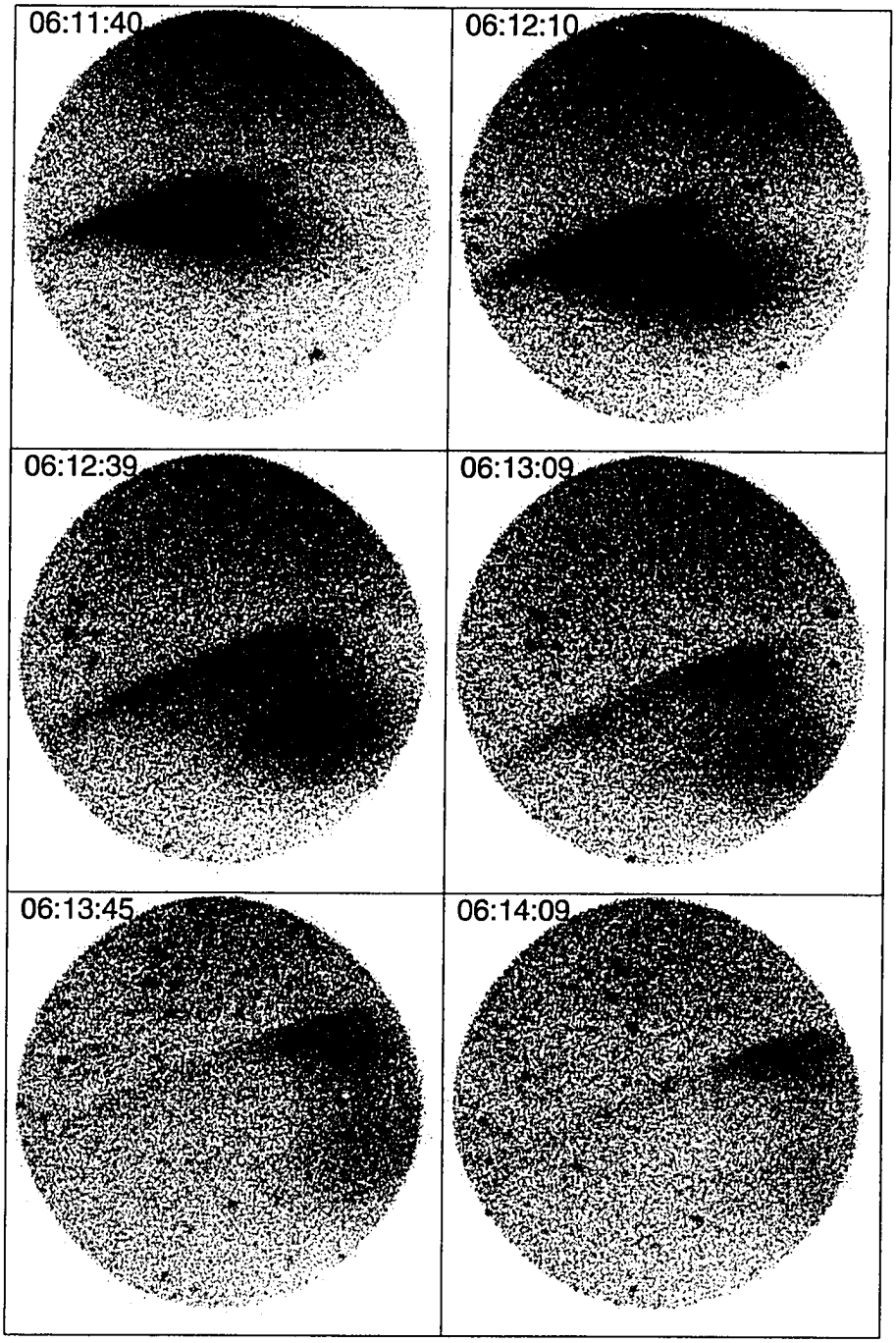

Figure 2.10: Development of G-13 Ba release from Learjet. The time development of the G-13 Ba ion cloud is shown as viewed from the Learjet IPD with the same terminator and release field line as shown in Figure 2.8. The UT times are indicated in the images.

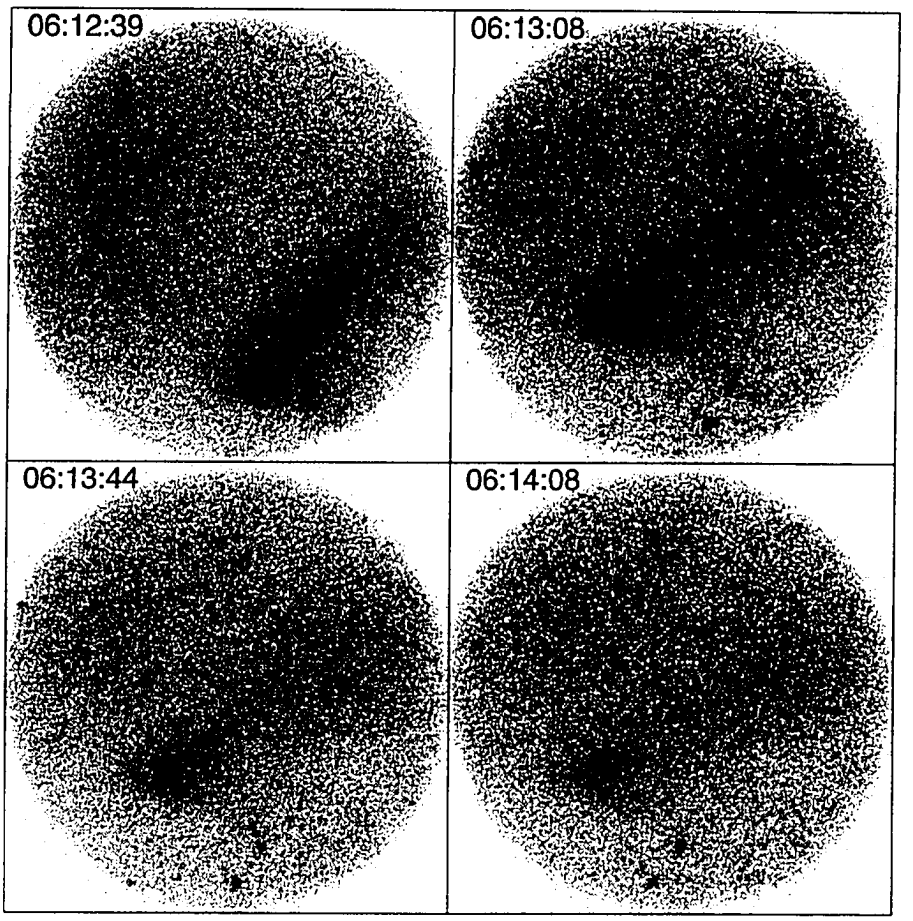

Figure 2.11: Development of CRRES G-13 Ba Release from KC-135. The Ba ion cloud as viewed from the KC-135 IPD is shown with the same terminator and release field line as shown in Figure 2.8. The times of the images correspond to the times of the last four images from Figure 2.10

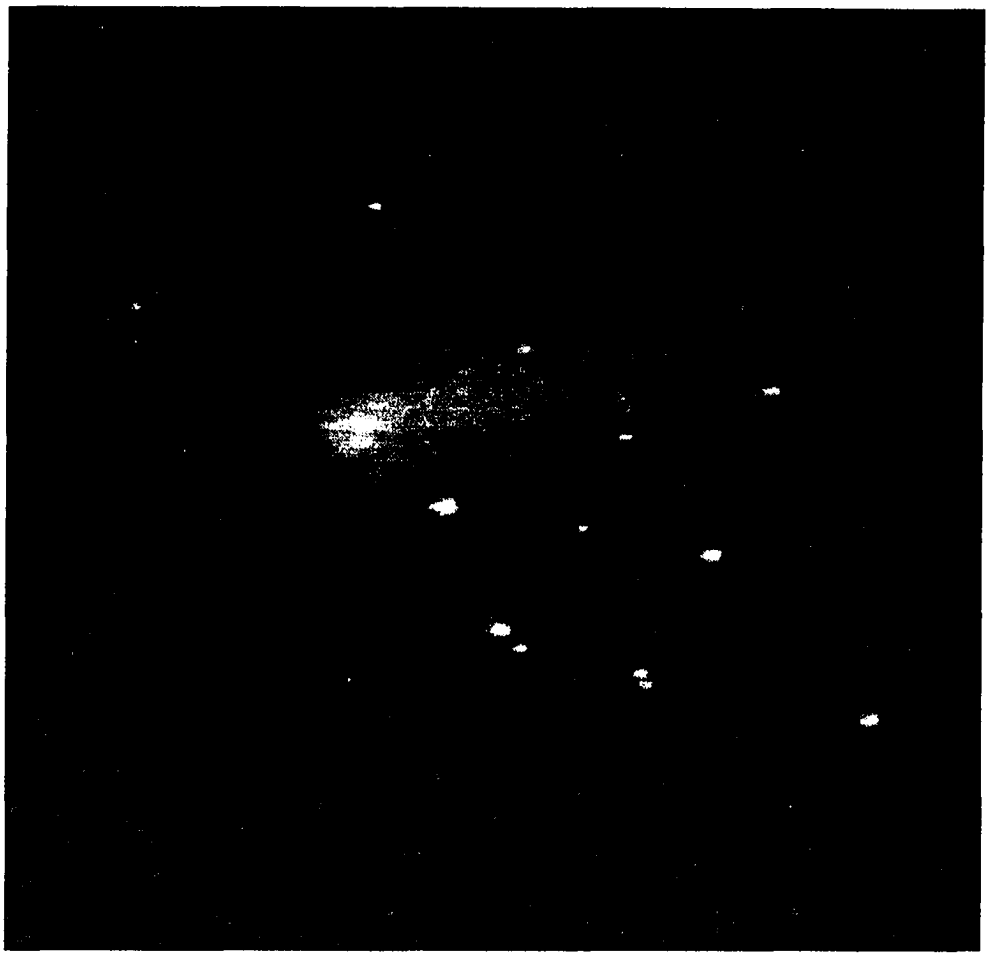

Figure 2.12: G-14 Ca Ion Cloud from Learjet ICCD. A composite image of the Ca cloud from G-14 is shown. The image is from the ICCD on the Learjet at about 1 min 30 s after the release.

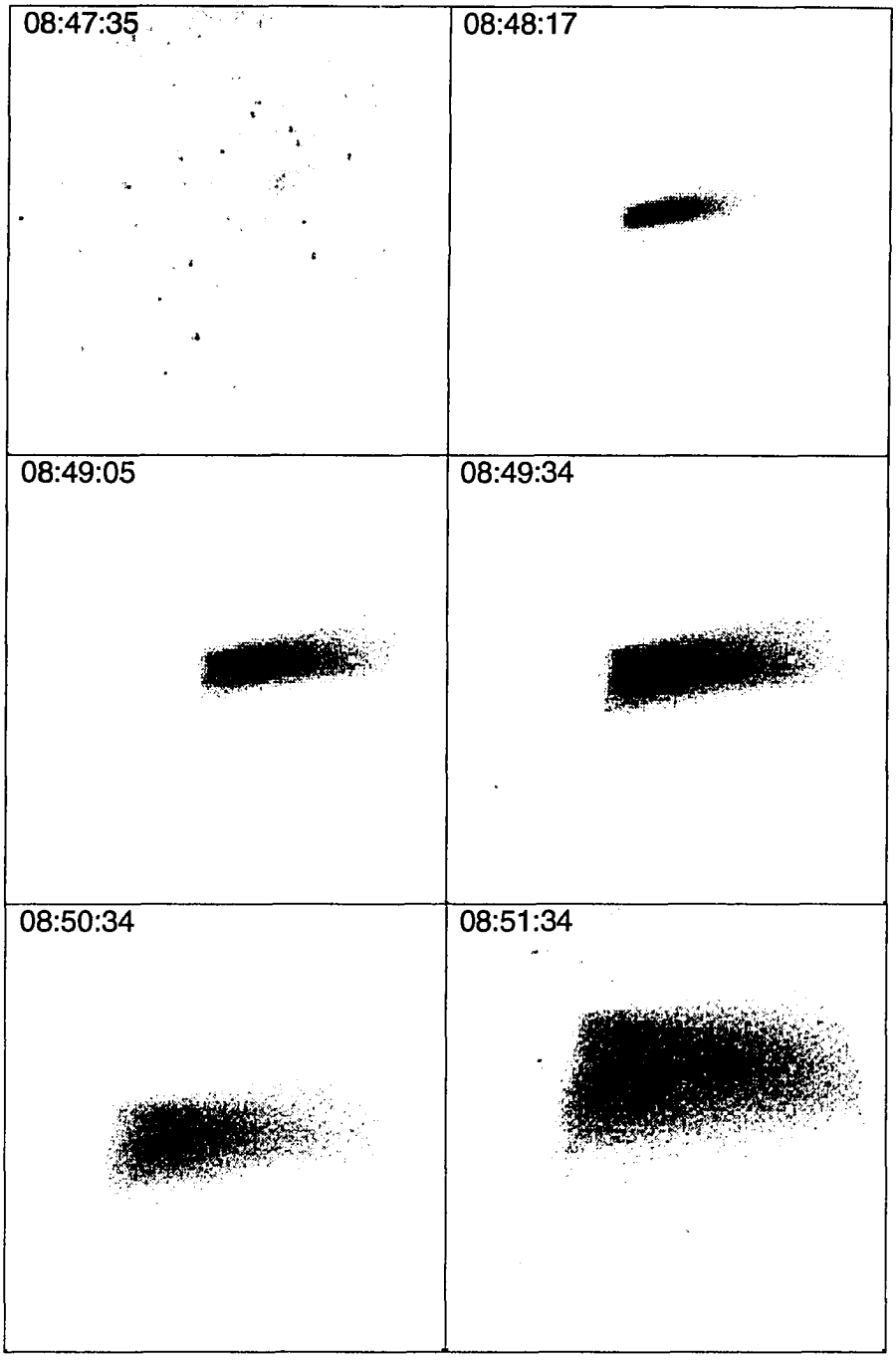

Figure 2.13: Time development of G-14 Ba release from Learjet. The UT times are indicated on the images. The geometry is shown in Figure 2.8.

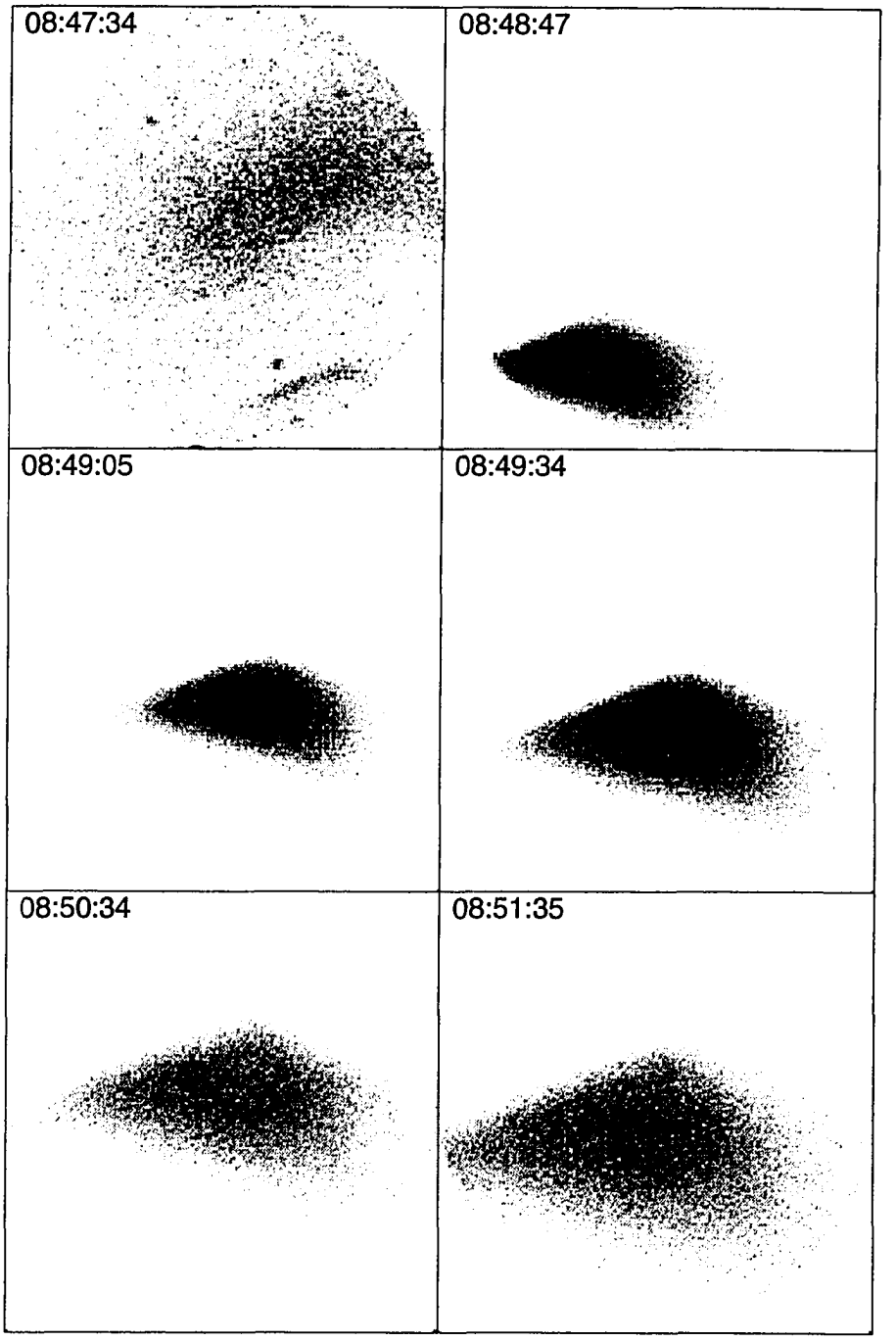

Figure 2.14: Time development of G-14 Ba release from KC-135. The UT times are indicated on the images. The geometry is shown in Figure 2.8.

G-14 Ba

The development of the Ba release was well documented for G-14. Both the filtered IPDs and the ICCD cameras, before the Ca filters were applied, imaged the ion cloud as it appeared. A synopsis of this development is shown in Figures 2.13 and 2.14, as seen by the IPD's. At 27 seconds after the release a narrow streak of ionization, on the release field line is seen. The cloud further along the satellite track is seen to emerge at later times and shows little structure. The intensity along the satellite track is seen to be fairly constant in the Learjet image by 08:51:34 UT.

2.4.3 Release Cloud Redux

From the filtered IPD's it was determined that most of the luminosity from the release clouds below the terminator is from line emission, after an initial broadband glow. Figure 2.15 shows the Ca release intensity, and the Ba release intensity as seen through the Learjet IPD filtered for the 455.4 nm line of Ba^+ for the G-14 release. The Ca release shows an initial peak of (presumably broadband) emissions that decays rapidly, whereas the Ba release decays much slower. In fact the glow is still prominent as it reaches the edge of the image after 10 seconds, in the next IPD image. The Ca cloud is seen to glow in the white light ICCD camera, with approximately the same intensity as the Ba cloud for a similar time. Thus the extended glow from the Ba cloud is from emission lines. The ratios of these lines are used later to examine the collisional processes that take place during the early phase of the releases.

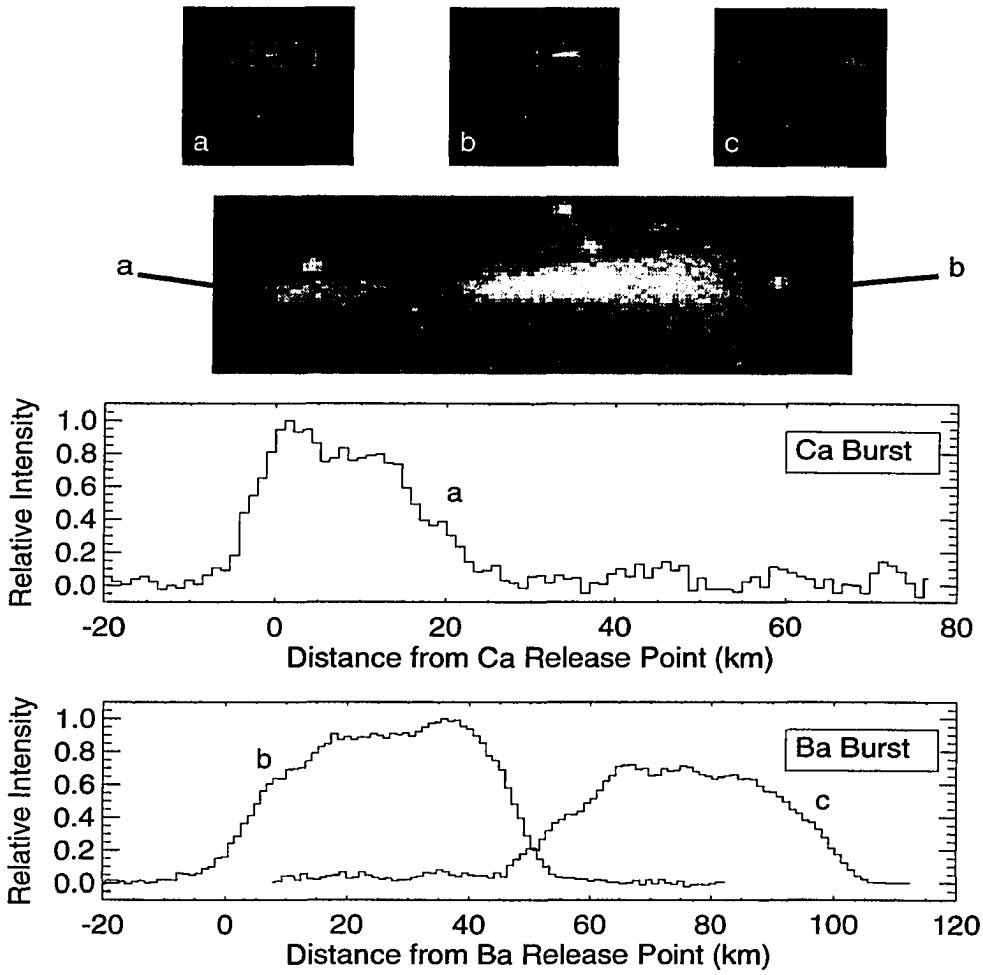

Figure 2.15: Release clouds observed with filtered IPD. The G-14 release clouds were seen in three images (a, b & c) from the Learjet IPD, which was filtered for the Ba^+ 455.4 nm emission line. The sum of first two images showing the two bursts, and subsequent emissions is shown below the three raw images. The measured intensities of the Ca release and the Ba release from from each image are plotted below. The Ca release , a, decays within 25 km of the release position corresponding to ≈ 2 seconds, while the Ba release (b & c) is seen to emit for 100 km, or 10 seconds, indicating that the light from the Ba release is predominantly from line emissions

Chapter 3

Collision Cross Sections

The atomic collisions outlined in the first chapter are well known in atomic and molecular physics. But the role of collisions in space-based CIV releases is still in question because many of the cross sections for specific collisions involving Ba, Sr, Ca and their ions with ambient ionospheric species have not been measured. Associative ionization has recently been a topic of interest, but the alkaline earths are not well represented in either theory or experiment. Charge exchange collisions have been studied for many species, including a measurement of Ca with O^+, but convincing experimental results of Ba with O^+ have not been reported to date. In contrast, electron impact excitation and ionization of Ba, Sr and Ca have been studied experimentally by several groups and the cross sections are well known.

In this chapter the cross sections for the collisions listed in the first chapter are presented. For those that have been measured the results are presented with a general discussion as to their accuracy. For those that have not been, the results estimated by other researchers are presented and discussed based on a literature review. In the case of charge exchange, the cross section is estimated using a well known approximation method.

3.1 Neutral Impact Ionization or Charge Stripping

In a binary collision between two neutral atoms, there is a probability that the collision will result in an atom ionizing if there is free energy in the system greater than the ionization potential of one of the atoms. For ionization of an alkaline earth

atom in a collision with atomic oxygen, the minimum velocity in the laboratory frame is $v_{min} = v_{cr}\sqrt{1 + \frac{m_1}{m_2}}$, where v_{cr} is Alfvéns critical velocity (Equation 1.1) and m_1 and m_2 are the masses of the metal and oxygen respectively. The minimum velocities are 8.4, 9.0, and 10.2 km/s to ionize Ba, Sr and Ca respectively, in collisions with O. The CRRES release velocities were around 9.5 km/s which are very close to the threshold velocities listed above. The ionization rate due to charge stripping in the releases may be highly variable within the release cloud because of velocity dispersion within the cloud.

Fleishmann et al. [1972] derive a two parameter semi-empirical approximation and use an empirical approximation of *Firsov* [1959] to model the charge stripping cross section for two arbitrary atomic species. Both of these methods work reasonably well for center of mass energies in the tens of keV and higher, but both show a finite cross section at energies where charge stripping should be energetically forbidden and by definition are poor predictors of the stripping cross section near threshold. Both methods do show that the cross section changes rapidly near the threshold energy so that a precise determination of the stripping cross section is difficult in this range.

Stenbaek-Nielsen et al. [1990a] use the local neutral density and the ionization rate of the CRIT I release to estimate a charge stripping cross section of 9×10^{-18} cm^2. This value may be too large however, based on the work of *Swenson et al.* [1991] who argue that the charge exchange cross section for Ba with O^+ is much larger than previously estimated. The cross section of 9×10^{-18} cm^2 remains a good upper estimate nevertheless. At this upper limit and for the CRRES release parameters, the ionization time constant would be 5^{-14} s^{-1}, or 1% in 20 seconds.

3.2 Neutral Impact Excitation

The excitation of emissions from the neutral atoms and ions of Ca, Sr and Ba by collisions with ambient species or themselves will undoubtably occur. The cross sections for producing these emissions are quite important in the determination of the ionizing cross sections, since the emissions will be visible in the release cloud. The magnitude of the intensity due to these collisions will have to be accounted for in the measurements. The cross sections for emissions of the three release materials with O, O^+ or each other are not found in the literature. There has been work by *Shpenik et al.* [1972] of the excitation cross section for Cd with Ca^+, Sr^+ and Ba^+ for energies up to 1 keV. The cross sections are generally less than 1×10^{-18} cm^2

for CRRES release energies. These include the resonant lines of Ca^+, Sr^+ and Ba^+ which are allowed transitions to the ground state. Thus, as an upper limit for neutral impact excitation, a cross section of 1×10^{-18} cm^2 is used. This would result in an emission rate of $\sim 5 \times 10^{-5}$ s^1 for the CRRES release parameters. This is less than is seen in the releases (described in Chapter 5), therefore the contribution from neutral impact excitation is expected to be small.

3.3 Charge Exchange

As the name implies, a charge exchange collision is one in which the two colliding particles transfer one (or more) electron(s). Typically the reaction is similar to that shown in Equation 3.1, where a positive ion acquires an electron from a neutral particle.

$$A + B^+ \rightarrow A^+ + B \tag{3.1}$$

When both A and B in equation 3.1 are the same species the reaction is called symmetric charge exchange and when A and B are different species it is called asymmetric charge exchange. Symmetric charge exchange is also referred to as resonant since the energy needed to detach the electron from the neutral will exactly match the energy that electron will gain as it attaches to the ion. There is no net transfer of energy. Because the reaction is through resonant channels, the collisions can have large cross sections ($\approx 10^{-14}cm^2$) which in a chemical release would result in significant ionization.

While a random selection of two atomic species for asymmetric charge exchange generally does not result in a large cross section for the reaction, in some cases there are energy levels that allow the energy lost and energy gained to match closely. In this case the cross section can be large, even approaching the magnitude of symmetric charge-exchange. These asymmetric reactions are termed near-resonant, and are of importance to CIV releases. In fact, the work presented here indicates that charge exchange is the dominant collisions process for the observed ionization.

3.3.1 Estimates Based on the Two-State Approximation

The theoretical method of *Rapp and Francis* [1962] is used to estimate the charge exchange cross section of collision of Ba, Sr and Ca which have near-resonant reaction channels with O^+. To discuss the uncertainties in this method it is important

to know what assumptions go into the development, which is given by *Rapp and Francis* [1962]. A similar calculation was done by *Liou and Torbert* [1995] for the CRIT II Barium releases, with similar results. Also included here is a calculation for Sr.

In general, the cross section for a collisional process is calculated by

$$\sigma(v) = 2\pi \int_0^\infty P(b,v) b \, db \tag{3.2}$$

where $P(b,v)$ is the probability of the collision to occurring for relative velocity, v, and impact parameter, b. The basic physics of the model developed of *Rapp and Francis* describes the probability, $P(b,v)$, for both symmetric and asymmetric charge exchange. Both results will be presented since the results from the symmetric case are needed to calculate the asymmetric cross section.

Symmetric Charge Exchange

For symmetric charge exchange the probability is found to be

$$P(b,v) = \sin^2 \left[\int_{-\infty}^{\infty} \frac{(E_a - E_s)dx}{2\hbar v} \right] \tag{3.3}$$

where E_a and E_s are the energies of the anti-symmetric and symmetric stationary states, respectively, and x is the distance along the trajectory. While the collisional process is decidedly non-stationary, the assumption underlying Equation 3.3 is that for inter-nuclear separations much greater than a Bohr radius, a_0, the molecular states can be approximated by stationary states [*Rapp and Ortenburger*, 1960]. Thus the only free parameters in the calculation are E_a and E_s. The states that they use are scaled hydrogenic wave functions,

$$\psi(r) = \frac{1}{\sqrt{\pi a_0^3}} \left(\frac{I}{13.6} \right)^{\frac{3}{4}} \exp \left[- \left(\frac{I}{13.6} \right)^{\frac{1}{2}} \frac{r}{a_0} \right] \tag{3.4}$$

where I is the ionization potential of the atom in eV, r is the distance of the electron from the nucleus. Note that for $I = 13.6$ eV these reduce to the wave functions for hydrogen. For inter-nuclear separation R, the quantity $(E_a - E_s)$ is calculated to be,

$$(E_a - E_s) = 2I(R/a_0) \exp \left[- \left(\frac{I}{13.6} \right)^{\frac{1}{2}} \frac{R}{a_0} \right] \tag{3.5}$$

Inserting this into Equation 3.3 and integrating the probability is found to be

$$P_0(b,v) = \sin^2\left\{\frac{2Ib^2}{a_0\hbar v}\left[K_0(\gamma b/a_0) + \frac{K_1(\gamma b/a_0)}{\gamma b/a_0}\right]\right\} \tag{3.6}$$

where $\gamma = (I/13.6)^{\frac{1}{2}}$, and K_0 and K_1 are the zero and first order Bessel function of the second kind

The cross section can then be found by integrating P_0 for all impact parameters, as in Equation 3.2. *Rapp and Francis* [1962] make several numerical approximations to calculate this integral without the aid of high speed computers. While this is no longer necessary, it is instructive to dissect the function in Equation 3.6. The argument in the $\sin^2$ function, which they label as $A(b,v)$ is a rapidly decreasing function of b that goes to zero as b goes to infinity seen in Figure 3.1a. The probability, P_0, is plotted in Figure 3.1b and is seen to oscillate rapidly for small b, and then decreases to zero as $A(b,v)$ goes to zero. They approximate P_0 with its average, $\frac{1}{2}$, until $A(B,v)$ reaches $\pi/6$ (at which point P_0 is $\frac{1}{4}$). The impact parameter for which this happens is labeled b_1 as seen in Figure 3.1b, and Equation 3.2 is simplified to calculate the cross section;

$$\sigma(v) = \tfrac{1}{2}\pi b_1(v) \tag{3.7}$$

Asymmetric Charge Exchange

For asymmetric charge exchange the system is again constructed of two point nuclei and an electron that can be attached to either one. The exact solution would be described in terms of molecular orbitals Ψ of the molecule AB^+. Again *Rapp and Francis* [1962] approximate the full molecular solution by means of a combination of atomic orbitals, namely

$$\Psi = c_A(t)\phi_A(r_A)\exp(i\omega_A t) + c_B(t)\phi_A(r_B)\exp(i\omega_B t) \tag{3.8}$$

where the c's are time dependent coefficients of the expansion, the ϕ's are atomic wave functions for electrons on A^+ or B^+, and $\omega_j \equiv \epsilon_j/\hbar$ where the ϵ's are the energies of A and B in states ϕ_A and ϕ_B. By initializing the coefficient $|c_B(t=-\infty)|^2$ to unity, the charge exchange cross section is found by examining the absolute square of c_A as $t \to \infty$. This is the two state approximation; having two possible outcomes, the probability of a reaction occurring is the square of the time dependent expansion coefficients.

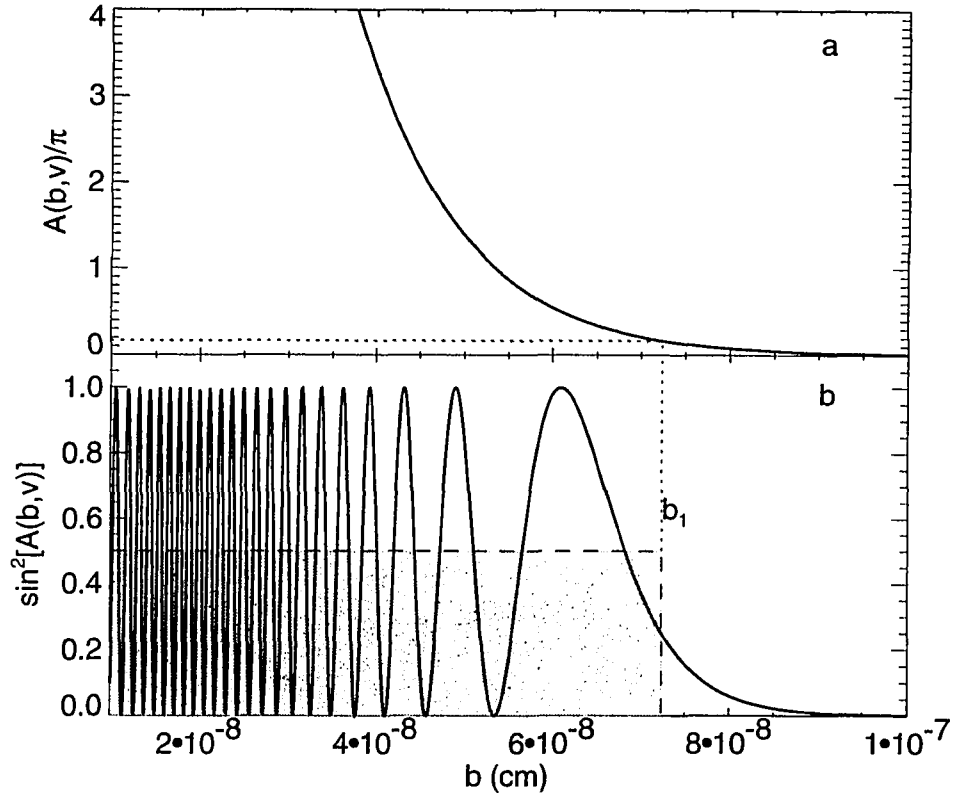

Figure 3.1: Functions for symmetric charge exchange. a) The Bessel function argument, $A(b,v)$ is plotted against b, the impact parameter. b) The probability, $P(A(B,v))$ is shown, as well as the impact parameter b_1 used in the calculation. The shaded area is integrated to find the cross section.

To solve for the coefficients the Schrödinger equation for the electron in the presence of both A^+ and B^+ is applied to Ψ,

$$\left[\frac{-\hbar}{2m_e}\nabla^2 + V_A(r_A) + V_B(r_B)\right]\Psi = i\hbar\frac{\partial\Psi}{\partial t} \tag{3.9}$$

where V_i is the effective potential for the electron near either nucleus (A or B). This results in a set of coupled equations in c_j and $\dot{c}_j$, the solution to which is arrived at after many approximations. The coupled equations are second order, and *Rapp and Francis* note that for reaction channels where $|\omega_B - \omega_A| << \omega_A$ or ω_B some cross terms in the coupled equations can be eliminated. This means that the final solution is valid only for near resonant collisions. They also note that the use of atomic orbitals rather than molecular orbitals is only justified for impact parameter

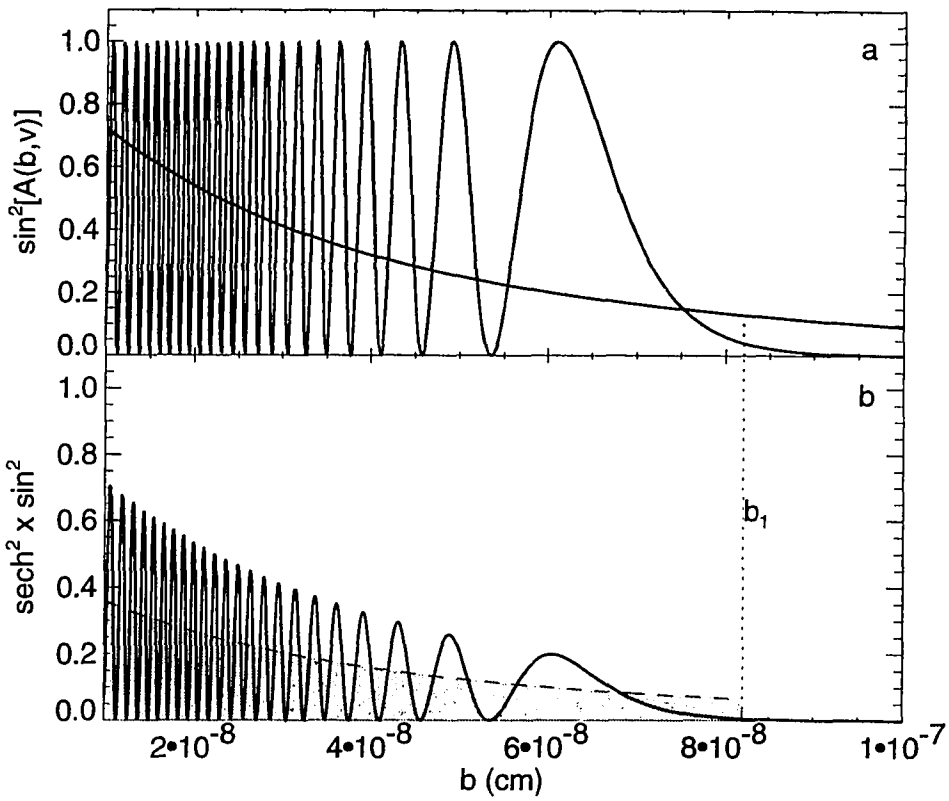

Figure 3.2: Functions for asymmetric charge exchange. a) The symmetric charge exchange probability, P_0 as well as the sech^2 function are shown plotted against b. b) Their product is shown, as well as the impact parameter b_1 used in the calculation. The shaded area is integrated to find the cross section.

greater than the scale size of the atomic orbitals ($\sim a_0$), which also implies that the method is good only for near resonant collisions.

The solution is found to be

$$|c_A(t \to +\infty)|^2 \sim P_\omega(b,v) = fP_0(b,v)\mathrm{sech}^2\left[(\omega/v)(a_0\pi b/2\gamma)^{\frac{1}{2}}\right] \qquad (3.10)$$

where $\omega = \omega_B - \omega_A$ is the energy deficit between initial and final states, P_0 is the symmetric probability introduced in Equation 3.6 with I now "some suitable mean between I_A and I_B"[*Rapp and Francis*, 1962, p. 2641]. The factor f has to do with the statistical weights of the initial and final states For all the collisions of alkaline earths with O^+, f is 1. Again, following the model of the symmetric case, numerical approximations are used to calculate the cross section. They define an

impact parameter b_1 to be where

$$\text{sech}^2\left[(\omega/v)\sqrt{a_0\pi b/2\gamma}\right] = 4P_0(b,v) \tag{3.11}$$

after the last peak in P_0 (see Figure 3.2b). This is used as the limit of integration, with P_0 again being approximated by its average of $\frac{1}{2}$. The cross section is then found by integrating

$$\sigma(v) = 2\pi f \int_0^{b_1} \tfrac{1}{2}\text{sech}^2\left[\frac{\omega}{v}\sqrt{\frac{a_0\pi b}{2\gamma}}\right] b db \tag{3.12}$$

If there is no b for which this happens (the sech function is below P_0), then the limit of integration is set to ∞.

There are two parameters that control the form of the resulting cross sections; the ionization potential, I, and the energy deficit, ω. The effects of the two parameters are shown in Figure 3.3. In Figure 3.3a, I is varied, while the energy deficit is kept fixed at 0. Changing I has the effect of shifting the magnitude of the cross section without changing the overall shape of the curve. This is understandable since the ionization potential is a factor in the argument of P_0 which will determine the value of b_1 for the integration. The effect of the energy deficit is seen in Figure 3.3b in which the cross section for fixed I is plotted for several values of ω. In this case the shape of the curve is altered for different deficits. The energy deficit controls the scaling of the sech^2 function, which for large ω/v sets the effective upper limit in the integral in Equation 3.12 to values of b less than the last peak in P_0. For small values of ω/v the sech^2 function is still nearly unity as P_0 passes through its last peak, and the cross section approaches that for symmetric charge exchange for the given ionization potential.

The use of atomic orbitals rather than molecular orbitals means that the interaction between nuclei is not included in the calculations. This implies that the method will only be accurate for large inter-nuclear separations ($\gg a_0$), and therefore only for collisions with large cross sections. The requirement that the energy deficits be small compared to the ionization potential has the equivalent result of requiring that the cross section must be large for accurate approximations. For Ca and Ba colliding with O^+ the energy deficits are certainly much smaller than the ionization potential, and for Sr which does not have what would be called a near resonant channel, the energy deficit is only a small fraction of the ionization potential of Sr.

The accuracy of the results can be examined by comparing the results of the calculation of Equation 3.12 to a laboratory measurement of the charge exchange

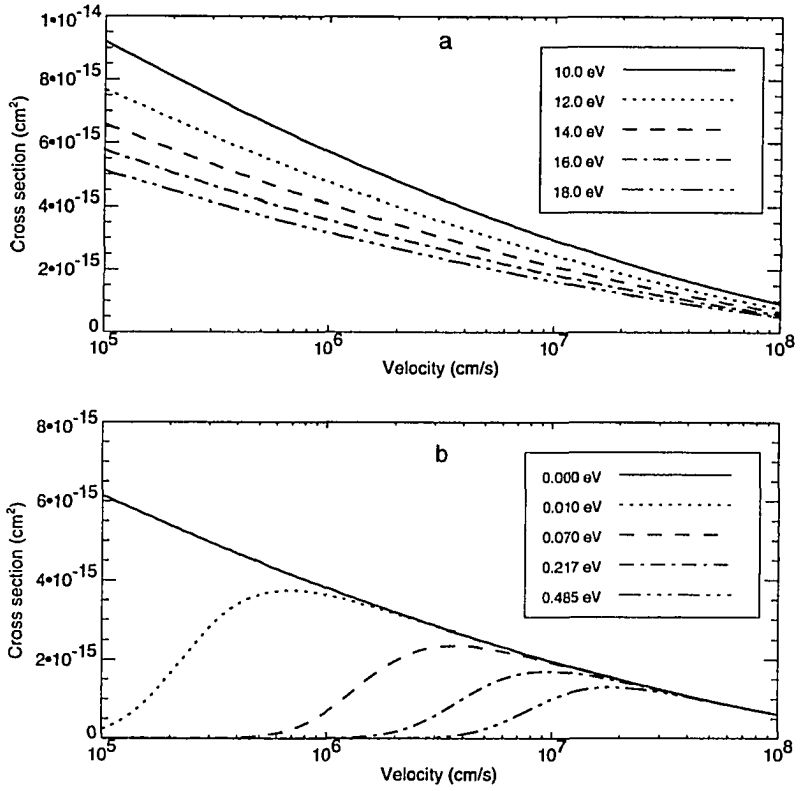

Figure 3.3: Effect of ionization and energy deficit on calculation of charge exchange cross section. a) For constant energy deficit, ω (=0), the cross sections for several values of I are plotted. The shape of the curve remains relatively constant. b) For constant I (= 16.0 eV) the cross section is plotted for several values of ω. For larger ω the cross section at lower velocities is reduced drastically.

cross section for the production of Ca ions in collisions of Ca with O^+ [*Rutherford et al.*, 1974]. Both are shown in Figure 3.4 for the velocity range between 1 and 100 km/s. The cross section is calculated for two different values of I; the ionization potential of Ca, and the ionization potential of O. The reaction $Ca+O^+ \rightarrow Ca^+ + O$ has a near resonant channel if the calcium ion is left in the $5p\ ^2P_{\frac{1}{2}}$ state. In this case the reaction has an energy deficit of only 0.001 eV, and for the velocities plotted the cross section does not deviate noticeably from the symmetric result. The range of velocities in the CRRES G-14 release is shown as a shaded region in the figure. The CRRES G-13 release has a similar velocity range.

Shown in Figure 3.5 is the calculation for charge exchange between Ba and O^+. There is a near-resonant channel that leaves the Ba^+ in the $6g\ ^2G_{\frac{7}{2}}$ state,

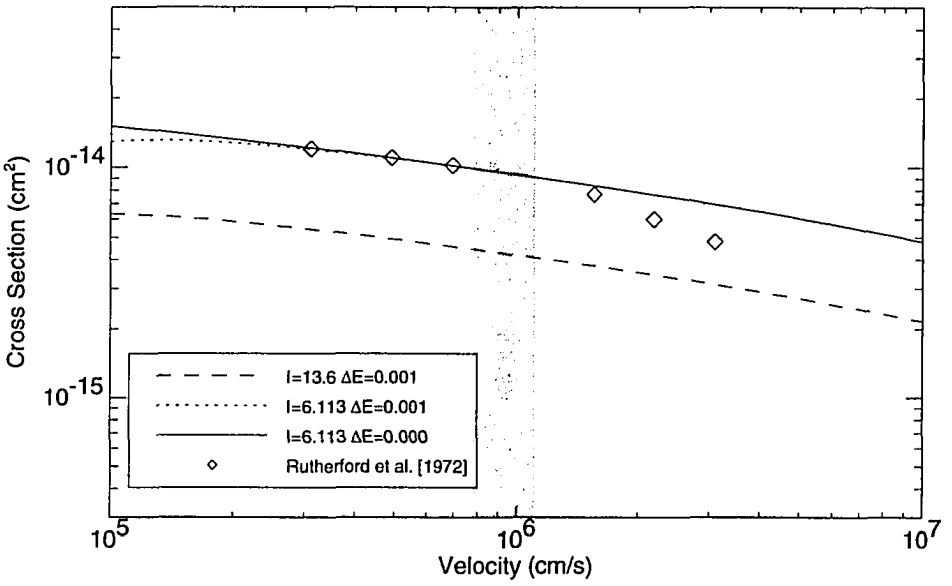

Figure 3.4: Charge exchange cross sections for Ca. The calculated cross section for charge exchange collisions of Ca with O^+ are compared to the data of *Rutherford et al.* [1974]. The calculations are made for the ionization potentials, I for Ca and O. The velocity range of the G-14 Ca release is shown in the shaded area.

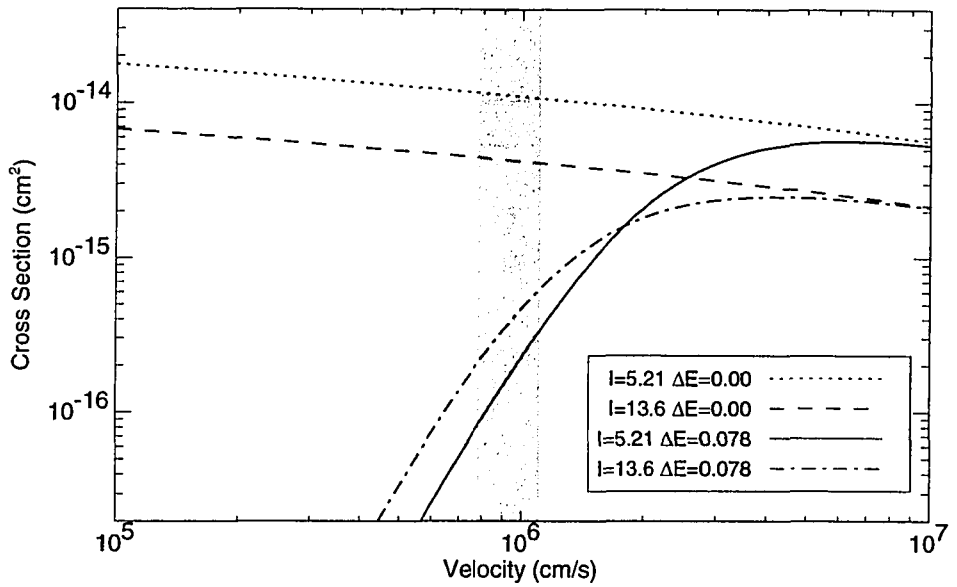

Figure 3.5: Calculated charge exchange cross section for collisions of Ba with O^+. The cross section for energy deficit 0.078 eV is shown in the solid line. The resonant charge exchange cross sections for Ba and O are shown in dashed lines. The velocity range of the G-14 release shown in the shaded region. The range is similar for G-13.

which has an energy deficit of 0.078 eV. Again, he velocity range for the CRRES G-14 Ba release (See Chapter 2) is shown as the shaded region. The calculated cross section for this release ranges between 7×10^{-17} cm^2 and 6×10^{-16} cm^2. The calculation for charge exchange of Sr with O^+ is shown in Figure 3.6. The energy deficit for Sr is 0.132 eV, and the cross section for CRRES release velocities is seen to be much lower than for Ca and Ba, less than 1×10^{-16} cm^2.

Thus for Ba and Sr the cross sections are not as large as the Ca charge exchange cross section, as argued by *Swenson et al.* [1991]. However, the Ba cross section is substantial, ranging from 1×10^{-16} cm^2 to 6×10^{-16} cm^2 at the center velocity of th releases. Of the collisional processes, charge exchange should produce the highest ionization rate for Ba releases. The Ca charge exchange cross section should be nearly 1×10^{-14} cm^2 according to both the measurement and the two-state calculation. This should by far be the dominant collisional ionization process for the Ca release. For Sr, the ionization rate should not be significantly greater than stripping or other collisions with neutral O.

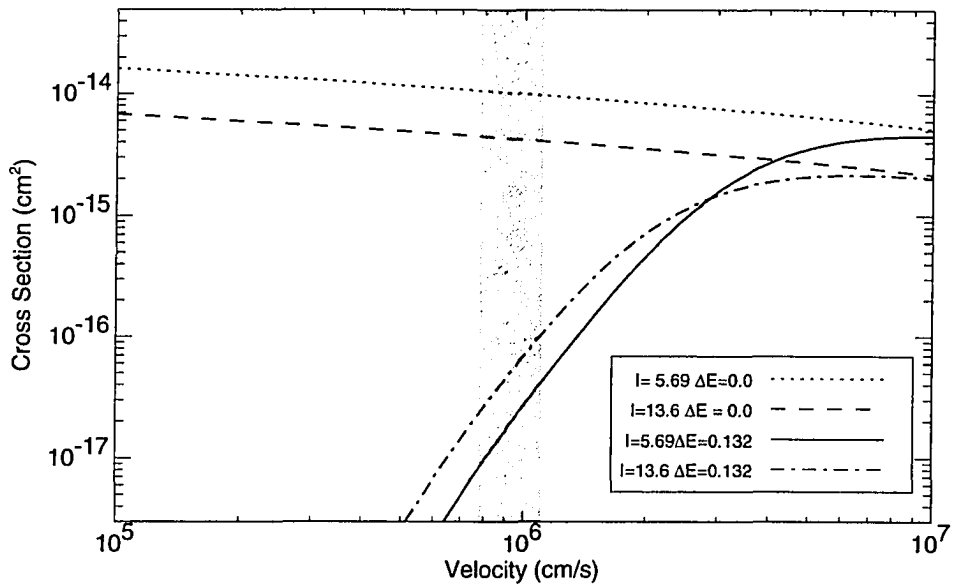

Figure 3.6: Calculated charge exchange cross section for Sr with O^+. The values of the ionization potential, I, of Sr and O are shown for $\omega = 0$ and 0.132.

3.3.2 Metastable states

Recently, *Hunton* [1995] has examined the possibility that long lived metastable states in the alkaline-earth atoms may augment the effective charge exchange cross section for chemical releases. For several CRRES sunlit releases, the ratio of Ba^+ to Sr^+ is much greater than would be expected for Ba releases doped with a few percent Sr. Strontium has a very slow photo-ionization rate compared to Ba in sunlight, and in its ground state does not have a near-resonant charge exchange channel, so its ionization rate should be low. However, he finds that if the Sr is in one of several dipole forbidden metastable states, (^3D_J, or ^1D_J), then there are near resonant reaction channels for charge exchange to occur. Energy deficits for many of the metastable states of Ba, Sr and Ca in reactions with ground state O^+ are listed in Tables 3.3.2 and 3.3.2. This will be important for sunlit releases for which scattering of sunlight will populate these states readily. For below-the-terminator releases the rate at which these states are populated should be much slower.

Table 3.1a – Energy Deficits for Charge Exchange Channels				
Neutral State	Energy [eV (cm^{-1})]	Ion State	Energy [eV (cm^{-1})]	Deficit[a] [eV (cm^{-1})]
Ca	I.P. 6.111 eV, 49304.80 cm^{-1}			
$4s^2\ ^1S_0$	0.00 (0.0)	$5p\ ^2P_{\frac{1}{2}}$	7.505 (60535.0)	-0.001 (-8.1)
$4s^2\ ^1S_0$	0.00 (0.0)	$5p\ ^2P_{\frac{3}{2}}$	7.515 (60613.2)	0.01 (81.3)
$3d\ ^3D_1$	2.521 (20335.344)	$7s\ ^2S_{\frac{1}{2}}$	9.851 (79449.9)	-0.176 (-1417.25)
$3d\ ^3D_2$	2.523 (20349.247)	$7s\ ^2S_{\frac{1}{2}}$	9.851 (79449.9)	-0.178 (-1431.25)
$3d\ ^3D_3$	2.526 (20370.987)	$7s\ ^2S_{\frac{1}{2}}$	9.851 (79449.9)	-0.180 (-1453.00)
Ba	I.P. 5.210 eV, 42032.4 cm^{-1}			
$6s^2\ ^1S_0$	0.00 (0.0)	$6g\ ^2G_{\frac{7}{2},\frac{9}{2}}$	8.48 (68425.87)	-0.078 (629.2)
$5d\ ^3D_1$	1.112 (9033.985)	$12g\ ^2G_{\frac{7}{2},\frac{9}{2}}$	9.62 (77628.0)	-0.098 (-789.7)
$5d\ ^3D_2$	1.112 (9215.518)	$12g\ ^2G_{\frac{7}{2},\frac{9}{2}}$	9.62 (77628.0)	-0.075 (-608.2)
$5d\ ^3D_3$	1.112 (9596.511)	$12g\ ^2G_{\frac{7}{2},\frac{9}{2}}$	9.62 (77628.0)	-0.028 (-227.2)
$5d\ ^1D_2$	1.413 (11395.382)	$21s\ ^2S_0$[b]	9.82 (79240.5)	-0.005 (-40.8)

[a] positive values indicate an endothermic process
[b] *Boulmer et al.* [1987]

Table 3.1b – Energy Deficits for Charge Exchange Channels				
Neutral State	Energy [eV (cm^{-1})]	Ion State	Energy [eV (cm^{-1})]	Deficit[a] [eV (cm^{-1})]
Sr	I.P. 5.692 eV, 45925.6 cm^{-1}			
$5s^2\ ^1S_0$	0.00 (0.0)	$7s\ ^2S_0$	8.053 (64964.1)	-0.131 (1053.0)
$4d\ ^3D_1$	2.251 (18159.056)	$7g\ ^2G_{\frac{7}{2},\frac{9}{2}}$	10.17 (82090.4)	-0.0025 (-20.2)
$4d\ ^3D_2$	2.260 (18218.795)	$7g\ ^2G_{\frac{7}{2},\frac{9}{2}}$	10.17 (82090.4)	-0.005 (-39.5)
$4d\ ^3D_3$	2.271 (18319.267)	$7g\ ^2G_{\frac{7}{2},\frac{9}{2}}$	10.17 (82090.4)	-0.017 (140.0)
$5p\ ^3P_0$	1.775 (14318.52)	$8d\ ^2D_{\frac{5}{2}}$	9.756 (78702.4)	-0.063 (508.2)
$5p\ ^3P_1$	1.798 (14504.35)	$8d\ ^2D_{\frac{5}{2}}$	9.756 (78702.4)	-0.040 (322.7)
$5p\ ^3P_2$	1.847 (14898.56)	$8d\ ^2D_{\frac{5}{2}}$	9.756 (78702.4)	0.009 (72.6)
$4d\ ^1D_2$	2.498 (20149.7)	$11d\ ^2D_{\frac{3}{2},\frac{5}{2}}$	10.43 (84144.9)	-0.014 (112.9)

[a]positive values indicate an endothermic process

3.4 Associative Ionization

Lai et al. [1992a] have suggested that associative ionization collisions of Ba (and therefore presumably Ca and Sr) with O may be an important process in ionospheric CIV releases. They introduce two reaction paths that result in the creation of Ba ions that are not the result of CIV,

$$Ba + O \rightarrow BaO^+ + e^- \tag{3.13}$$

followed by either

$$BaO^+ + h\nu(\lambda < 172.0 \text{ nm}) \rightarrow Ba^+ + O \tag{3.14}$$

or

$$BaO^+ + h\nu(\lambda < 190.8 \text{ nm}) \rightarrow BaO^{2+} \tag{3.15}$$

$$BaO^{2+} \rightarrow Ba^+ + O^+ \tag{3.16}$$

They stress the important point that for the altitudes of chemical releases, the neutral oxygen density is generally greater than the oxygen ion density by an order of magnitude or more. Since associative ionization is a reaction with neutral O, even if its cross section is less than that of charge exchange, the difference in densities can cause the reaction rate for associative ionization to be comparable to or greater than that for charge exchange. The discussion naturally falls into two parts; 1) the cross section for the actual associative ionization reaction (Equation 3.13), and 2) the rate of dissociation of BaO^+ into Ba^+

Associative Ionization

The cross section for associative ionization used by *Lai et al.* [1992a] are based on the experimental results of several heavy elements, including, U, Th, Sm and Nd, colliding with O [*Fite et al.*, 1977] The cross section for associative ionization for U and O is measured to be about 1×10^{-15} cm^2. The cross sections of *Fite et al.* [1977] are for thermal speeds, which are much less than the release speeds of 10 km/s.

Ringer and Gentry [1979] examined the associative ionization cross section for collisions of N with O. They found that the cross section peaks at values of 6×10^{-17} cm^2 at center of mass kinetic energies of about 10 eV. Above 10 eV, the cross section drops rapidly to less than 1×10^{-17} cm^2 by 20 eV. They speculate

that other collisional processes, including charge stripping and charge exchange (resulting in a negative ion of O), dominate over associative ionization above their threshold energies, which are about 10 eV. It is interesting to note that the reaction studied by *Ringer and Gentry* [1979] is endothermic by 0.38 eV in the center of mass frame, while that for Ba and O (both in their ground states) is endothermic by 0.68 eV in the center of mass frame. The threshold energy for stripping of Ba in the center of mass frame is 5.2 eV. While it is tempting to compare the results from the study by *Ringer and Gentry* [1979] to the Ba + O system, they differ in scale due to the large mass of Ba. A center of mass energy of 10 eV in the Ba + O system corresponds to ≈ 96 eV in the lab frame, or 35 km/s for Ba. This is well above the release velocities. It is important to note, however, that the peak cross section is less than 1×10^{-16} cm^2 for a reaction with an endothermic threshold energy comparable to that of Ba + O. The two endothermic associative ionization reactions listed in *Lai et al.* [1992a] have cross sections of 1×10^{-17} cm^2 and 1×10^{-18} cm^2. Based on these results we would expect the cross section to be less that 1×10^{-16} cm^2

Lai et al. [1992a] calculate the ratio between the reaction rates for associative ionization and charge exchange using the two values, 1×10^{-15} cm^2 and 1×10^{-17} cm^2, for their estimate of the associative ionization cross section for Ba + O, and a charge exchange cross section of 1×10^{-15} cm^2 The ratio is found to be between 10^4 and 10^2, for $n_O/n_{O^+} = 10^4$, The ratios n_O/n_{O^+} for the two CRRES releases were ~ 17 for G-13 and ~ 10 for G-14. These result in an associative ionization to charge exchange ratio between 17 and 0.17 for G-13 and 10 and 0.1 for G-14, for the same charge exchange cross section. These are much less than what they calculate for a 'typical' release, but represent a significant loss of neutral Ba from the release compared to charge exchange.

Dissociation of BaO^+

So far the discussion has been about the production of BaO^+. Part of the argument of *Lai et al.* [1992a] is that ions produced by the dissociation of BaO^+ by sunlight will be indistinguishable from those created by CIV or other collision processes. For associative ionization to be a major contaminant in ion inventories of the release, the two possible dissociation mechanisms must be relatively prompt. There is no information on the photo-dissociation cross section of BaO^+. The dissociation energy for BaO^+ is ≈ 4.6 eV to produce Ba^+ in its ground state. The dissociation energy for O_2 is 7.1 eV which is comparable to, though slightly greater than BaO^+. The dissociation rate for O_2 is well known and *Chamberlain and Hunten* [1987]

report a rate of 4×10^{-6} per second per molecule in full sunlight. Even if the dissociation rate for BaO^+ is a factor of 10 greater than for O_2, the time constant for creating Ba^+ from associative ionization by means of photo-dissociation will still be $\approx$ 25,000 s, or around 400 minutes.

The other method of creating barium ions via associative ionization is by photo-ionization of BaO^+. *Lai et al.* [1992a] make use of the photoionization of Ba^+ as a model for discussing the photoionization cross section of BaO^+, which is not known. The cross section for Ba^+ as measured by *Lyon et al.* [1986] is generally $< 1 \times 10^{-16}$ cm^2 between 10 and 30 eV photon energy with narrow peaks up to 1×10^{-15} cm^2. The solar irradiance in this same range is generally $\approx 1 \times 10^9$ cm^{-2} s^{-1}. The photoionization rate (the product of the two) is then on the order of 10^{-6} to 10^{-7} per second per molecule

If the true dissociation rate for Reaction 3.14, or the photoionization rate for Reaction 3.15 are high enough, there should be some evidence of associative ionization in the data. The minimum photon energies needed to either dissociate the molecular ion or to photoionize BaO^+ are 7.2 eV and $\approx$ 7 eV according to *Lai et al.* [1992a]. These correspond to wavelengths near 160.0 nm. The terminator for UV and EUV sunlight will be at a significantly higher altitude than that for visible light, by as much as 100 km [*Stenbaek-Nielsen*, personal communication, 1993]. If associative ionization is indeed the major process producing ions in below the terminator releases, there should be considerable gradients in the brightness of the resonant emissions in the ion cloud above the terminator. As will be shown in following chapters this is not observed.

The rate of associative ionization is seen to be comparable to the rate of charge exchange. However, the chances of detecting Ba^+ after dissociation of BaO^+ due to associative ionization seems low based on the comparison to two known rates of dissociation, and thus associative ionization is not expected to be a major contributor to the ion inventories of the CRRES releases. What may play a role in the analysis of these release are the emissions that may result from the associative ionization reaction. The energetics of the system may allow for the BaO^+ to be created in an excited state, and give rise to emissions. There is no information to be found on the spectrum of BaO^+ much less the cross section for excitation of emissions in the ion, but the possibility of such emissions must be entertained. There are several unidentified emissions in the spectra of early time sunlit Ba releases taken by *Stenbaek-Nielsen et al.* [1993]. These may be emissions from molecular species formed by associative collisions. Their appearance only at early times in

the releases indicates that their production and emission rates are low and must be observed when the release cloud densities are high.

An interesting aspect found while searching for associative ionization information on alkaline earths was that for reactions of $Ba^* + Ba \rightarrow Ba_2^+ + e^-$, where Ba^* is in a highly excited Rydberg state, *Kallenback et al.* [1988] estimate that the cross section is about 1×10^{-13} cm^2. In another work, *Liu and Olson* [1978] estimate that for Ca in a high Rydberg state ($n \geq 20$) the associative ionization cross section for $Ca + Ca^{**}$ is 1×10^{-14} cm^2. Note that if the associative ionization cross sections for Ba and Ca as estimated by these studies are indeed between 1×10^{-14} cm^2 and 1×10^{-13} cm^2, then this could be a large loss of Ba and Ca neutrals early in the release. The ions would still transit into sunlight and like BaO^+ would dissociate in sunlight. The dissociation energy of Ba_2^+ has not been reported, but is likely to be close to that of Ca_2^+ which has been calculated to be 1.04 ± 0.1 eV [*Liu and Olson*, 1978]. This puts the threshold wavelength for photo-dissociation well into the visible. This reaction is not expected to be important for releases however, since it requires an exotic high lying atomic state which is not likely for the temperatures involved in the releases.

3.5 Electron Impact Excitation

There have been numerous laboratory studies of electron impact excitation of atoms, ions and molecules, including all the species important to this study. Figure 3.7 shows the cross sections for excitation of individual line emissions in Ba. The cross sections are from *Aleksakhin et al.* [1975] and *Chen and Gallagher* [1976], and only the emissions with the largest cross sections are shown. The predominant emission is seen to be the 553.5 nm line. Figure 3.8 and 3.9 show the cross sections for Sr and Ca respectively [*Aleksakhin et al.*, 1974; *Starodub et al.*, 1973; *Garga et al.*, 1974]. These also show a single predominant emission line, but the cross section is not a factor of 100 above those of other emission lines, like that of Ba. The cross sections are for excitation of specific emissions and not for exciting Ba into specific states. This means that cross sections of lower lying transitions include cascades from higher states. This presents no difficulties since the line intensities, not the population of each state, are to be examined for the CRRES releases.

The excitation of the released ions will also be important for some of the calculations. *Zapesochnyi et al.* [1976] measured the cross sections for excitation of the resonance lines of Ba^+, Sr^+ and Ca^+. The cross section for the K line of Ca^+

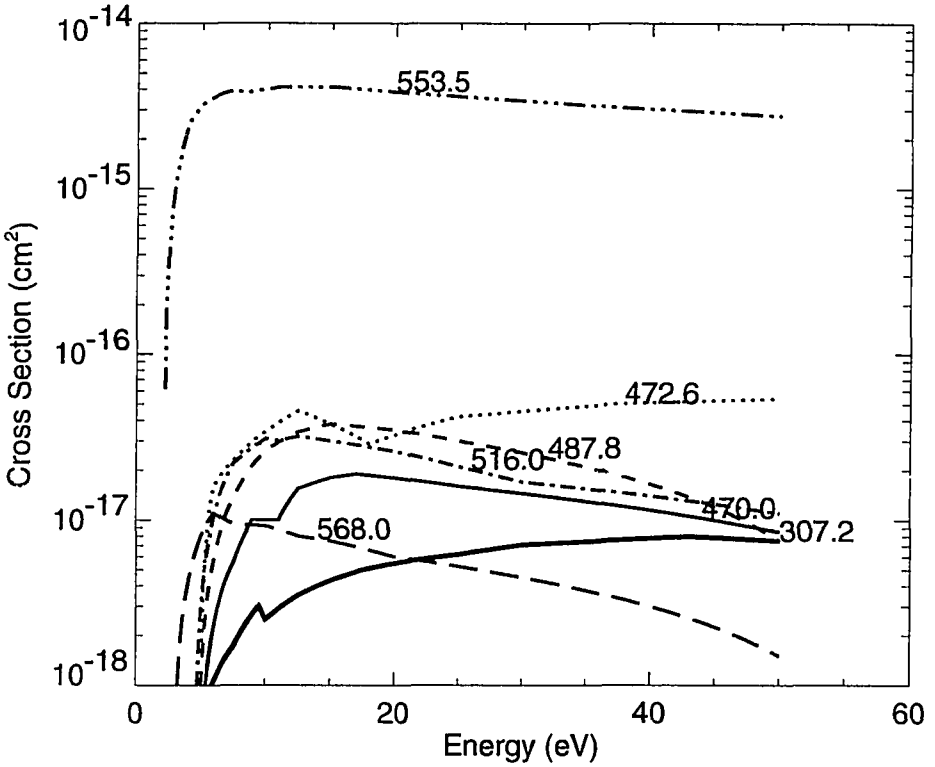

Figure 3.7: Electron impact excitation cross sections for Ba. The cross sections for the 553.5 and a representative selection of other emission lines are shown for energies between 0 and 50 eV. The emission wavelengths are indicated on the plot in nm. The data are from *Aleksakhin et al.* [1975]

compares well to the cross sections measured by *Taylor and Dunn* [1973] whose experiment, according to *Phaneuf* [1985, p. 117], "... must rank as one of the most meticulous absolute experiments to be performed in atomic collision physics"

Excitation of the ambient species will be an energy drain on heated electrons due to CIV. *Rees* [1989, Appendix 4] shows the excitation cross section for O, O_2, N, and N_2. Early in the releases, however, the density of the release material is much greater than the ambient densities, and it is not until several seconds after the burst that collisions with ambient species will be important.

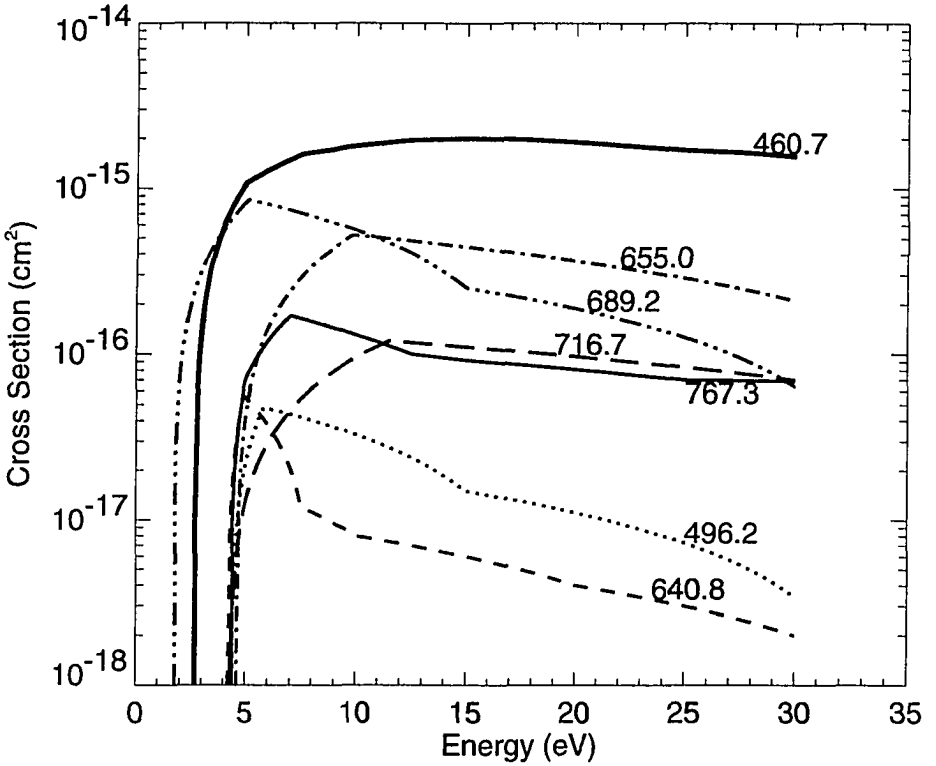

Figure 3.8: Electron impact excitation cross sections for Sr. The cross sections for the singlet transitions (460.7, 655.0, 716.7, and 767.3 nm) are from *Starodub et al.* [1973], and the triplet transitions (496.2, 640.8 and 689.2) are from *Aleksakhin et al.* [1974].

3.6 Electron Impact Ionization

Vaĭnshteĭn et al. [1972] measured the electron impact ionization cross section for Ba, Sr and Ca (as well as Mg). *Chen and Gallagher* [1976] show ionization cross sections for Mg, Sr and Ba, as well as some line excitation cross sections from collisions with their neutrals. They also measured the ionization cross section for Ca, but do not present the results. The ionization cross section vs energy are plotted in Figure 3.10. The excitation cross section of the resonant ion lines for ionizing collisions is also shown. The curve for the Ca^+ *K* and *H* emissions is produced from three parameters of *Vaĭnshteĭn et al.* [1972] who report the threshold energy for excitation, the peak cross section and the energy for the peak cross section. The curve is given a somewhat similar shape to the Ba^+ excitation cross section.

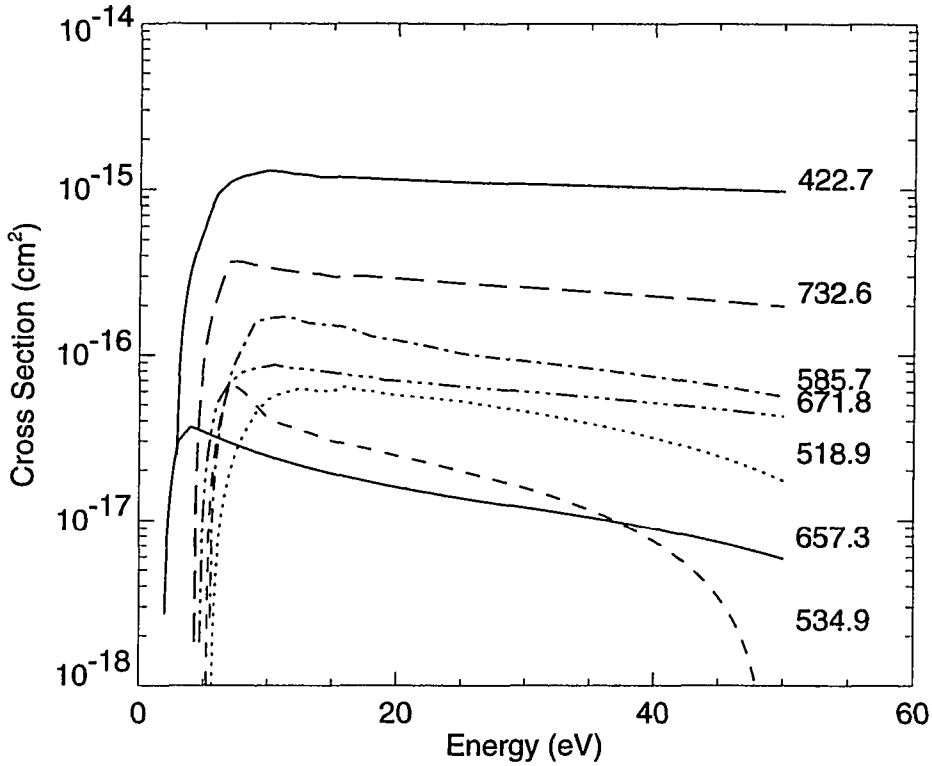

Figure 3.9: Electron impact excitation cross sections for Ca. The cross sections for the 422.7 nm and other emission lines are shown for energies between 0 and 50 eV. The emission wavelengths are indicated on the plot in nm. The data are from *Garga et al.* [1974].

3.7 Local and Total Reaction Rate Calculations

Since much of the analysis deals with collision rates, and especially ionization rates, for collisions between the release material and ambient species, it is instructive to establish how these rates are calculated. The arguments will be given in terms of a Ba release, but they apply equally as well to Sr and Ca. There are several cases where the assumption of either low density or small cross section leads to the use of a 'constant' ionization rate. The range of applicability of this assumption will be shown using some of the cross sections listed in this chapter.

In general, for a gas of two interacting species, the collision frequency is calculated using the full 6-D distribution function, $f(\mathbf{r}, \mathbf{v}, t)$, averaged over all di-

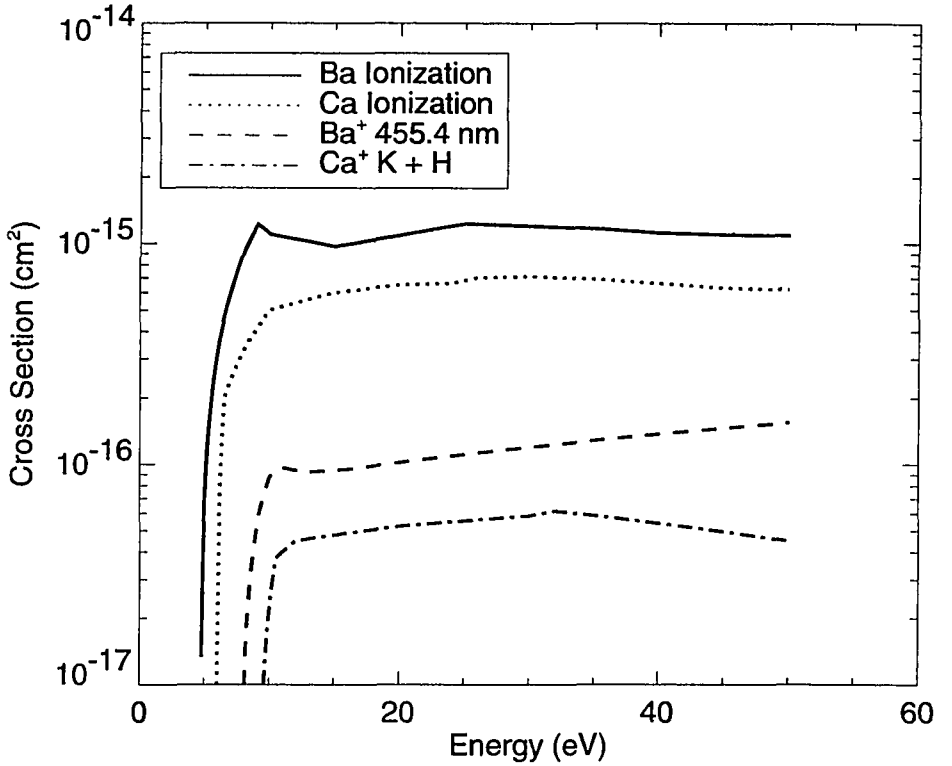

Figure 3.10: Cross sections for electron impact ionization of Ba and Ca. The ionization cross sections are from *Vaĭnshteĭn et al.* [1972] and *Chen and Gallagher* [1976]. The excitation cross sections for the ion lines of Ba and Ca from ground state neutral atoms are also shown from *Vaĭnshteĭn et al.* [1972].

mensions with the cross section and the relative velocity between the two particles. For two species, a and b, the collision rate, p, in collisions per unit volume per unit time, is found to have the following proportionality

$$p \propto \int\int f_a(\mathbf{r}_a, \mathbf{v}_a, t) f_a(\mathbf{r}_b, \mathbf{v}_b, t) |\mathbf{v}_a - \mathbf{v}_b| \sigma(|\mathbf{v}_a - \mathbf{v}_b|) d\mathbf{v}_a d\mathbf{v}_b \qquad (3.17)$$

If the gas is in thermal equilibrium, the distribution functions are taken to be Maxwell-Boltzmann distributions and the rate is found by completing the double integral.

For a chemical release we let species a be Ba, and assign species b the label O which may indicate either neutral or ionized oxygen, since at 500-600 km altitude these are the most abundant species. During a release, the Ba is moving relative

to the background atmosphere with a speed $v = |\mathbf{v}_O - \mathbf{v}_{Ba}|$ which is much greater than the average thermal speed of the ambient atmosphere. In this case the thermal speed of the atmosphere can be neglected and the velocity part of f_O can be approximated by a delta function. It was shown in Chapter 2 that the distribution of the CRRES releases is an expanding spherical shell (Equation 2.5). Locally the Ba neutrals have little relative motion so that, locally, the distribution is cold. Local means that the scale length of the volume under consideration is much less than the width of the spherical shell, v_{th}, described in Chapter 2. This cold distribution can also be approximated by a delta function, and the local collision rate is then found to be

$$p = n_O(\mathbf{r}) n_{Ba}(\mathbf{r}) v\sigma(v) \tag{3.18}$$

Many of the measurements made for the CRRES CIV releases are of the brightness of the entire release cloud. For collisional processes the emission rate of photons is directly proportional to the collision rate, so it is important to calculate the total collision rate for the release cloud. Since the cloud is of a finite extent the total collision rate, P in collisions per second can be calculated by integrating p over a volume V greater than the release cloud (which abstractly can be taken to be all space)

$$P = \int_{\mathsf{V}} n_O(\mathbf{r}) n_B a(\mathbf{r}) v\sigma(v) dV \tag{3.19}$$

The density of the background species, n_O can, in general, be taken to be constant, and can be taken out of the integration. One exception to this is shown in Chapter 5 where the depletion of the ambient O^+ due to charge exchange collisions is shown to be significant in the early part of the release. If the collision cross section is constant over the range of velocities in the release cloud, then it can also be pulled out of the integral, along with the average release velocity, $\langle v \rangle$, and the total collision rate becomes

$$P = n_O \langle v \rangle \sigma(\langle v \rangle) \int_{\mathsf{V}} n_B a(\mathbf{r}, t) dV = n_O \langle v \rangle \sigma N_{Ba}(t) \tag{3.20}$$

where N_{Ba} is the total number of released atoms. The total number of particles is given a time dependence to account for the loss of neutrals due to ionization (*e.g.* charge exchange, stripping) or collisions which result in molecular species (*e.g.* associative ionization)

To find the time dependence of N_{Ba} we must return to the local collision rate for ionization collisions. This will be equivalent to the change in the local neutral density per unit time, namely

$$\frac{dn_{Ba}}{dt} = -p = -n_{Ba} n_O v\sigma_i(v) \tag{3.21}$$

In Chapter 2 the density of the release cloud was found to be proportional to t^{-3} , and depend on radius from the center of the cloud, so that locally the ionization rate is actually

$$\frac{dn_{Ba}}{dt} = -p = -n_{Ba}(t)n_O v\sigma_i(v) \propto \frac{1}{t^3} \tag{3.22}$$

The ionization rate of the entire cloud can be found by integrating the equation over a volume V which is larger than the release cloud,

$$\int_V \frac{dn_{Ba}}{dt} dV = -\int_V n_{Ba}(t)n_O v\sigma(v)dV \tag{3.23}$$

Noting that this is an instantaneous relation, the time derivative can be taken outside the integral on the left hand side. The average velocity and cross section, σ_i are independent of coordinate, and it is assumed that n_O is locally uniform, so that this reduces to

$$\frac{dN_{Ba}}{dt} = -[n_O\langle v\rangle\sigma(v)]N_{Ba}(t) \tag{3.24}$$

where $N_{Ba}(t)$ is the total number of neutrals in the cloud at time t. The solution to this is a simple exponential function,

$$N_{Ba}(t) = N_{Ba}(0)\exp[-t/\tau] \tag{3.25}$$

where $\tau = [v\sigma(v)n_O]^{-1}$. For times $t \ll \tau$ the number of neutrals is very nearly the initial number of neutrals, and by Equation 3.24 the ionization rate is nearly constant. For the charge exchange, associative ionization and stripping cross sections for Ba and densities of their respective target species (O and O^+), the time constants are approximately 10^4, 10^3 and 10^6 seconds, much longer than the 30 to 40 seconds for which the time evolution of the ion and release clouds are observed. For Sr and Ca the numbers will be similar except for charge exchange of Ca with O^+, which has a near resonant charge exchange channel, and for which a cross section has been measured [*Rutherford et al.*, 1974]. In this case the large cross sections drops the time constant to around 70 s.

Chapter 4

Ion Clouds

Previous optical studies of CIV chemical releases in the ionosphere have used ion inventories from filtered images as the primary analysis [*Haerendel*, 1982; *Stenbaek-Nielsen et al.*, 1990a, 1990b; *Wescott et al.*, 1990, 1986b]. The inventories establish the ionization yield, the ratio of the total number of ions produced to the total number of neutrals released. The ion yield allows for a determination of the ionization rate and thereby a determination of the efficiency of the ionizing processes in the release. The analysis of the CRRES releases begins with this measurement.

It is apparent for the CRRES releases that there is an evolution to the ion cloud, both along the satellite track, and upward along the magnetic field line, and a more detailed analysis of the ion clouds will allow for a better understanding of the release dynamics. Both of these are evolutions in time, and some ambiguity could be possible without nomenclature. The two will be distinguished by the (somewhat arbitrary) labels of 'field-aligned evolution' for the ion density along the magnetic field and simply 'time evolution' for the change in ion density along the satellite track. To measure the field aligned evolution, the ion density along the field lines is compared to the distribution expected from the release pitch angle distribution and energy conservation as the ions move up along the field lines. The time history along the satellite track is used to determine the time after the release that the maximum ionization rate occurred. Much of the work presented here has been reported by *Wescott et al.* [1994] and in some cases the details of these calculations will not be repeated here.

4.1 Ion Inventories

Two quantities are needed to calculate the total number of ions in a digitized image: the intensity calibration for the image and the emission rates for the ion emission lines. Only images from filtered cameras are used for the ion inventories. The filters are constructed so that only one or two (in the case of Ca) ion emission lines will pass through the filter. The ion lines are well separated from other emissions lines, either ion or neutral, as well as most of the prominent airglow emission lines. For the intensity calibration, the stars in the image are used as standard intensity sources. Based on the magnitude and spectral type listed in the SAO star catalog [*Smithsonian Astrophysical Observatory*, 1969], the expected flux from a set of stars in the image is calculated and compared to the signal measured from the stars. The method is described in Appendix A. The emission rates for the ion line emissions are calculated from atomic data and the solar spectrum. Emission rates for Ba^+ have been calculated by *Stenbaek-Nielsen* [1989], who showed a major Doppler effect on emission rates in sunlight due to the motion of the ions and a strong Fraunhoffer absorption feature in the solar spectrum. For previous Sr releases, estimates of the 407.8 nm emission rates included 0.5, 0.2, 0.82 photons $ion^{-1}\,s^{-1}$ [*Deehr et al.*, 1982; *Wescott et al.*, 1990, 1994]. The CRRES G-14 Ca release being the first ionospheric Ca release, there had been no emission rates calculated. *Wescott et al.* [1994] calculated 0.38 photons $ion^{-1}\,s^{-1}$ for the K and H resonant lines (393.366 and 396.847 nm respectively) for the initial analysis of the releases.

The emission rates for all four CRRES releases are shown in Figure 4.1. The two Ba calculations are those used in *Wescott et al.* [1994], while the Sr and Ca are calculated for this work. The method used is that of *Stenbaek-Nielsen* [1989] which is a full examination of the equilibrium transition rate of each emission. The method includes effects of the solar spectrum, the gyromotion of the ion, and absolute motion of the ions relative to the sun. Emissions are assumed to be isotropic. The results are not significantly different than those presented by *Wescott et al.* [1994], but are included for completeness in Figure 4.1.

The inventories for the four ion clouds of the CRRES CIV release are now presented with a short description of the uncertainty in each measurement. The method of calculation (described in Chapter 2 and Appendix A) is to find the total count C in the image from the ion cloud, by finding the best estimate of the background and subtracting this from the image. The intensity scale found from the star calibrations is used to find a total emission rate for the cloud, and by means

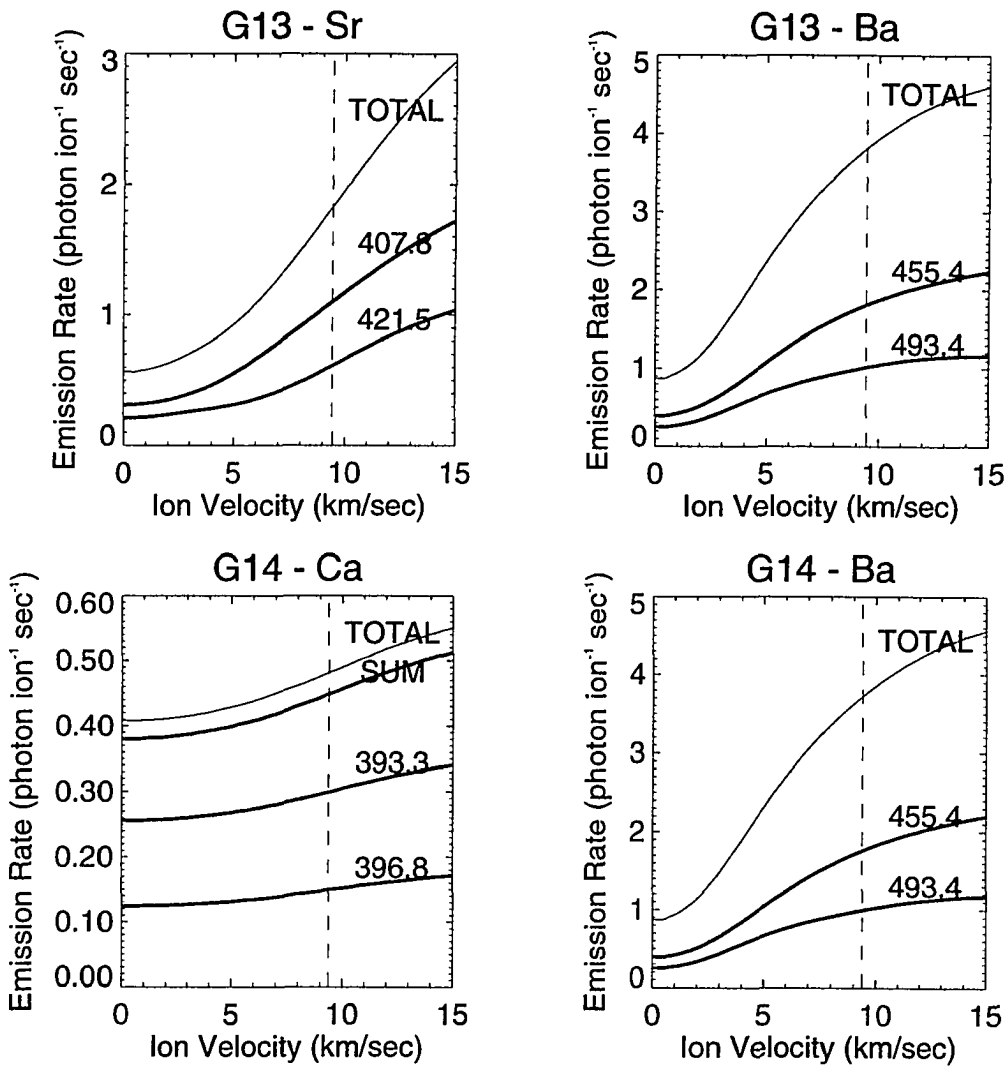

Figure 4.1: Emission rates for CRRES CIV releases. The emission rates versus velocity are shown for the CRRES releases. The emission rates for the prominent resonant lines are shown in each plot, as well as the total emission rate for all the emission lines in the model (labeled TOTAL). The filter for the Ca release included both the 393.3 and 396.8 nm lines, and for inventories the sum of these two emission rates is used (indicated in the plot).

of the calculated emission rate for an individual ion, the total number of emitters

The ion yield is found by dividing the ion inventory by the number of neutrals expected to be produced as vapor from the release cannister. The number used here, 40%, comes from preliminary tests of CRRES chemical release cannisters released from rockets from Wallops Is. [*Huba et al.*, 1992]. *Bernhardt et al.* [1993] used the same fraction in a model to study striations in a high altitude release, G-2, and found good correspondence to data. However, these two studies cannot verify the amount released for either G-13 or G-14. Hence the uncertainties listed are for the inventories and not the yields, since there is an unknown error in the number of total neutrals available in each release.

4.1.1 G-13 Sr

The ion inventory for the Sr release from the CRRES satellite has a very large uncertainty due to the fact that the intensity of the cloud was just at the detectability limit of the ICCD cameras. At approximately 2 minutes after the burst, the total number of ions in the image is measured to be 8.4×10^{21}, which is 0.02% of the total number of Sr neutrals available in the release. Uncertainties in the inventory approach 50% for the release based on the uncertainty in the star calibrations, and the small signal from the cloud.

4.1.2 G-13 Ba

The ion inventory for the second release of G-13 were taken from the IPDs. The star calibrations were fair (probably 10% uncertainty) as was the signal from the ion cloud in a 5 s integration. The number of ions seen above the terminator at about 2 min 30 s after burst was 9.6×10^{21}, corresponding to 0.15% of the total number of Ba neutrals expected from the release. The uncertainty in the inventory is less than 15% based on the star calibration and noise in the image.

4.1.3 G-14 Ca

As discussed in Chapter 2, the development of the Ca ion cloud was not captured, but at about 2 minutes the number of ions was found to be 3.1×10^{22}, corresponding to 0.27% of the neutrals expected in the release cloud. The star calibration was poor, but the inventories were consistent to within 10% between the two ICCD

cameras. The overall uncertainty in the inventory is thought to be better than 15% based on the consistency between the two ICCD images.

4.1.4 G-14 Ba

The Ba release of G-14 was the best documented ion cloud of the set. The ions were detected as early as 17 seconds after the release. The number of ions above the terminator at 2.5 minutes into the release was found to be 1.8×10^{23} which is 1.48% of the total number of neutrals expected for the release. The signal in the IPDs was quite strong so the uncertainty due to image noise is small. The star calibrations were also quite good ($\sim$ 10% uncertainty in the slope). Neither IPD could image the entire cloud so there is an unknown number of ions not inventoried.

4.2 Time Evolution of Ion Clouds

For both Ba releases the time evolution of the ion cloud has been examined. The satellite position was calculated at 2 second intervals after release. The magnetic field lines were traced from these points and are mapped to the image. Figures 4.2 and 4.3 show the mapped field lines from the Learjet ICCD for G-14 and G-13 respectively. The total intensity (and therefore ion inventory) between successive field lines is summed, and the results are plotted in Figure 4.4. Similar analyses of the Sr and Ca ion clouds were inconclusive due to the poor signal to noise ratio for these data.

There are some assumptions that go into the interpretation of the results of this measurement. The ions are expected to stay on the magnetic field line on which they were created. If there is any local electric field this assumption breaks down. There did seem to be some drift in all of the clouds, but is probably an overall drift due to large scale electric field. It is also assumed that the release cloud is smaller than the distance between successive field line traces. This is true only until 7 seconds after the burst, at which time the release cloud diameter is 18.8 km, the distance between successive satellite positions. No attempt was made to describe the effect that this had on observations. The most important observations occur within the first 10 seconds.

The general result for both releases is that the time evolution of the ionization rises quickly to a peak at 2 seconds for G-13 and 6 seconds for G-14. Both profiles then decay to a plateau of 5.5×10^{20} s^{-1} for G-13 and 3.5×10^{21} s^{-1} for

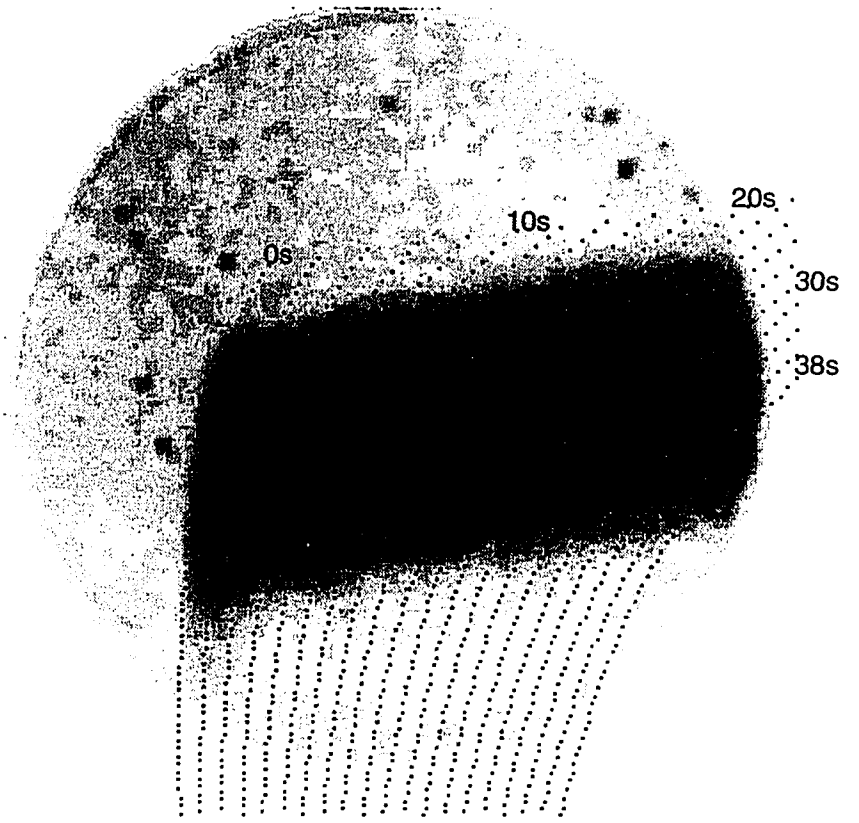

Figure 4.2: Field line traces for G-14 Ba from the Learjet. An IPD image from the Learjet at 2.5 minutes after the burst is shown with field line traces mapped from points at two second intervals along the satellite trajectory. The last field line is seen at 38 seconds, and the ion cloud is still seen at this field line. The distance between points along the field lines is 20 km.

G-14. The plateau is important since it indicates a constant ionization source, such as is expected for ionizing collisions with a uniform background. The sharp drop in ion inventories at later times is due to the edge of the image for both images The first field line for which the inventory is affected by the edge of the image is indicated by a vertical dashed line in the figure.

The decay from the peak ionization rate to the plateau looks approximately exponential, and a best fit to the profiles in these regions are shown in Figure 4.5. The decay distances, d, are shown in the figures. For G-13 the characteristic decay length corresponds to a decay time of 5 seconds, and for G-14 the decay time is 6.5 seconds. Using the derivations in Chapter 2, the cross section for the collision

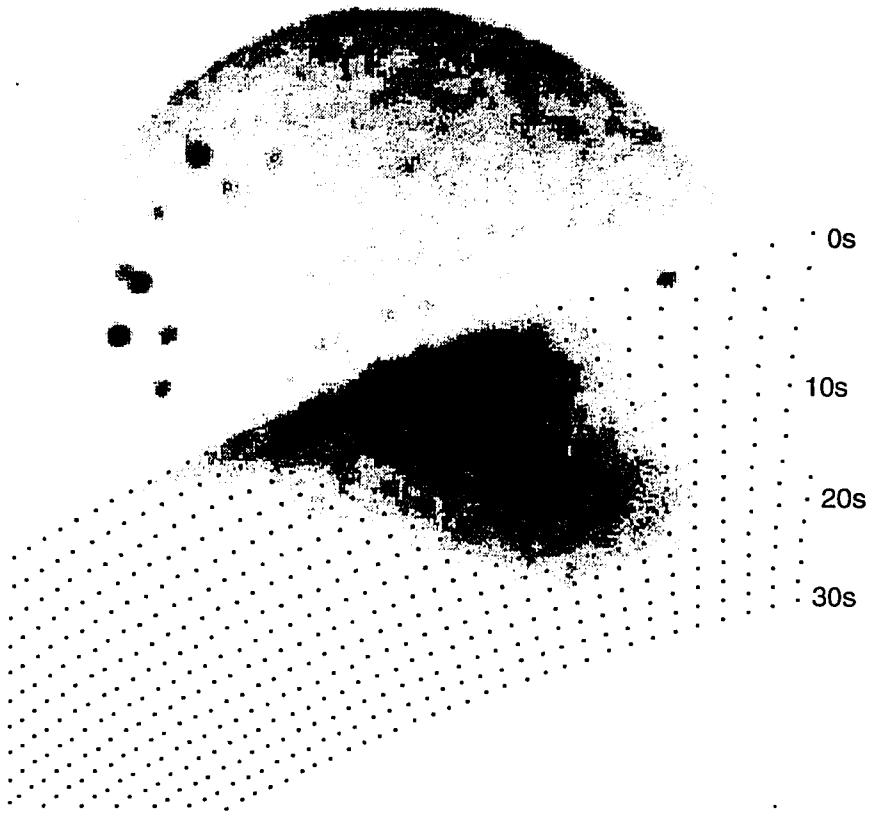

Figure 4.3: Field line traces for G-13 Ba from Learjet. An IPD image from the Learjet at two minutes after the burst is shown with field line traces similar to those in Figure 4.2. The satellite trajectory is out of the field of view of the image to the right hand side.

rates to produce such a decay can be calculated. The decay time is found to be

$$\tau = 1/n_s \sigma_i \langle v \rangle \tag{4.1}$$

where n_s is either O or O^+. The average velocity is taken as the satellite velocity $\langle v \rangle = 9.4$ kms^{-1}. There is a choice of collision partners for ionization – neutral oxygen and oxygen ions – and so the effective ionization cross section is calculated for both, for both releases. For neutral oxygen the required cross sections would be 4.2×10^{-15} cm^2 for G-13 and 6.5×10^{-15} cm^2 for G-14. For oxygen ions the required cross sections would be 6.1×10^{-14} cm^2 for G-13 and 1.0×10^{-13} cm^2 for G-14. These numbers alone would indicate that the decay is not due to depletion of the neutrals due to collisional processes. The cross sections are much larger than would be expected for ionizing collisions with either species. Further, the plateau

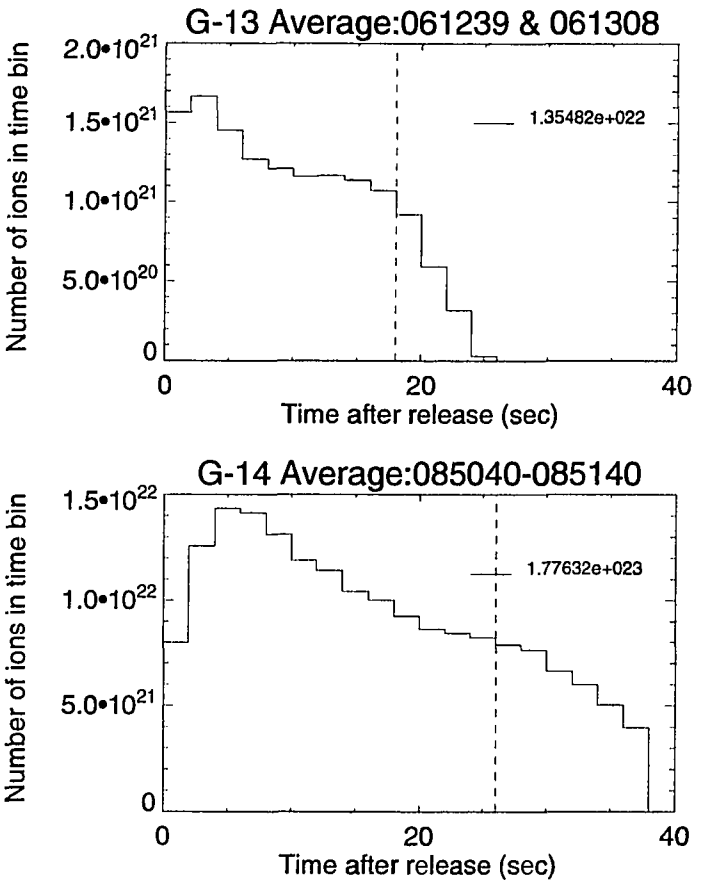

Figure 4.4: Time history of ionization rate. The total ion inventory between successive field lines shown in Figures 4.2 and 4.3 are shown. The upper plot shows the G-13 data and the lower plots shows the G-14 data. The dashed vertical line indicates where the edge of the image affects the ion inventory.

seen in both profiles indicates that the decay is due to a secondary process over and above collisional ionization with ambient species.

The Ba^+ cloud in G-14 is interesting in that the ions are still visible out to 40 seconds after the release. The ion density has reached a plateau after the initial peak. The ionization rate within the plateau is about 3.5×10^{21} per second. For ionization due solely to charge exchange this would correspond to a cross section of 5×10^{-16} cm^2, which is consistent with the cross section calculated in Chapter 3.

While a detailed measurement of the Ca^+ cloud was not done, a first order calculation of the ionization rate shows that there is less ionization than would be expected for charge exchange collisions. The ion cloud is seen to extend over 150 km from the release point, so that ionization was taking place for at least 15 seconds after the release. Dividing the ion inventory from Section 4.1.3 by 15 results in an ionization rate of $\sim 2 \times 10^{21}$ s^{-1}. This is much less than the $\sim 10^{22}$ expected for charge exchange collisions between Ca and O^+.

4.3 Field-aligned Evolution of the Ion Clouds

Ions that are created below the terminator are confined to and will begin gyrating about the magnetic field line. Knowing the mirror force of the magnetic field, the change in altitude along the field line, and the initial pitch angle of the ion, in theory one should be able to predict the subsequent motion of an ion along the field line. The only free parameter in the release is the pitch angle of the newly created ion. A comparison of the ion motion along the fieldline to the predicted ion cloud development provides information about the ion distribution.

Only for the G-14 release can the actual field-aligned *evolution* be examined. The G-13 Ba^+ cloud was not imaged until nearly 2 minutes after the release, by which time it was well developed. However, a snapshot distribution of ions along the magnetic field from individual images can be compared to what is expected from the release distribution and the time after the release.

The field-aligned evolution of the releases was examined most closely for the Ba releases, and is discussed by *Wescott et al.* [1994]. The evolution of the two Ba releases is found to match the calculated evolution based on the initial distribution, gravity, and mirror forces. There is a small energy loss in the distribution which is modelled as collisions with ambient neutral oxygen to good agreement. The model and results are discussed extensively in *Wescott et al.* [1994] and so will not be

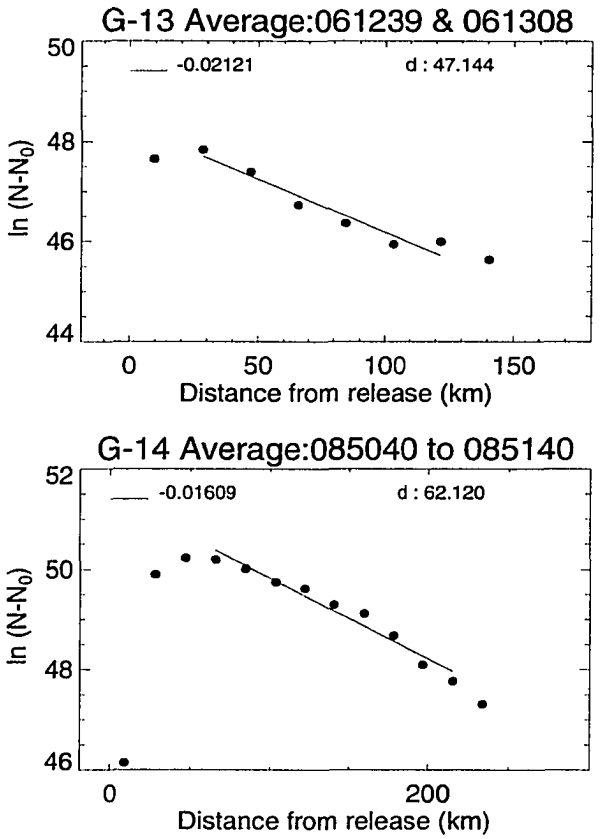

Figure 4.5: Decay of ionization rate. The first 12 seconds of the G-13, and the first 20 of the G-14 ion inventories is shown on a natural log plot. The data are roughly linear and the decay distance is shown in the upper right of each plot.

repeated here except for one further comment. The distance along the fieldline where the first signal is detected from the ion cloud matches closely to calculated distance to the terminator. The set of reactions resulting in barium ions due to associative ionization of Ba, as proposed by *Lai et al.* [1992a], would result in a dramatic increase in intensity of Ba^+ emissions lines at the H Lyman$-\alpha$ terminator (see Section 3.4), which should be at a higher altitude than the optical terminator needed to excite the resonant ion lines used to form the images. No dramatic change in intensity was seen at or greater than 100 km along the fieldline.

4.4 Evolution of Total Cloud Brightness

The ion inventories listed earlier are for discrete times after the release. Figures 4.6 and 4.7 show the time series of relative total brightness of the Ba ion clouds for G-13 and G-14 respectively from the IPDs of both aircraft. Five images at various times in the series are also indicated for both aircraft. All series show a fairly abrupt rise in the brightness, although the G-13 rise is artificial due to camera motion. All the series show a slow decay after reaching a peak at 1.5 minutes for G-13 and 3 minutes for G-14. The decay in the G-14 series is complicated by the fact that the ion cloud was larger in extent than could be completely imaged by the IPDs, but qualitatively shows the same form. The images in Figure 4.6 show that the ion cloud stayed within the field of view of the IPD for the G-13 release.

There are several possible explanations for this decay. First, a perpendicular electric field would result in an $\mathbf{E} \times \mathbf{B}$ drift, which could Doppler shift the ions into the very minimum of the solar Fraunhoffer absorption line. However it is difficult to envision a scenario in which the change in brightness would be so uniform. If there is no acceleration there should be no decrease in brightness for a constant number of ions. There is also no indication of motion of such magnitude as would be needed (kilometers per second) from triangulations of the leading edge of the ion cloud. Second, the decrease in total brightness could be due to image uncertainties. As the ion cloud spreads out along the field line, the surface brightness will decrease. As the signal drops into the noise inherent in the background it may become undetectable. However, the total image brightness is plotted and no attempt is made to find and subtract the background.

Third, the terminator is moving through the ion cloud. From calculations of the solar screening height along the release fieldline it is found that the terminator moves 170 km along the magnetic fieldline during the first 6 minutes after the

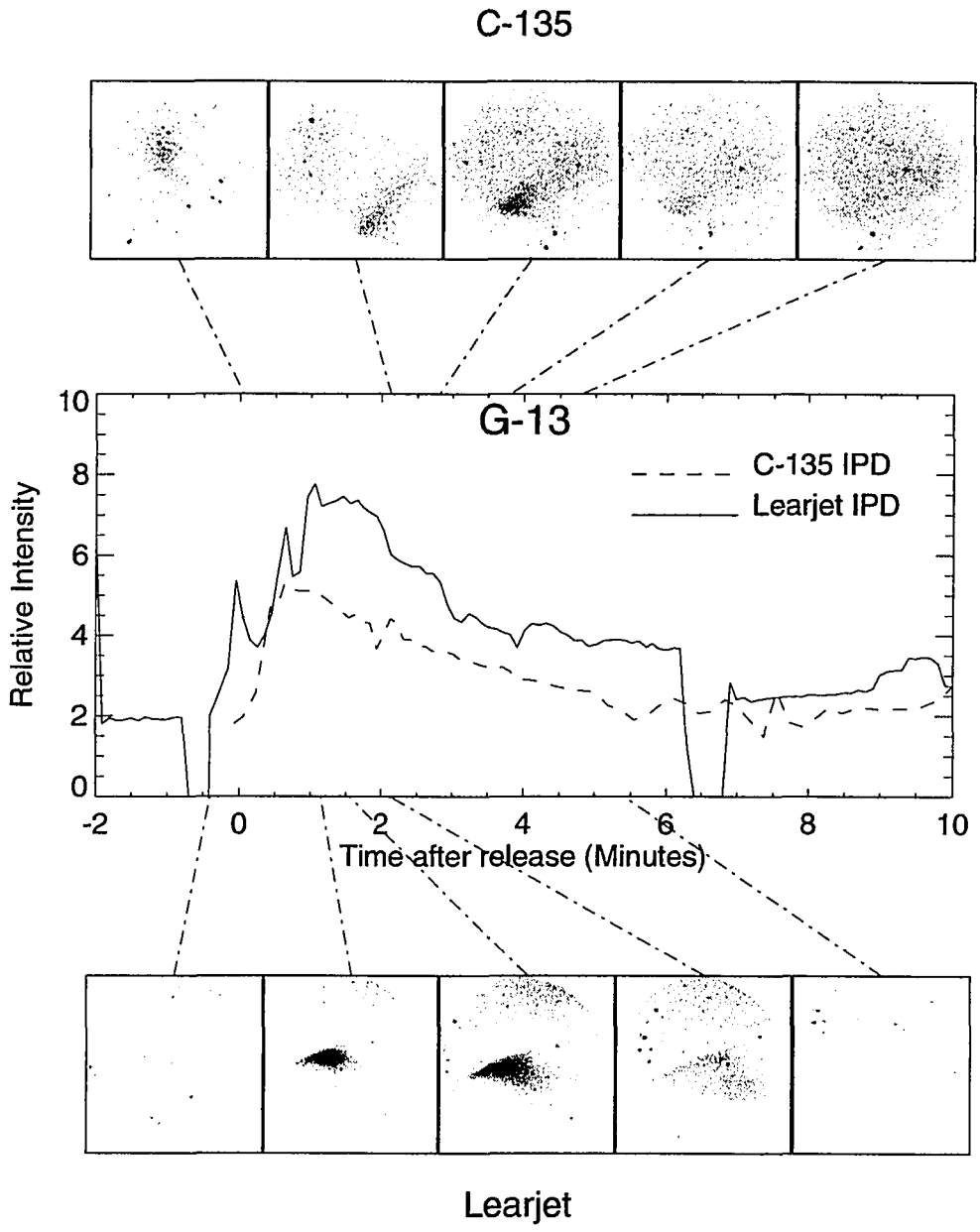

Figure 4.6: Time series of intensity of G13 ion cloud. The total intensity of each image in the series is plotted on an arbitrary scale. The upper images are from the KC-135, and the lower images are from the Learjet. The times are indicated by the line from each image to the time axis on the plot.

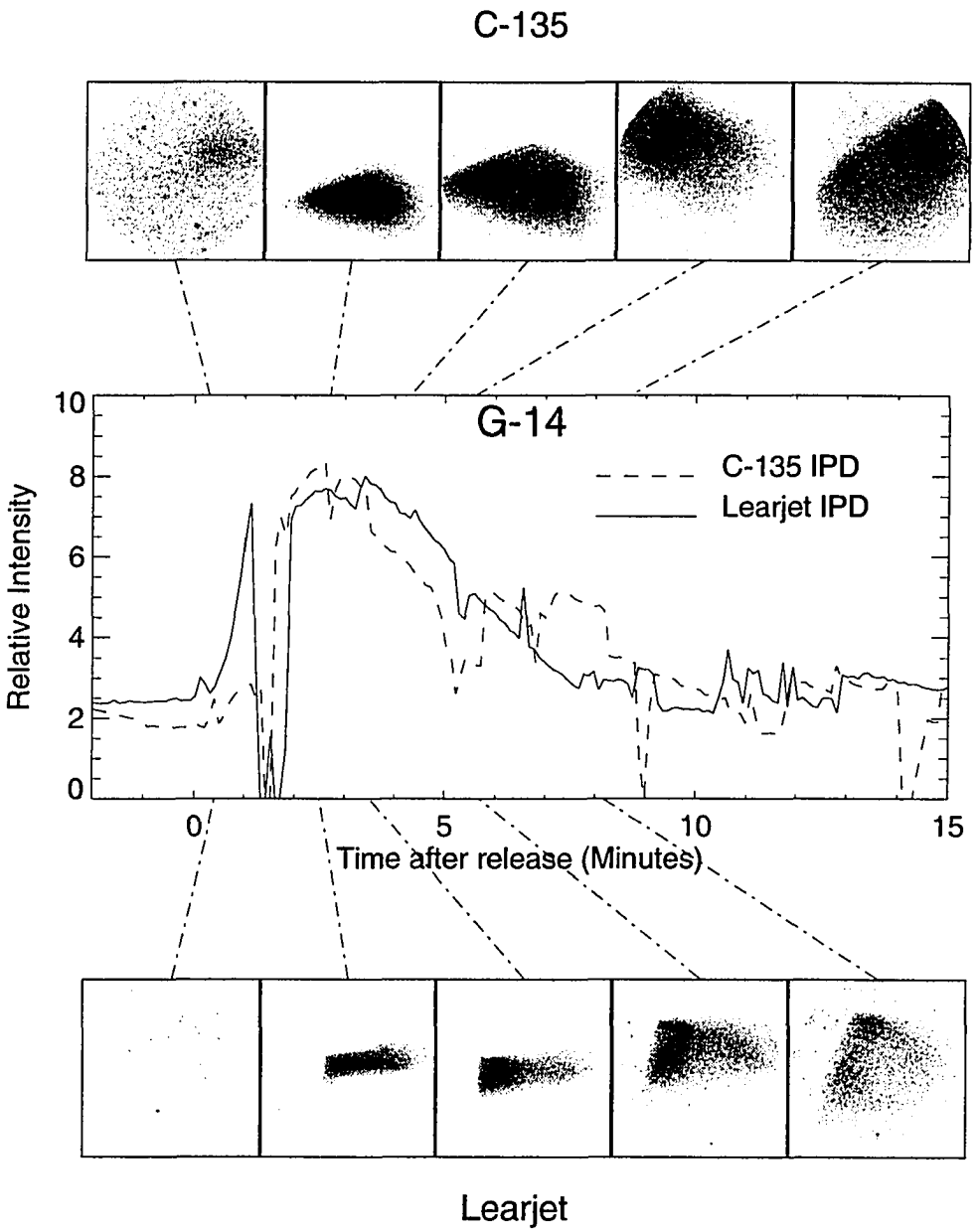

Figure 4.7: Time series of intensity of G14 ion cloud. The format is the same as that for Figure 4.6.

release. This corresponds to a speed along the fieldline of about 0.5 km/s. The parallel velocity from the center of the release is 1.6 km/s, so that most of the barium should be outrunning the terminator. However, the barium motion up the fieldline seems to have halted as seen in Figure 2.10.

Fourth, there could be a collisional loss mechanism for barium ions The intensity would be expected to decrease for a collisional loss mechanism, and in fact the time series should show an exponential decay. The time series of natural log of brightness is shown in Figure (4.8) for the C-135 IPD (the Learjet time series is compilcated by camera movements). The trace is seen to be linear in this plot indicating that the decay is exponential. The best fit to the data is shown as well with the decay time scale being about 350 seconds.

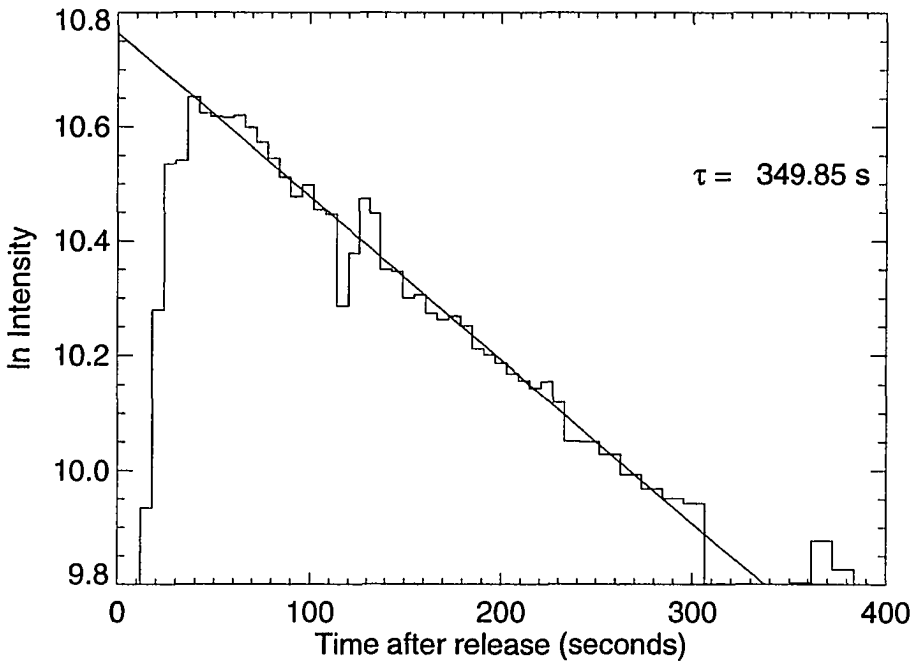

Figure 4.8: Decay of G-13 Ba^+ cloud intensity from KC-135 IPD. The first six minutes of the time series in Figure 4.6 is shown plotted on a log scale. The best fit is found to correspond to a time constant of 350 s.

Possible collisional loss mechanisms include recombination, charge exchange and chemical reactions. The reverse reaction with neutral oxygen does not have a

near resonant channel, and so the cross section is expected to be reduced compared to the reaction discussed in Chapter 3. The 350 s time constant indicates that the loss of Ba ions must be from reactive collisions, and not neutralization of Ba^+. Since the photoionization time constant for Ba is 28 seconds any neutral barium from a neutralizing collision will return to an ion on the 28 second time scale. However a reactive collision (e.g. $Ba^+ + M \rightarrow BaM^+$) may avoid this. One such collision studied is a reaction of Ba^+ with O_2 to form BaO^+ and atomic oxygen. The O_2 density at 500 to 700 km is low ($< 10^4$ cm^{-3}), but it is not unreasonable to think that the same reaction would happen with atomic oxygen. If the cross section is comparable, 1×10^{-16} cm^2, then the reaction rate would be between 10^{-3} and 10^{-2} s^{-1} for oxygen densities between 10^7 and 10^8 cm^{-3} and for Ba ions gyrating at $\sim$ 10 km/s (10^6 cm/s).

Further we note that the product of the 'abstraction' reaction with O introduced above is BaO^+, which *Lai et al.* [1992a] propose is the product of the first step of their two-step associative ionization scheme. The second step of this process is the photo-dissociation of BaO^+, which they argue will be prompt. If the loss of the Ba^+ in the G-13 release is due to the above reactive collision, then the time constant puts a limit on the photo-dissociation rate of BaO^+ at much more than 350 seconds - which is consistant with the analysis in Chapter 3.

However, *Milinevsky et al.* [1993] observe barium ions more than 10 hours after a release, for two different releases. For one release there were spectroscopic observations that confirmed Ba^+ emissions. These two releases were at lower altitudes than G-13 and G-14 and therefore would have higher collision frequencies with ambient species. If collisional losses happen in Ba releases, the clouds studied by *Milinevsky et al.* [1993] should have dispersed within this 350 second time frames as well. They clearly did not. Therefore it is most likely that the decrease in the ion cloud intensity is due to the advance of the terminator up the fieldline. The small dip angle of the field and possible slowing of the Ba^+, similar to that seen in G-14 would combine to reduce the emission rate of the ions, not the inventory.

Chapter 5

Release Clouds

All four release clouds were detected in the broadband B&W ICCDs and the Ba release clouds were seen in the filtered IPDs for 10s of seconds, while the cloud was in darkness, below the terminator. In Chapter 2 this light was shown to be line emissions of Ba for the G-14 Ba release, and is assumed to be similar for the other three releases. With the limited set of data a precise determination of the collisional processes alluded to above is not possible. But, there are several measurements that can give 'order-of-magnitude' or better determinations of the reaction rates and therefore collisional cross sections. This also allows for a new means by which to estimate the amount of ionization due to CIV.

5.1 Cloud Intensity vs. Time

Central to all of the measurements of the release cloud is the time series of the total cloud intensity. The overall evolution of the release cloud intensity, as seen from the KC-135 for the pair of G-14 releases, is shown in Figure 5.1. Each image from a 11.5 second sequence, starting one half second before the Ca burst, was digitized from video tape. A 150 × 150 pixel region, centered on the Ca release cloud was selected from the larger image. For the creation of the time series each of these images was divided in half along a horizontal division, creating an upper and lower half. The results are plotted in the upper panel of Figure 5.1 with labels 'upper half' and 'lower half'. The time scale is adjusted so that the Ca burst is at 0 sec, and the Ba release is seen at 2.5 seconds after the Ca burst. Plotted below this is a time series of the number of pixels that are saturated in the ICCD camera in each image. Below this are five 100 × 100 pixel sub-images in the time series,

with a line plotted from the top of each image to the time axis on the bottom plot indicating the time of each image. There is a horizontal line through all of the images indicating the separation between upper and lower half.

The choice of splitting each sub-image in two was meant to help distinguish between the contributions of the two release clouds. Since the Ba burst occurred below the Ca burst in this viewing geometry, the upper half should show a continuation of the Ca burst, independent of the intensity of the Ba burst below, until the Ba cloud has expanded into the upper half of the region. However, it is apparent in the plot that signal from the Ba burst does show up in the upper half at the time of the burst. This is due to light scattering in both the atmosphere and camera system, and can not be eliminated.

Both clouds begin with a very intense double pulse, which is the signature of the burning Ti and B propellant. A similar double pulse was observed in laboratory tests of the cannisters [*Stokes*, 1989]. The total integrated brightness of both release clouds is seen to rise to a peak at about 3 seconds after the release, and then begin to fall. This is more difficult to see in the Ca release, since the Ba burst at 2.5 affects the upper half of the image. There is also contamination by the Ba release cloud (fourth image from left) as it expands into the upper half of the images. However, from 1.25 to 2.5 s, the intensity of the Ca release is seen to be rising, and from 3.0 to 4.0 s, the intensity of the Ca release is seen to be falling in the upper half. During both of these periods, there is little contamination from the Ba release.

Before discussing the physical significance of these results it is imperative that any instrumental effects due to the performance of the ICCD be discussed. This is where the number of saturated pixels becomes important. While the cloud is saturated in the image, its expansion will cause a regular increase in total intensity. In fact, the total intensity should change as t^2, since the area changes as $\pi r^2(t)$, where $r(t) \propto v_0 t$. As seen in Figure 5.1, the number of saturated pixels drops drastically at 1.25 s, after which the total intensity is still seen to increase.

A non-linear gain in the ICCD would change the results of this measurement and alter the interpretations dramatically. Calibrations both in the lab and in the field have shown these systems to be linear [*T. Hallinan*, personal communication, 1995], and the star calibrations used to measure intensities (see Appendix A) show no signs of a non-linear response.

If the cameras are not artificially producing the rising intensities at early times in the release clouds, as seen in Figure 5.1, it remains to explain them by

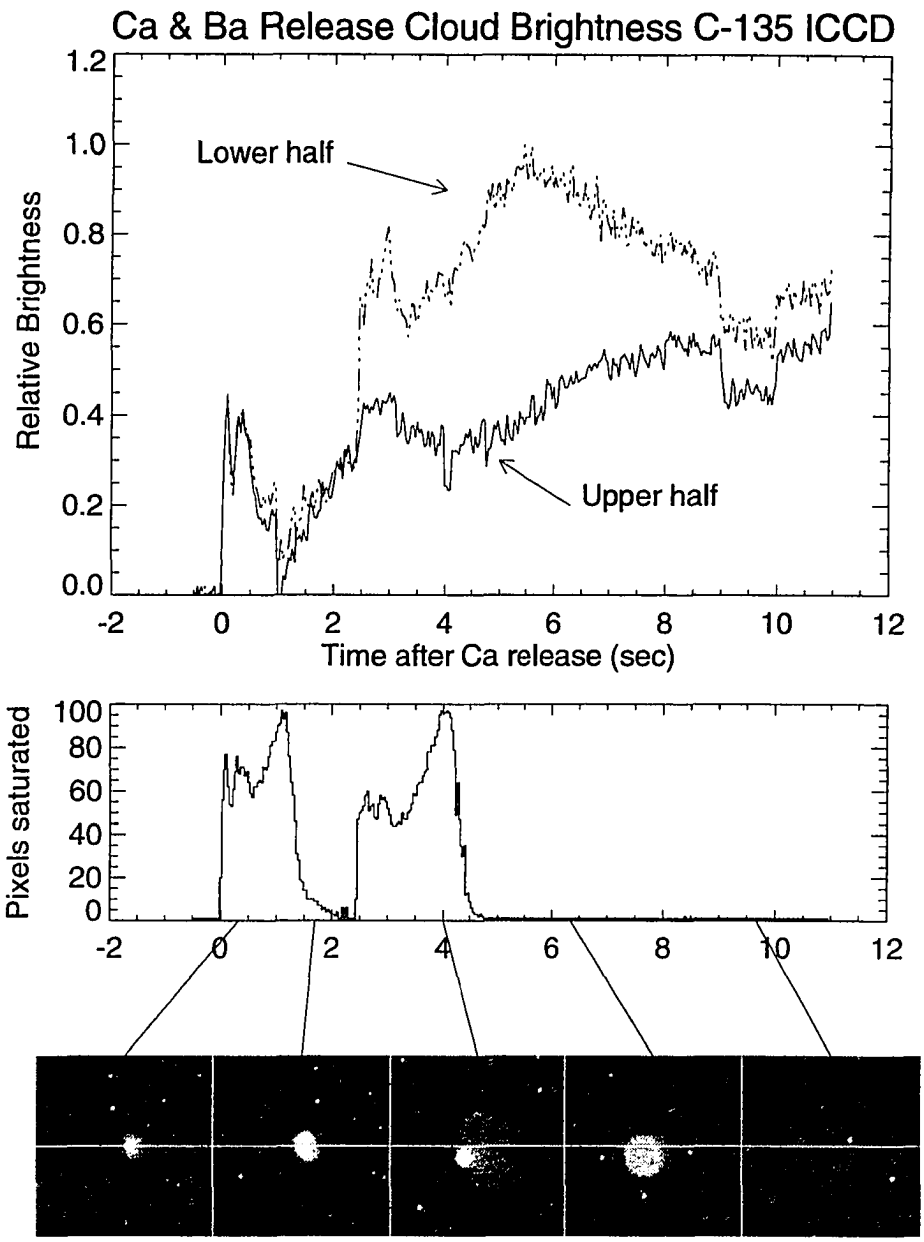

Figure 5.1: Time series of intensity of Ba and Ca release clouds. The upper plot shows the time series of the intensity of the release clouds as measured from the KC-135 ICCD. The lower plot shows the number of pixels saturated for each image. Five images on the bottom show representative times in the series. The times are indicated by lines from the top of each image to the time axis on the lower plot.

a physical model. The emissions are assumed to be due to collisions. The local collision rate with ambient species is proportional to the density of the release material. As shown in Chapter 3, while the density of the release material decreases as $1/t^3$, the volume that the release cloud encompasses, and therefore the total number of ambient particles included in the cloud, is proportional to t^3. Therefore the total emission rate due to collisions involving atmospheric species should be nearly constant, assuming the background densities are unaffected by the release. For collisions involving ions of the released material the emission rate should increase since the number of ions increases with time. However, the ionization rate is much less than 1% per second as measured in the ion yields. The majority of the collisions should be between neutrals and ambient species. This does not mean that the emissions are not from ion lines. Charge exchange, electron impact and neutral-neutral impact ionization will all produce populations of excited ions which will subsequently emit. Still, the original collision partner was a neutral metal atom.

5.1.1 Optical Depth

A rising intensity could be due to the cloud changing from an optically thick to an optically thin regime. This must be the case for neutral emissions early in the release when the neutral density is very high and most of the emissions originating from within the cloud will be absorbed and re-emitted one or more times before exiting the cloud. During each absorption there is a chance that the state will be collisionally deactivated or that the atom will radiate a different emission line. The question is at what time after the release does the cloud become optically thin? Ion lines will not be absorbed by the neutrals, and the ion density will not be high enough to absorb significant amounts of the emissions, so the calculation of the optical depth is only for neutral lines, and specifically for the Ba 553.5 nm resonant line. The results for the optical depth calculation for Sr and Ca will be similar, with the Ba emission case being an upper limit on the transition time owing to its much greater emission rate.

The radiative transfer problem of a thermite barium release was treated by *Drapatz* [1971] for the case of a release in sunlight. For a release in darkness the problem is to calculate the probability for a photon produced within the release cloud to escape without being absorbed and re-emitted. This means that the optical depth, τ, can be calculated in a straightforward manner since secondary scattering can be ignored. This calculation represents an upper limit on the time that the cloud

is optically thick, since there will have to be many absorptions and re-emissions for the emission rate to be substantially reduced.

For a radiative transfer problem in which there are only absorptions, the change in intensity along path s is proportional to the intensity,

$$\frac{dI_\nu}{ds} = -\alpha_\nu I_\nu \tag{5.1}$$

where the constant of proportionality, α_ν, is the absorption coefficient. The formal solution to Equation (5.1) is

$$I_\nu(s) = I_\nu(0)\exp\left[\int_0^s -\alpha_\nu(s')\,ds'\right] = I_\nu(0)e^{-\tau_\nu(s)} \tag{5.2}$$

where τ_ν is the optical depth at frequency ν, and $I_\nu(0)$ is the intensity of the emission at its point of origin. The absorption coefficient can be shown to be [*Rybicki and Lightman*, 1979]

$$\alpha_\nu(s) = n(s)\,\sigma_\nu \tag{5.3}$$

where n is the volume density of absorbers. The quantity σ_ν is the absorption cross section in the gas for radiation of frequency ν, and is defined as

$$\sigma_\nu = \frac{\pi e^2}{m_e c} f_{nm}\,\phi(\nu) \tag{5.4}$$

where ϕ is the spectral line width of the emission line, and f_{nm} is the oscillator strength for the transition. For a gas in thermal equilibrium, light of a given wavelength should see a uniform absorption cross section along its path since the relative motion will be centered around zero speed. But for the freely expanding cloud the particles at a distance s from s_0 will be moving, on average, at speed $(s - s_0)/t$. This will shift the center frequency of the absorption profile so it will be a function of not only the frequency, but of the distance from the source as well. The Doppler shift for velocity $v(s)$ is $\Delta\nu = \nu_0 v(s)/c$. The optical depth in Equation (5.2) becomes,

$$\tau_\nu = \frac{\pi e^2}{m_e c} f_{nm} \int_0^s n(s')\,\phi(\nu + \frac{\nu_0 s'}{c\,t})\,ds' \tag{5.5}$$

The Doppler frequency in ϕ is added to the source frequency indicating that the center wavelength of the gas at distance s' moves to lower frequency (or is red-shifted).

So far the line profile, $\phi(\nu)$, has not been specified, but there is a normalization constraint, namely,

$$\int_0^\infty \phi(\nu)\,d\nu = 1 \tag{5.6}$$

Drapatz [1971] argues that after an initial period of thermalization, the particles will have no interactions. In this case the spectral line width is that for a cold plasma, namely a Lorentz profile,

$$\phi(\nu) = \frac{\gamma/4\pi^2}{(\nu - \nu_0)^2 + (\gamma/4\pi)^2} \tag{5.7}$$

where γ is the lifetime of the upper state ($\gamma = \sum_{n'} A_{n,n'}$, where n is the upper state and the sum is over the lower states). There will be collisions with ambient oxygen which may broaden the natural line width. *Rybicki and Lightman* [1979] show that the effect can be approximated by adding twice the collision frequency to the factor γ above. Using a hard sphere cross section for collisions with ambient species, the collision frequency is found to be on the order 1×10^{-2} Hz, much less than the transition frequency, $A_{n,n'}$ for allowed transitions.

With the optical depth defined in Equation 5.5 the intensity of light expected along a path from any point in the cloud can be found. The intensity at frequency ν will be the total intensity distributed over the line width, $I_\nu(s) = I(s)\,\phi(\nu)$. So that the intensity along path s is simply,

$$I(s) = \int I_\nu(s) d\nu = I(0) \int \phi(\nu) \exp[-\tau_\nu(s)]\, d\nu \tag{5.8}$$

The shape of the Lorentz profile for the Ba 553.5 nm neutral line is readily calculated, so that all that remains to calculate the optical depth is to set the geometry. The symmetry of the release cloud reduces the problem to three parameters; 1) the radius from the center of the release cloud of the source region of the emission, 2) the angle between the line from the source region to the observer and the line from the source region to the center of the cloud, and 3) the time after the release, which specifies the density of the cloud. The geometry is shown in Figure 5.2. The angle from the source region in the cloud at radius, r, to the observer is defined as ψ. The zero of the angle is arbitrarily toward the center of the cloud. The integrating path, s, is toward the observer. The density in the cloud is a radial function, and finding the density along the path s requires finding the radius at any point along s, which is simply, $R(s) = \sqrt{r^2 + s^2 - 2rs\cos\psi}$, and is indicated in Figure 5.2.

The relative speed between gas particles at two points in the expanding gas cloud increases for increasing distance between the points. Thus the relative magnitudes of the width of the line resonance and the Doppler shift along a given path become important. This is shown in Figure 5.3 for $r = 0.9$ and $\psi = 180°$,

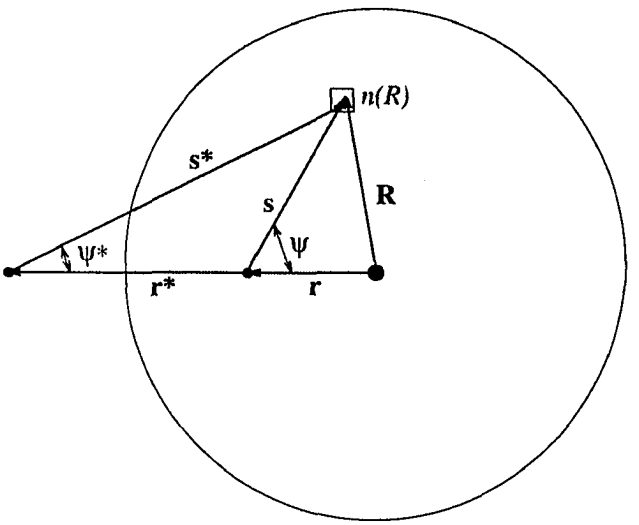

Figure 5.2: Geometry of optical depth calculation. The vectors **r** and **r*** are from the center of the release cloud to the point of origin of the emissions. The vectors **s** and **s*** are the distance along the path of integration. The vector **R** is from the origin to the current volume of absorbers along **s** or **s***.

which is near the peak of the density, and along a path directly away from the center of the cloud. Four traces of the line width, ϕ, are shown at distances along the path, s. The trace on the bottom is the distribution of the source emissions that will spread out along the path s. This trace is also the absorption profile at the emission source region. The other traces are the absorption profiles along the path s, and their peaks are seen to shift with distance along the path. The line widths and Doppler shifts are plotted to the same scale. Also plotted vertically is the relative density along the path with the zero at the center and greater density to the right. The purpose of the plot is to show that, within a very short distance from the source region, the absorption profile has Doppler shifted such that there is very little overlap between the emission and absorption profiles. Since the optical depth is a function of density, and the main component of the calculation comes from near the source region, the greatest attenuation should occur at the greatest density.

The optical transmission of the 553.5 nm Ba neutral line is plotted vs. time in Figure 5.4 for $r = 1.0$, and $\psi = 180°$, a path outward from the peak density. The attenuation is seen to dwindle rapidly, and is nearly zero at 0.15 seconds after the release. After this time the cloud will be optically thin to emissions created within

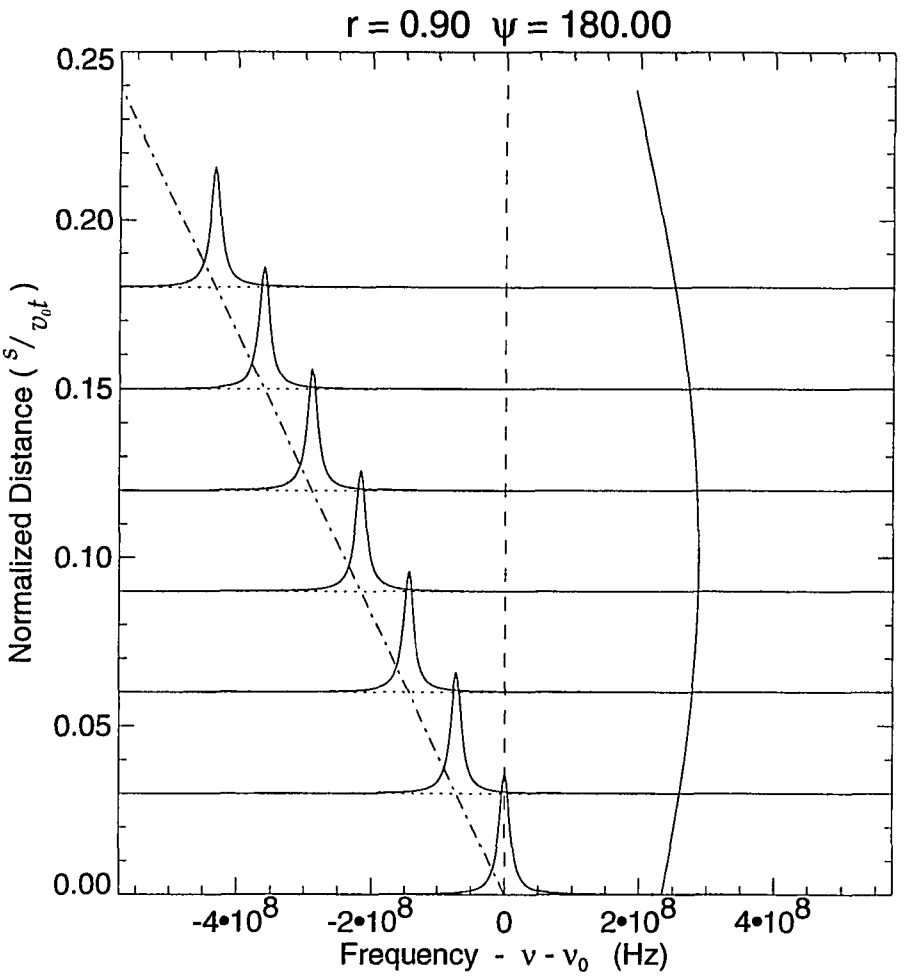

Figure 5.3: Line width vs Doppler shift along line of sight path. The emission profile is seen plotted at normalized distance 0. The absorption profiles are seen at various distances along an integration path. The overlap between the emission profile and the absorption profiles is seen to be small even at a short distance from the origin.

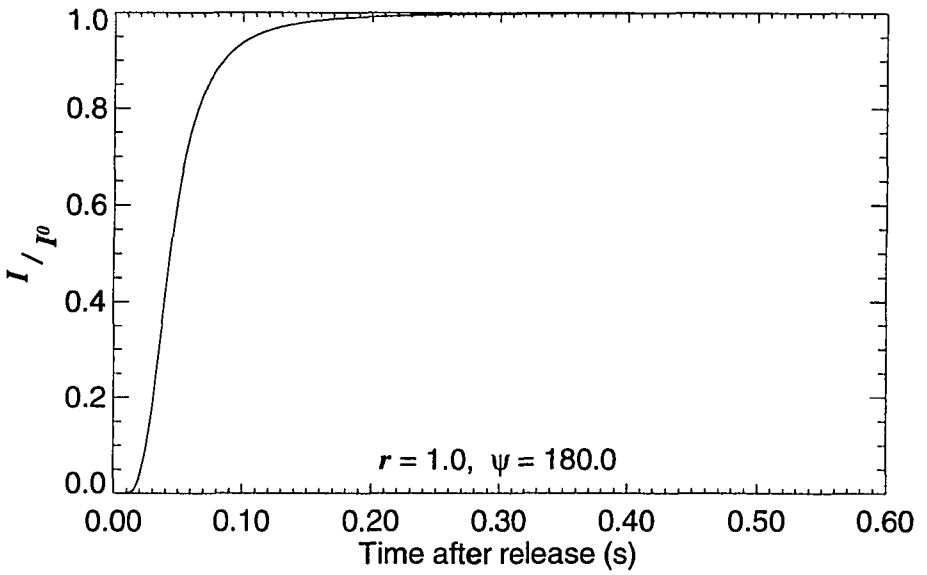

Figure 5.4: Transmission vs time for expanding Ba cloud. The transmission I/I_0 is plotted for a point at $r = 1.0$ along a path for $\Psi = 180.0°$. The attenuation is negligible at $t = 0.3$ seconds after the release, at which point the cloud will be optically thin.

the cloud. The gas ejection from the cannister is found to take nearly 0.2 seconds [*Stokes*, 1989] so that the optical depth of the Ba releases is not expected to be a significant contribution to changes in the intensity of the clouds.

5.1.2 Oxygen Ion Depletion Due to Charge Exchange

One effect of the high densities of the releases cloud at early times is that collisions that remove ambient species (*e.g.* $O^+ \rightarrow O$ in charge exchange) may deplete the entire population of the ambient species locally. Further, in cases where the total ambient population is severely depleted at the front of the release, the total number of emissions will be reduced from the constant rate described in Chapter 3. Like the optical depth, this effect of the 'collisional depth' is certainly happening in the early times of the CRRES CIV releases, and the question is how long does it last. Can this explain the rise in intensity of the release clouds?

The time history of the early release emissions due to charge exchange are

calculated using a 3-D particle model. The release cloud density is calculated using Equation 2.5 at each location in a 3-D grid, for a series of times. The expanding and translating release cloud interacts with a gas of O^+ with an initially uniform density. At each time step the change in O^+ density is calculated and the O^+ density is updated. The emission rate is directly proportional to the ionization rate for charge exchange so the total number of collisions is saved for each time step as well.

The ionization rate was shown in Chapter 2 to be

$$\frac{dn_{O^+}}{dt} = -n_{O^+}(\mathbf{r}, t) n_{Ba}(\mathbf{r}, t) \sigma_{cx} \langle v \rangle \tag{5.9}$$

where $\mathbf{r}$ is the position vector, t is the time after the burst, and $\langle v \rangle$ is the average velocity, taken to be the satellite velocity. Whereas n_{O^+} was assumed to be uniform in Chapter 2, for this calculation it must be a function of time and position. In the model, the change in n_{O^+} at time step $[j]$, is found by means of the difference equation of Equation 5.9

$$n_{O^+}[j+1] - n_{O^+}[j] = -n_{O^+}[j] n_{Ba}[j] \sigma_{cx} \langle v \rangle \Delta t \tag{5.10}$$

where both σ_{cx} and $\langle v \rangle$ are average values. The average velocity is the satellite velocity of 9.4 km/s. The charge exchange cross section is an adjustable parameter within the limits of the estimates found in Chapter 3. The total number of Ba neutrals is not modified for the model. As will be seen the total number of ionizations is less that 1% of the total number of neutrals so neglecting the loss of neutrals is a minor correction. No electrodynamic effects are considered in the model.

The results for three values of the charge exchange cross section are shown in Figure 5.5. Plotted is the total number of charge exchange collisions per second over the time of the model run. Even for the largest cross section, the emission rate is within 90% of its constant value within 1 second of the burst. Thus it is concluded that the collisional depth is not the source of the increase in intensity of the release clouds at early times for the Ba releases.

The results for a similar calculation of the intensity in the Ca release is shown in Figure 5.6. In this case the much larger cross section delays the time at which the emissions are close to the nominal emission rate. For this case the emissions reach 90% of the constant rate at about 1.8 seconds after the release. This is not far from the time which the Ca release is seen to reach its peak value, and so the rise time in the Ca release may be due to the collisional depth of the release cloud.

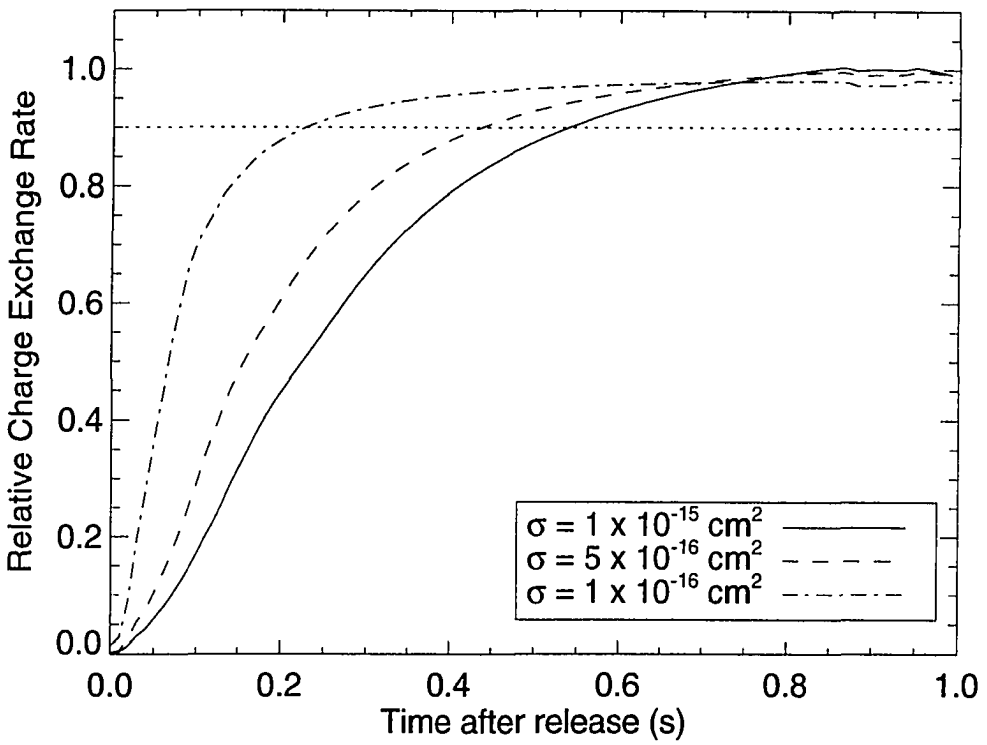

Figure 5.5: Early time Ba release cloud intensity due to charge exchange. The intensity is plotted for three values of the charge exchange cross section. All three cases reach 90% of the nominal intensity within 1 second.

5.2 Ratio Between Ba Ion Line and Other Emissions

All of the atomic collisional processes listed in Chapter 3 result in line emissions of various wavelengths that can be seen in the unfiltered ICCDs. Charge exchange, electron impact ionization, and neutral-neutral impact ionization will all result in a fraction of the collisions producing the 455.4 nm Ba^+ resonant line which can be seen in the filtered IPDs. The ratio of these two measurements gives a method to examine the collisional processes. Since the exact emissions measured by the ICCDs are not known and the ion line is not unique to a single ionization collision, each collision process cannot be determined precisely. Rather, the intensity expected for each type of collision is calculated for both cameras and the ratio of the two

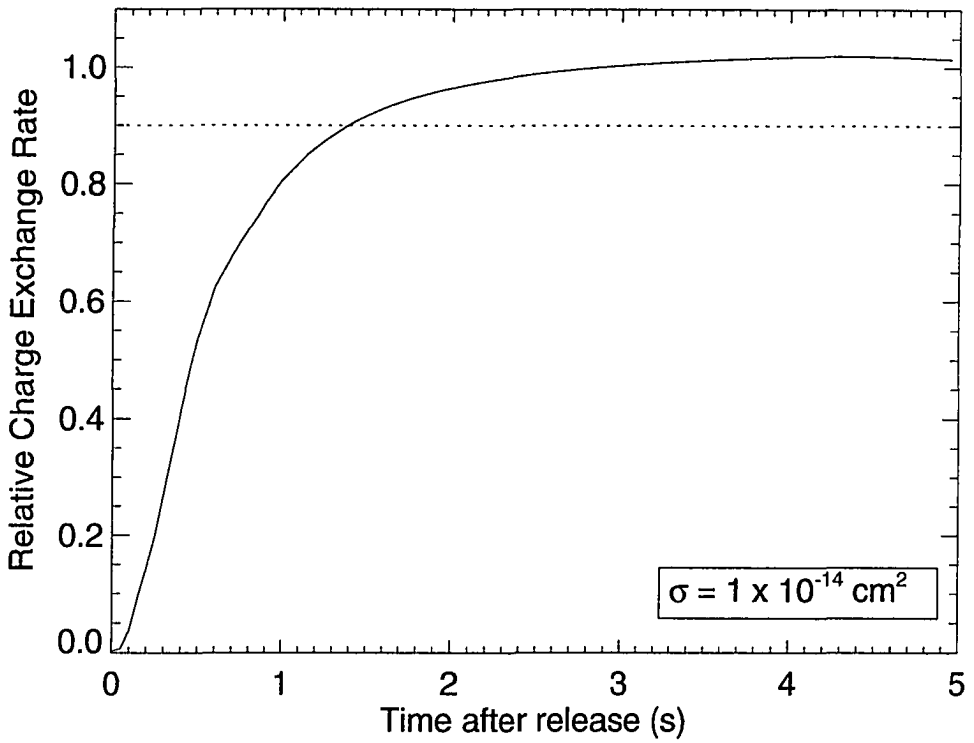

Figure 5.6: Early time Ca release cloud intensity due to charge exchange. The intensity is plotted for the intensity expected in the Ca release. The intensity is seen not to reach the constant rate (1) until nearly 1.8 seconds

is calculated. If one of these ratios is consistent with the measured ratio, it could indicate that the emissions are primarily from that collision, and the intensity will give another measure of the cross section for that collision in these releases. The calculations are made for the best known processes, charge exchange and electron impact.

5.2.1 Charge Exchange

For near resonant charge exchange collisions, the difference in ionization potentials between the alkaline earths and oxygen requires that the alkaline earth ions be formed in excited states. The excited states then relax to the ground state by way of a cascade of transitions, each producing a photon. The excited ions will have several possible transitions to their ground states and the task at hand is to find

the number of photons of each emission line for each charge exchange collision. The fraction that goes into a specific emission line is determined by its branching ratio, $B(j,k)$, which is the transition probability, $A(j,k)$, for that line divided by the sum of the transition probabilities for all the lines originating from the upper state,

$$B(j,k) = \frac{A(j,k)}{\sum_l A(l,k)} \tag{5.11}$$

The sum over l includes the state j. (Note that the upper state is the second index and the lower state is the first index, according to convention.) Each *individual* ion will relax to the ground (or metastable) state by way of one, and only one, of the possible paths and will emit one photon for each transition. The probability that the ion will cascade through a certain path is the product of all the branching ratios along that path. Thus, the probability for an ion producing a given emission is the product of the branching ratios up to and including the transition that produces the emission. This probability is then the fraction of ions in a population that will produce that emission. In some cases there are several possible paths that lead to an emission. In this case the fraction of charge exchange collisions that result in this emissions is the sum of the branching ratios, over all the paths leading to the upper state, multiplied by the branching ratio of the desired transition.

The branching ratios and fraction of photons have been calculated for Ba^+ and Ca^+. The Sr^+ calculation was not done since the Sr release cloud was only imaged with one camera, and for only a fraction of a second when the camera was not saturated. The results for Ca^+ are shown in detail to illustrate the method because the number of transitions is smaller. The method is identical (if more tedious) for Ba^+. None of the cameras was filtered for Ca lines (ion or neutral), and therefore there is no spectroscopic information for either of this release. The calculations are still needed to estimate the brightness of the release cloud due to the charge exchange ionization rate.

The Ca charge exchange collision has a reaction channel of small energy deficit that leaves the Ca ion in the $5p\ ^2P_{\frac{1}{2}}$ state. Transitions from this level have known transition probabilities [*Moore*, 1958]. The branching ratios are shown in Table 5.2.1, and the number of photons of each transition expected for each charge exchange collisions is shown in Table 5.2.1. The average number of photons expected for each charge exchange collision from all transitions is seen to be 2.84, and the total number of photons in the visible transitions (primarily the K and H lines at 393.3 and 396.8 nm) is seen to be 0.857. These must be convolved with the response function of the ICCD to predict the brightness of the release cloud due to

Table 5.1 – Branching Ratios for Ca Charge Exchange Cascade

Upper state[a]	Lower state[a]	λ (nm)	$A(j,k)(\times 10^8)$[b]	Branching Ratio
(5) $4^2P_{\frac{3}{2}}$	(1) $4^2S_{\frac{1}{2}}$	393.366	1.50	0.9317
(4) $4^2P_{\frac{1}{2}}$	(1) $4^2S_{\frac{1}{2}}$	396.847	1.46	0.9296
(5) $4^2P_{\frac{3}{2}}$	(3) $3^2D_{\frac{3}{2}}$	849.802	0.011	0.0068
(5) $4^2P_{\frac{3}{2}}$	(2) $3^2D_{\frac{5}{2}}$	854.209	0.099	0.0615
(4) $4^2P_{\frac{1}{2}}$	(3) $3^2D_{\frac{3}{2}}$	866.214	0.106	0.0704
(6) $4^2S_{\frac{1}{2}}$	(4) $4^2P_{\frac{1}{2}}$	370.603	0.84	0.3373
(6) $4^2S_{\frac{1}{2}}$	(5) $4^2P_{\frac{3}{2}}$	373.690	1.65	0.6627
(7) $4^2P_{\frac{1}{2}}$	(3) $3^2D_{\frac{3}{2}}$	213.143	0.018	0.0720
(7) $4^2P_{\frac{1}{2}}$	(2) $3^2D_{\frac{5}{2}}$	212.873	0.002	0.0002
(7) $5^2P_{\frac{1}{2}}$	(6) $5^2S_{\frac{1}{2}}$	1194.700	0.23	0.920

[a]Numbers in parentheses correspond to numbered states in Figure 5.7
[b]From *Moore* [1958]

charge exchange collisions.

The charge exchange collision between Ba and O^+ with the smallest energy deficit leaves the barium ion in an excited state $6g\ ^2G_{\frac{7}{2},\frac{9}{2}}$ state. Twenty-five transitions are used when calculating the branching ratios for the Ba cascade. There are over 50 emission lines that are excited, but for most the individual doublet states are averaged together. The $6p\ ^2P$ states were not averaged since the emission rate for the 455.4 nm line is needed. The branching ratios are listed in Table 5.3 and the states and transitions are shown in a Grotrian diagram in Figure 5.8. The transitions from the $5g\ ^2G$ state are listed in the Table even though no paths to this state are listed. There is a transition to this state from the $6f\ ^2F$ state with a calculated 6.1 μ emission line, which should have a very low transition probability. It is noted that any ions that reach this state will predominantly go to the $5d\ ^2D$ metastable state and not produce a 455.4 nm emission. Most of the transition probabilities have been tabulated by *Miles and Wiese* [1969]. The uncertainties in these values are reported to be less than 50% and some (*e.g.* 455.4 and 670.6 nm) are less than 25%. However, the transition probabilities of four transitions of high lying states are not listed, and a persistent search of the literature has failed to produce a laboratory measurement or theoretical calculation of these transition probabilities.

For the transitions not listed in the tables of *Miles and Wiese* [1969] or

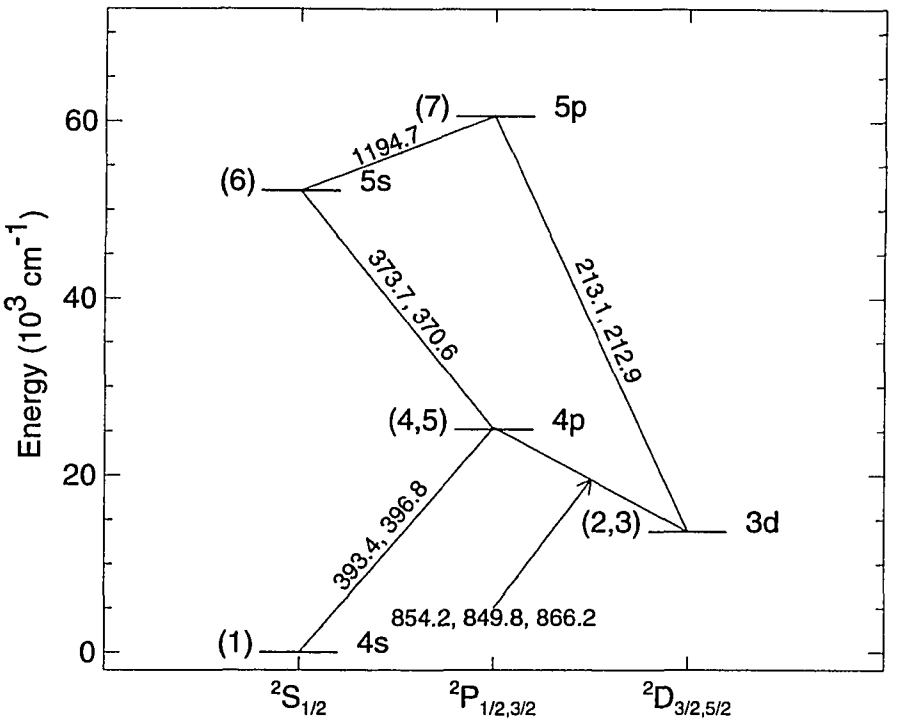

Figure 5.7: Partial Energy Level Diagram for Ca^+. The numbers in parentheses are used in Tables 5.2.1 and 5.2.1. The wavelengths of the transitions are shown in nm.

Moore [1958], the transition probabilities were calculated based on the quantum defect theory of *Kostelecky and Nieto* [1985]. The ions of the alkaline-earths have a configuration that is conducive to calculating the spectroscopic quantities. There is a single valence electron, the other electrons being locked in closed shells, similar to the alkaline metals. *Kostelecky and Nieto* [1985] used quantum defect theory to arrive at radial wave functions for the valence electron of alkaline atoms or alkaline earth ions, and these can be used to calculate the spectroscopic quantities needed for the cascade. *Djerad* [1991] lists the parameters needed for the calculations. A routine based on the methods outlined by *Kostelecky and Nieto* [1985] reproduces the known oscillator strengths well, but the calculations for the visible transitions from the $6g$ ^{2}G state may be unreliable. *Djerad* [1991] cautions that transitions to and from a state with low principal quantum numbers (n) may have poor accuracy.

Table 5.2 - Photon Yield for Ca Charge Exchange		
Wavelength (nm)	Path[a]	Fraction
393.366	$7 \rightarrow 6 \rightarrow 5 \rightarrow 1$	0.5681
396.847	$7 \rightarrow 6 \rightarrow 4 \rightarrow 1$	0.2885
849.802	$7 \rightarrow 6 \rightarrow 5 \rightarrow 3$	0.0041
854.209	$7 \rightarrow 6 \rightarrow 5 \rightarrow 2$	0.0375
866.214	$7 \rightarrow 6 \rightarrow 4 \rightarrow 3$	0.0218
370.603	$7 \rightarrow 6 \rightarrow 4$	0.3103
373.690	$7 \rightarrow 6 \rightarrow 5$	0.6097
213.143	$7 \rightarrow 3$	0.0720
212.873	$7 \rightarrow 2$	0.0080
1194.700	$7 \rightarrow 6$	0.9200
	total	2.8400

[a]Number Correspond to States in Figure 5.7

The $6g\ ^2$G to $4f\ ^2$F transition involves states with low principal quantum numbers. The transition is important for the ratio calculation since the emissions wavelength is $\sim$ 500.0 nm, near the peak sensitivity of the ICCD.

The calculated transition probability between the $6g\ ^2$G and the $4f^2$F state, $A(7,13)$, plays a key role in determining the ratio of the visible lines to the 455.4 nm line. The calculated transition probability, $1,45 \times 10^8$ s^{-1}, seems high and dominates the branching ratio of the top state in the cascade. Therefore the value of $A(7,13)$ has been assigned a range of values for the calculation of the emission ratios. Varying the value of $A(7,13)$ changes the ratio of all of the visible lines to the 455.4 nm emission line, as shown in Figure 5.9. For $A(7,13)$ between 0.1×10^8 and 2.5×10^8 s^{-1} this ratio ranges between 5 and 45. None of the listed transitions in Ba^+ has transition probability greater than 1.5×10^8 s^{-1}, so it is safe to say that 2.5×10^8 s^{-1} is a stringent upper limit on the possible values. The transition is allowed and the transition probabilities for other allowed lines is a few times 10^7 per second. The lower limit assigned to $A(7,13)$ is not a strict limit, but is thought to be closer to the true value, for which the ratios are around 5.

The measured ratio is between all the visible lines in the ICCD camera and the filtered IPD, which is imaging the 455.4 nm line. The calculated ratio was made comparable by multiplying the emission rate of each line by the relative response function of the ICCD at the wavelength of each line. The lines for $A(7,13) = 1.0$ are shown in Figure 5.10 with the response function of the ICCD.

Table 5.3 – Branching Ratios for Ba Charge Exchange Cascade

Upper state[a]	Lower state[a]	λ (nm)	$A(j,k)(\times 10^8\ s^{-1})$[b]	Branching Ratio
(13) $6g\ ^2G_{\frac{7}{2},\frac{9}{2}}$	(12) $6f\ ^2F_{\frac{5}{2},\frac{7}{2}}$	2650.4	0.16*	0.09
(13) $6g\ ^2G_{\frac{7}{2},\frac{9}{2}}$	(9) $5f\ ^2F_{\frac{5}{2},\frac{7}{2}}$	917.4	0.079*	0.05
(13) $6g\ ^2G_{\frac{7}{2},\frac{9}{2}}$	(7) $4f\ ^2F_{\frac{5}{2},\frac{7}{2}}$	498.9	1.45*	0.86
(12) $6f\ ^2F_{\frac{5}{2},\frac{7}{2}}$	(10) $7d\ ^2D_{\frac{3}{2},\frac{5}{2}}$	2084.2	0.14*	0.34
(12) $6f\ ^2F_{\frac{5}{2},\frac{7}{2}}$	(2) $5d\ ^2D_{\frac{3}{2},\frac{5}{2}}$	168.6	0.22†	0.54
(12) $6f\ ^2F_{\frac{5}{2},\frac{7}{2}}$	(6) $6d\ ^2D_{\frac{3}{2},\frac{5}{2}}$	538.0	0.051†	0.12
(11) $5g\ ^2G_{\frac{7}{2},\frac{9}{2}}$	(9) $5f\ ^2F_{\frac{5}{2},\frac{7}{2}}$	1818.3	0.21*	0.04
(11) $5g\ ^2G_{\frac{7}{2},\frac{9}{2}}$	(7) $4f\ ^2F_{\frac{5}{2},\frac{7}{2}}$	682.9	5.37*	0.96
(10) $7d\ ^2D_{\frac{3}{2},\frac{5}{2}}$	(8) $7p\ ^2P_{\frac{1}{2},\frac{3}{2}}$	994.5	0.44†	0.23
(10) $7d\ ^2D_{\frac{3}{2},\frac{5}{2}}$	(7) $4f\ ^2F_{\frac{5}{2},\frac{7}{2}}$	871.6	0.035†	0.02
(10) $7d\ ^2D_{\frac{3}{2},\frac{5}{2}}$	(4) $6p\ ^2P_{\frac{3}{2}}$	263.7	0.76†	0.39
(10) $7d\ ^2D_{\frac{3}{2},\frac{5}{2}}$	(3) $6p\ ^2P_{\frac{1}{2}}$	252.5	0.71†	0.36
(9) $5f\ ^2F_{\frac{5}{2},\frac{7}{2}}$	(6) $6d\ ^2D_{\frac{3}{2},\frac{5}{2}}$	872.7	0.88†	0.97
(9) $5f\ ^2F_{\frac{5}{2},\frac{7}{2}}$	(2) $5d\ ^2D_{\frac{3}{2},\frac{5}{2}}$	191.6	0.031†	0.03
(8) $7p\ ^2P_{\frac{1}{2},\frac{3}{2}}$	(6) $6d\ ^2D_{\frac{3}{2},\frac{5}{2}}$	2679.2	0.05*	0.09
(8) $7p\ ^2P_{\frac{1}{2},\frac{3}{2}}$	(5) $7s\ ^2S_{\frac{1}{2}}$	1342.1	0.20†	0.36
(8) $7p\ ^2P_{\frac{1}{2},\frac{3}{2}}$	(2) $5d\ ^2D_{\frac{3}{2},\frac{5}{2}}$	224.9	0.20*	0.36
(8) $7p\ ^2P_{\frac{1}{2},\frac{3}{2}}$	(1) $6s\ ^2S_{\frac{1}{2}}$	200.7	0.10†	0.18
(7) $4f\ ^2F_{\frac{5}{2},\frac{7}{2}}$	(2) $5d\ ^2D_{\frac{3}{2},\frac{5}{2}}$	232.3	1.48*	1.0
(6) $6d\ ^2D_{\frac{3}{2},\frac{5}{2}}$	(4) $6p\ ^2P_{\frac{3}{2}}$	414.5	3.1†	0.60
(6) $6d\ ^2D_{\frac{3}{2},\frac{5}{2}}$	(3) $6p\ ^2P_{\frac{1}{2}}$	387.3	2.1†	0.40
(5) $7s\ ^2S_{\frac{1}{2}}$	(3) $6p\ ^2P_{\frac{1}{2}}$	452.493	0.72†	0.38
(5) $7s\ ^2S_{\frac{1}{2}}$	(4) $6p\ ^2P_{\frac{3}{2}}$	489.993	1.2†	0.62
(4) $6p\ ^2P_{\frac{3}{2}}$	(2) $5d\ ^2D_{\frac{3}{2},\frac{5}{2}}$	602.3	0.371†	0.24
(4) $6p\ ^2P_{\frac{3}{2}}$	(1) $6s\ ^2S_{\frac{1}{2}}$	455.403	1.19†	0.76
(3) $6p\ ^2P_{\frac{1}{2}}$	(2) $5d\ ^2D_{\frac{3}{2},\frac{5}{2}}$	670.6	0.332†	0.26
(3) $6p\ ^2P_{\frac{1}{2}}$	(1) $6s\ ^2S_{\frac{1}{2}}$	493.409	0.955†	0.74

[a]Numbers in parentheses correspond to numbered states in Figure 5.8

[b]Values are †from *Miles and Wiese* [1969] and, * calculated for this work

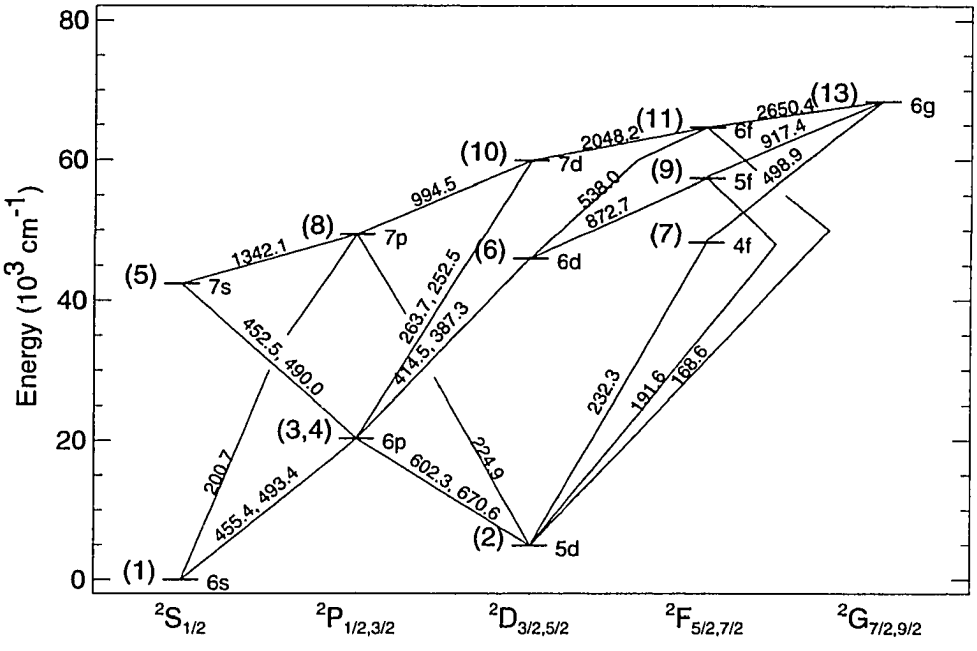

Figure 5.8: Partial Energy Level Diagram for Ba^+. The numbers in parentheses are used in Tables 5.2.1 and the wavelengths of the transitions are shown in nm.

5.2.2 Electron Impact Emissions

The ratio of the 553.5 neutral Ba line to the 455.4 nm Ba ion line can be calculated for electron impact excitation and ionization using the cross sections in listed in Chapter 2. Since the cross sections include the energy dependence, the ratio can be calculated for an arbitrary electron distribution. Simulations of the two-stream instability show that the electrons are heated and in some cases will have secondary 'high' energy peaks [*Machida et al.*, 1984; *Abe and Machida*, 1985]. Using the electron heating case first, the ratio of the 553.5 nm line to the 455.4 nm ion line is calculated for a range of temperatures. The relative emission rates of several neutral emission lines, as well as the ion lines are plotted vs electron temperature in Figure 5.11. The 553.5 emission line is seen to dominate for the electron impact case.

Torbert et al. [1992] measured the electron distribution in a rocket based CIV Ba release (CRIT II) and found not only a heated population of electrons ,

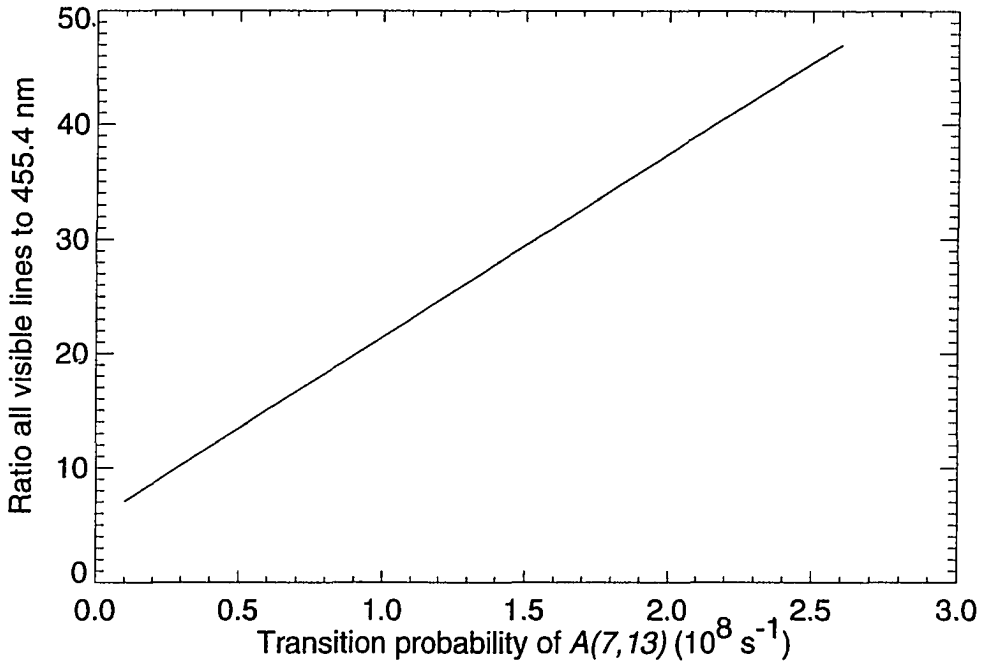

Figure 5.9: Calculated ICCD to 455.4 nm intensity ratio for charge exchange. The Einstein coefficient for the $6g\ ^2$G to $4f\ ^2$F ($A(7,13)$) is varied from 10^7 to 2.5×10^8 s^{-1} over which the ratio changes from 5 to 45.

but a set of quasi-gaussian tails centered at 10 eV and 80 eV. Both of these centers are above the threshold for electron impact excitation and ionization. At 80 eV the cross sections for both excitation and ionization into the 455.4 nm emission line are only slightly energy dependent, and the ratio is nearly constant for a wide range of energies. The ratio is found to be 40, and this can be taken as a lower limit on the possible ratios of 553.5 to 455.4 nm emission lines created by electron impact on neutral Ba.

5.2.3 Measurements

To measure the ratio of the signal from the ICCD camera to the signal from the IPD, there are two major obstacles to overcome. First is the difference in sampling rate of the two cameras. The IPDs took 5 second integrations for each frame, whereas the ICCD's were running at full TV frame rates of 30 frames per second. The broadband portion of the signal is highly oversampled compared to the IPD.

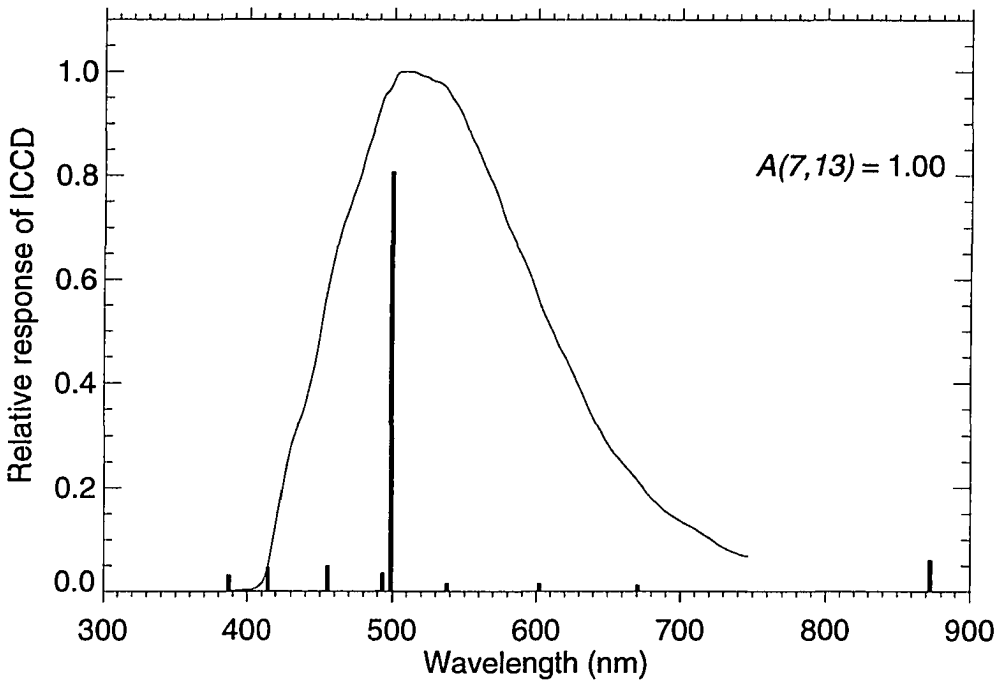

Figure 5.10: Intensities of individual lines compared to ICCD response. For $A(7,13) = 1 \times 10^8$ s^{-1} the intensities of the visible lines of the Ba charge exchange cascade are shown relative to the ICCD response function. Note the $6g$ ^{2}G to $4f$ ^{2}F emission at 499.0 nm dominates the emissions, and is near the peak in sensitivity.

Ideally the ratio of the ion line to the visible lines would be made at the highest possible sampling rate. Since the release cloud geometry is known it is, in principal, possible to reconstruct the time evolution of the ion line of the cloud at a higher resolution than five seconds. However if the emissions are due to a electron impact excitation, and the electron distribution is changing as a function of time then the ratio will be changing with time. The calculation is not done since it requires a detailed knowledge of the electron distribution, which is not known.

If the IPD signal cannot be subsampled, then the ICCD must be integrated. This is easily done in computer programs, but it points out the second problem; the mixing of the two release clouds. In order to compare similar quantities, the total brightness from *only* the Ba release needs to be found. But the Ba release takes place within the Ca release as seen in the images. The signal from the Ca cloud was removed by fitting a synthetic release cloud image to the measured release cloud.

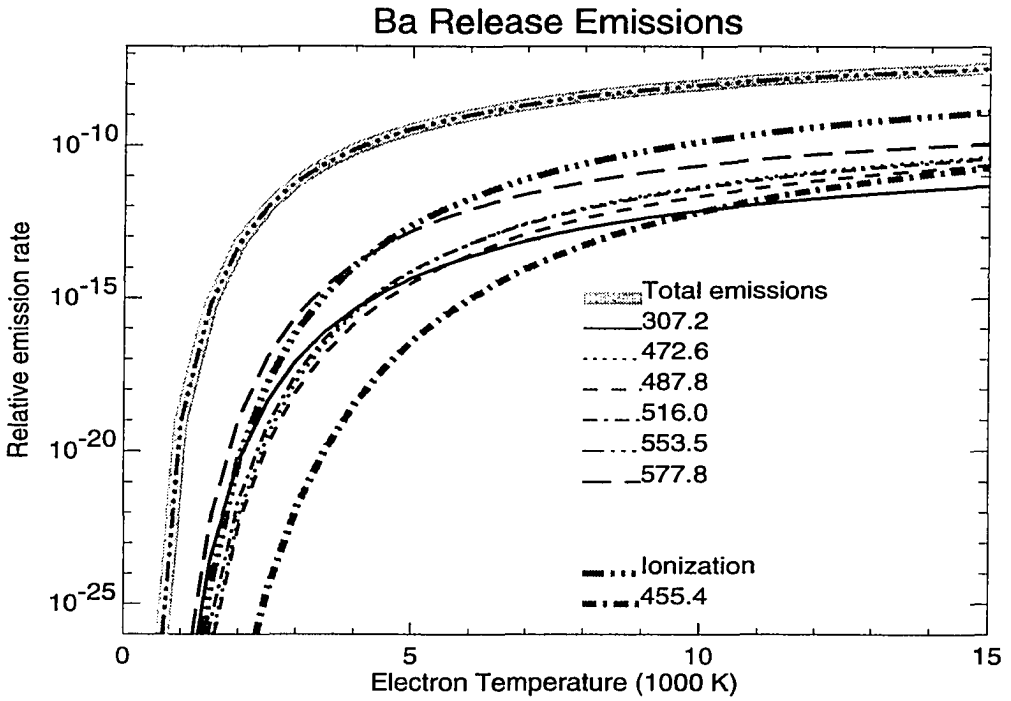

Figure 5.11: Relative emission rates for electron impact excitation of Ba. For a range of electron temperature the relative emission rates of several Ba neutral lines are plotted. The total of the emission rates is shown as the heavy gray line, and the ionization rate, and 455.4 nm emission rate are shown as medium gray lines. The 553.5 line is seen to dominate the emissions.

The 3-D density function has resisted attempts to find an analytic form of the profile in a 2-D projection. The synthetic projections are therefore created by integrating the density function introduced in Chapter 2 along parallel lines-of-sight. This was done such that the radius of the peak of the synthetic profile could be scaled to an arbitrary radius in the synthetic image.

The radius of the peak intensity of the expanding Ca cloud was found in the images for early times in the release, and was extrapolated for the entire time series using a least square fit to these early times. The upper right hand corner of the image was used to match the cloud intensities. For much of the time series this avoided any contamination from the Ba release. Five seconds after the Ca release, however, the Ba cloud was visible in this sub-image, and had to be blanked out. The blanking was applied to both the video data and the synthetic image for

consistency. The best fit intensity of the synthetic image was found by varying the intensity in the synthetic image and minimizing the difference between it and the background-subtracted video data. The total intensity of the Ca cloud was thus measured by applying the best-fit intensity to the synthetic cloud and summing over the entire synthetic image.

The results of the measurements are shown in Figure 5.12. The total release brightness from Figure 5.1 is plotted along with the Ca cloud intensity as measured by the method just described. The synthetic and video intensities show good correspondence as well. The uncertainty in the measurement is indicated by dashed lines above and below the best fit line. The uncertainty was calculated by comparing the peak signal in the synthetic image to the width of the noise in the background level of the video data. The uncertainty increases with time since the peak intensity is falling with time. In fact the surface brightness for a constant emission rate in the cloud should fall as $1/t^2$ since the column density is decreasing with this rate. The uncertainty is seen to be small early in the measurements, where the video signal is strong.

This estimated intensity can now be subtracted from the total measured intensity to find the signal solely from the Ba cloud. This is shown in Figure 5.13 and this signal is used to calculate the ratio. There is a slight ambiguity as to when the release starts in the IPD image. The image integration time was 5 seconds, but there was a video recording of the signal that was updated every second. In the video the burst is seen within the first second of the integration. Therefore, for the ratio measurement, the ratio is calculated not only for the total ICCD signal starting at the Ba burst to 5 seconds, but also for the total signal starting one second after the Ba burst. This actually makes little difference in the calculated ratio, but does increase the uncertainty because, in the second ratio, the measurement of the Ca cloud brightness is from later times when the signal to noise ratio has decreased.

The ratio that is calculated is between the emissions rates inferred from the signal in each camera. The emission rates can be calculated using the equation

$$\epsilon = \frac{4\pi r^2 C}{N\alpha T} \tag{5.12}$$

where r is the distance from the camera to the cloud, C is the total number of counts in the image, α is the factor from the intensity calibration (Appendix A), and T is the transmission of the filter for the IPD, or the relative response of the camera for the ICCD. The calibration for the IPD is of the actual image with the release cloud signal so the α is consistent, but the total signal from the ICCD

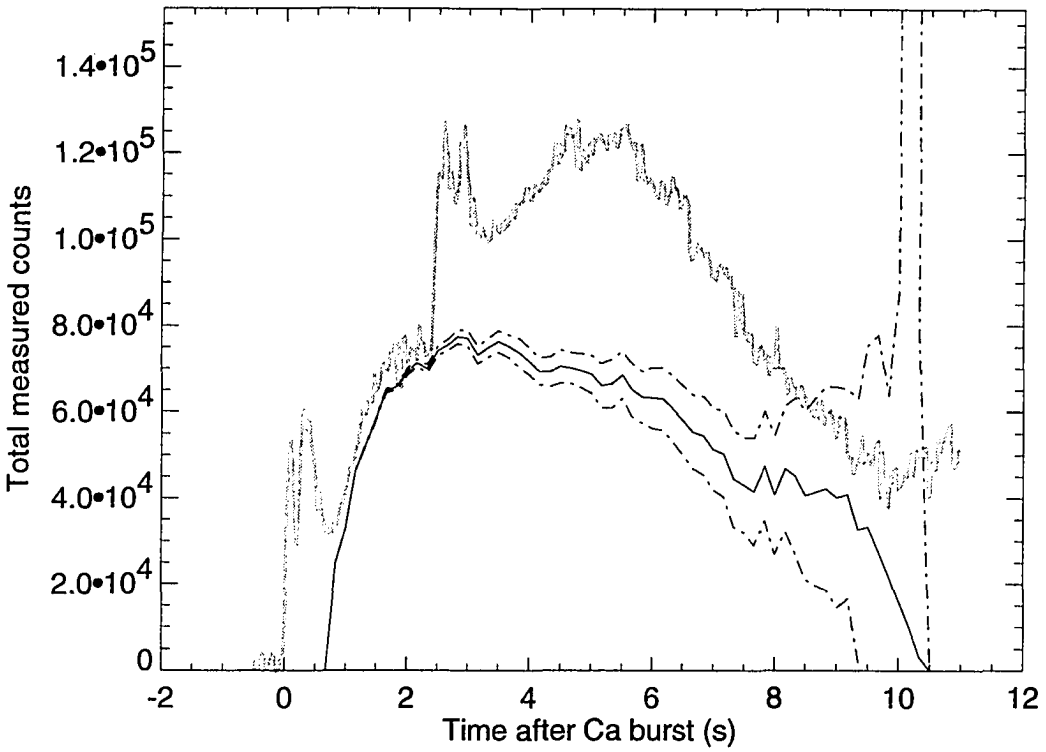

Figure 5.12: Measured ICCD signal from Ca release cloud. The total white light signal from both release clouds is shown as the heavy gray line. The white light signal measured from the Ca cloud alone, is shown as the solid line, with the uncertainty shown as dashed lines.

images is essentially the sum of 150 images. The calibration for the ICCD is from a single image, so α in Equation 5.12 must be multiplied by 150 in order to make the emission rate in units of s^{-1}.

For the ICCD interval between 2.5 and 7.5 seconds after the Ca burst, the ratio is 2.9 ± 1.2, and between 3.5 and 8.5 seconds the ratio is 3.2 ± 1.3. It is also instructive to look at the ratio when the Ca cloud emissions are not subtracted. In this case the ratio is 3.9 ± 1.6. All of these ratios are consistent with the assumption that all the emissions are from charge exchange, and are plotted in Figure 5.14.

For G-13 the data gaps do not allow for a good time series of the release cloud brightness, and therefore a measurement of the ratio of the ICCD signal to

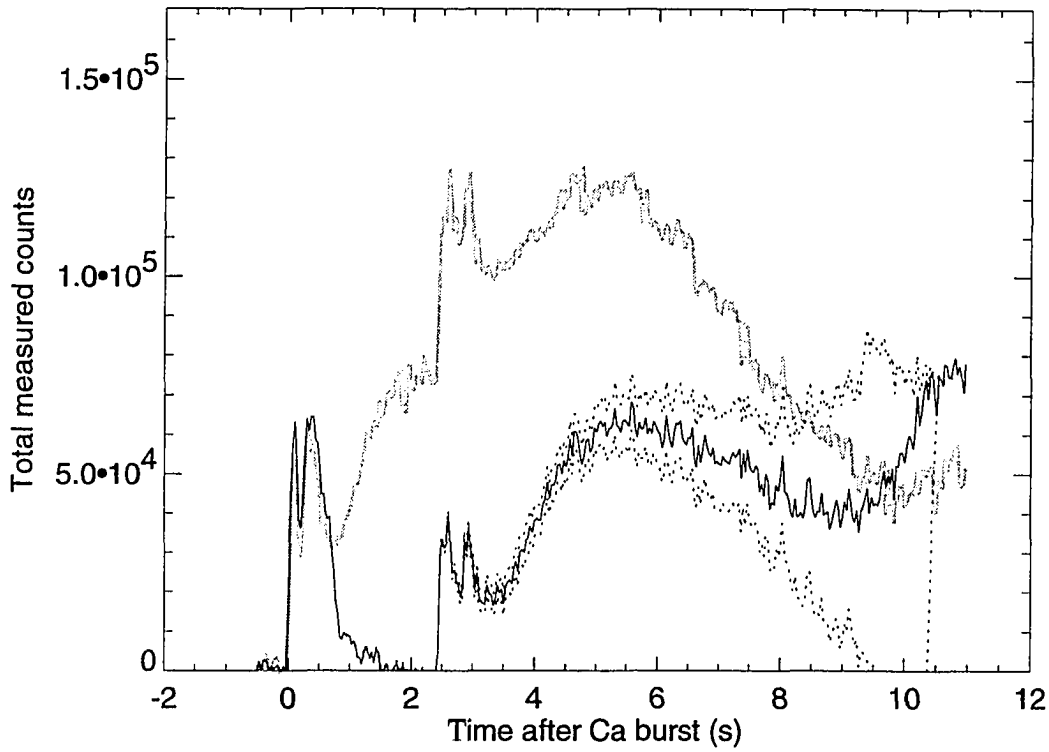

Figure 5.13: Measured ICCD signal from Ba release cloud. The difference between the total signal (heavy gray line) and the measured signal from the Ca release cloud (Figure 5.12) is shown as the solid line. The error associated with the measurement is shown as dashed lines.

the IPD signal is not as easy, especially in the early part of the release. The cameras on the Learjet did follow the release cloud after about 4 seconds, and there is a good set of data for both cameras between 10 and 15 seconds. In this case the Sr cloud signal cannot be removed using the same technique as described above for the Ca cloud. This is because the apparent separation between the two releases is much smaller than either cloud radius at 10 seconds, so only a small portion of the Sr cloud is visible uncorrupted by the Ba cloud. It is not a large enough portion to make a good fit to synthetic profiles.

Nevertheless, the Sr cloud can be given the expansive limits of either half of the signal to none of the signal in the ICCD images. Since there is no time series, 150 images of the ICCD video data are averaged and the total count in the

release cloud is measured. Again this corresponds to 5 seconds of data, which is the integration time of the IPD image. The ratios range from 12.7 for the limit that all the signal is from the Ba cloud (no Sr) to 6.4 for the limit that half of the signal is from the Ba cloud. The uncertainty in these ratios is about 40% as in the G-14 case. The signal to noise ratio was quite good for both cameras.

5.3 Absolute Intensities

The previous calculations show that for the Ba releases the ratios are consistent with the emission being from charge exchange. With this limited data set there is no independent way of telling if this is coincidental ratio due to another collisional process or not. If a second independent measurement, consistent with the emissions being from charge exchange, this will strengthen the argument that the primary collision process is charge exchange. This can be checked by comparing the absolute intensities of the release clouds to that calculated for charge exchange.

For Ba (or Sr or Ca), the volume emission rate for emission of wavelength λ due to charge exchange will be

$$\eta_\lambda = f_\lambda(n_{O^+}\sigma_{cx}\langle v\rangle n_{Ba}) \tag{5.13}$$

where n_{Ba} and n_{O^+} are the volume densities of species Ba and O^+ respectively, σ_{cx} is the charge exchange cross section, $\langle v\rangle$ is the average velocity between the release and the ambient background plasma, and f_λ is the fraction of collisions that result in the transition that produces the emission of wavelength λ. With no specific information on changes in the O^+ density, it shall be assumed to be a constant throughout the release region (not withstanding the loss of O^+ described in Section 5.2). With this assumption, the total photon emission rate can be calculated,

$$\epsilon_\lambda = f_\lambda \int_V n_{O^+}\sigma_{cx}\langle v\rangle n_{Ba} dV = f_\lambda\, n_{O^+}\sigma_{cx}\langle v\rangle N_{Ba}(t) \tag{5.14}$$

where $N_{Ba}(t)$ is the total number of Ba neutrals in the release as a function of time. The time dependence is an exponential decay with a time constant $n_{O^+}\sigma_{cx}\langle v\rangle$, which is rather long compared to the 11.5 seconds of data. As seen in the previous section the emission rate can be related to the counts in the image by

$$\epsilon = \frac{4\pi r^2 C}{\alpha T N_{Ba}} \tag{5.15}$$

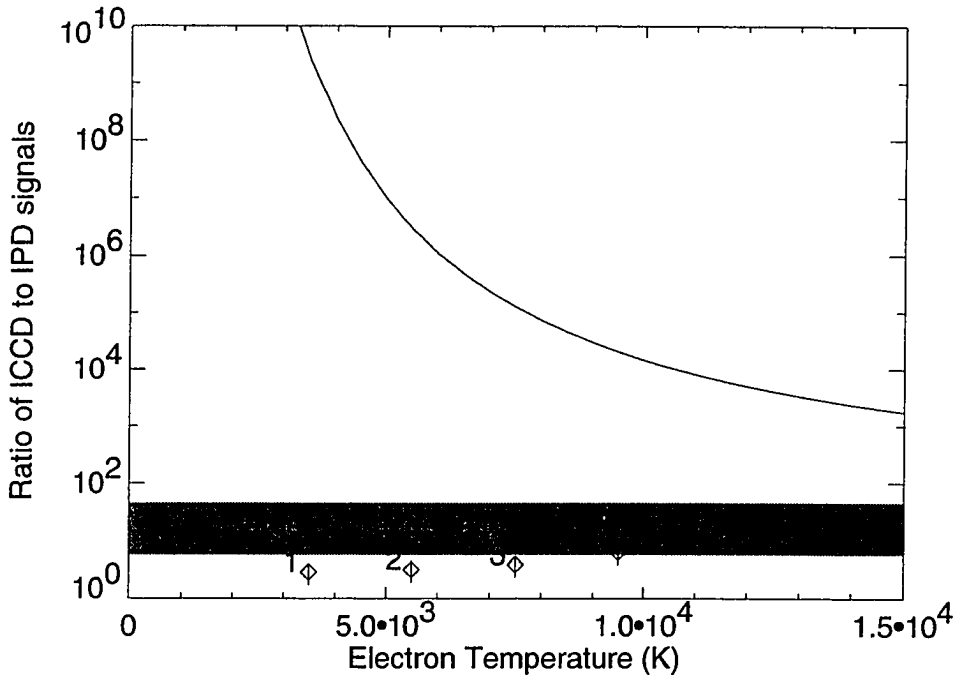

Figure 5.14: Emission ratios for charge exchange, electron impact, and measured ratios. The charge exchange ratio of 499 nm emission to the ion line at 455.4 nm is shown as the shaded area. The ratio of electron impact excitation of the 553.5 nm line to the electron impact ionization excitation of the 455.4 nm line is plotted for various electron temperatures. Five measured ratios are shown. 1) for G-14 from 2.5 to 7.5 seconds after the Ca burst; 2) for G-14 from 3.5 to 8.5 seconds after the Ca burst; 3) for G-14 not subtracting the Ca cloud; 4) G-13 assuming half the ICCD signal is from Sr; 5) G-13 assuming all of the signal is from Ba (no Sr).

Combining these and solving for the total counts,

$$C_\lambda = \frac{1}{4\pi r^2}\alpha T(\lambda) N_{Ba}^2 f_\lambda n_{O+}\sigma_{cx} \tag{5.16}$$

For the ICCD measurements the total measured signal is the sum over all the emission lines in the charge exchange cascade

$$C_{TOT} = \sum_\lambda C_\lambda \tag{5.17}$$

The free parameters in Equation 5.16 are the charge exchange cross section, and N_{Ba}. The number of atoms listed in Table 2.1 is from a single test firing of a Ba-Ti-B cannister from a rocket, for which it was found that 40% of the available barium metal in the cannister was vaporized. A single measurement gives no indication of the variation of the quantity measured so it is not known how much variation there is from cannister to cannister. Thus, for the absolute intensities the possibility of deviations from the listed total neutrals will have to be considered. Note that this variation does not affect the ratio calculations for the Ba release, as discussed in the previous section, since the total number of emitters cancels in the ratio.

The calculated intensity for the Ca release of G-14 is shown in Figure 5.15 for the nominal values of $\sigma_{cx} = 1 \times 10^{-14}$ cm^2, $N_{Ca} = 1.1 \times 10^{25}$. The calculated intensity is seen to fall far below the measured intensity for these nominal values. The cross section is not an adjustable parameter for Ca since the cross section has been measured. The total number of neutral Ca atoms can be increased by a factor of 2.5, but this still does not explain the discrepancy. The greatest unknown in the calculation of the total Ca cloud intensity is the ICCD camera response. The response is very low, between 0.05% and 0.2% of the peak value, at the K and H resonant lines of Ca^+. These are the brightest ion lines and are the only two in the (near) visible range (see Grotrian Diagram in Figure 5.7).

The calibration of the response function was made by imaging the output of a slit spectrograph looking at a standard calibration lamp. The wavelength scale for the digitized image was found by means of finding the position of the peak intensity for a set of narrow band interference filters placed in front of the spectrograph aperture. The coarseness of the image digitization results in a wavelength scale with steps of 1.8 nm and so the response of the camera is only known to within this accuracy. If the discrete response function used to calculate the intensity is shifted by one pixel, the change in the intensity is found to be nearly 40%. With this and

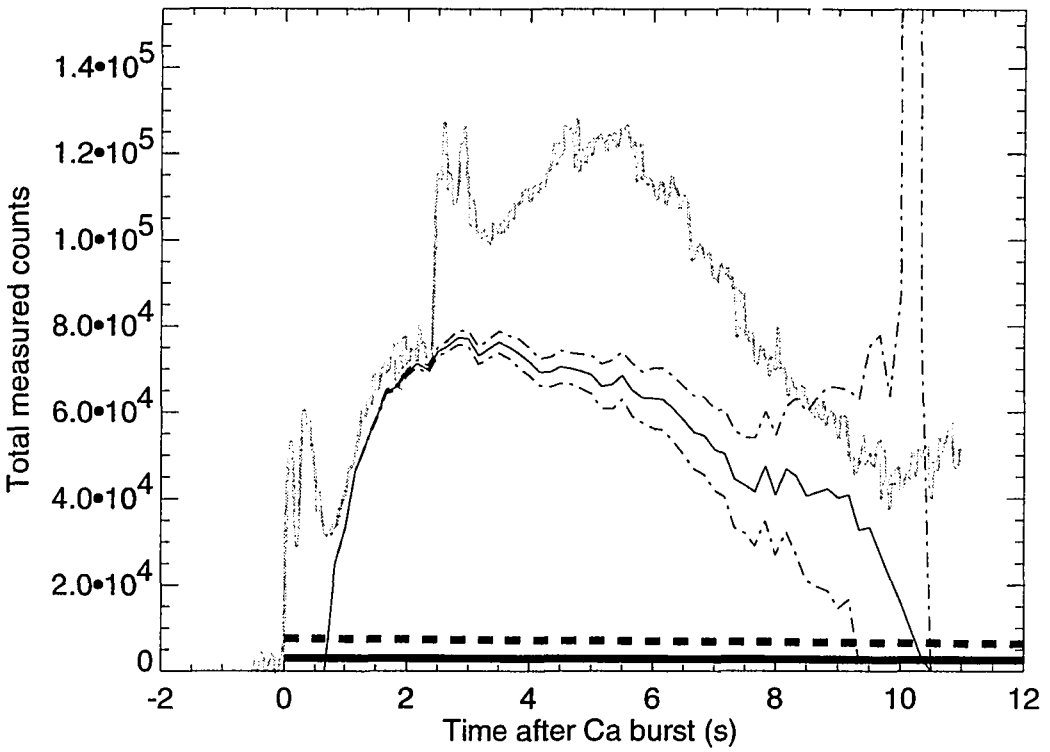

Figure 5.15: Measured and expected Ca emissions from charge exchange. The total signal from the G-14 release clouds are shown as the heavy gray line. The estimate of the Ca cloud is shown as the solid line, while the errors in the measurement are shown as dash-dot lines. The intensity calculated for the charge exchange emission rates are shown for 40% and 100% Ca neutral production as heavy solid and dashed lines respectively

other uncertainties the calculation of the absolute intensity of Ca has upwards of a 70% uncertainty. This does not affect the Ca ion inventory in Chapter 4 since in that case the star calibration was done for filtered images.

The absolute intensity calculation for the Ba release of G-14 is shown in Figure 5.16, for the nominal values of $\sigma_{cx} = 2 \times 10^{-16}$ cm^2, $N_{Ba} = 9.4 \times 10^{25}$. The calculation is made for three values of $A(7, 13)$ which was shown to play a key role in the various emission rates for the charge exchange cascade. Again the absolute intensity calculation for the nominal values is less than the measured intensity. In this case the charge exchange cross section is an adjustable parameter, but would require a factor of five increase in the cross section in order to match the measured intensity. This puts the cross section at $\sigma_{cx} = 1.25 \times 10^{-15}$ cm^2, which is greater than that predicted by the estimation method described in Chapter 3 (see Figure 3.5). The calculated intensity can be made to match the measured intensity, but only for values of the two parameters that approach their maxima (*e.g.* $N_{Ba} > 90\%$). This is especially true when considering that the ratios measured in the last section correspond to values of $A(7, 13)$ less than or near 0.1, which is the lowest curve in Figure 5.16.

For the Ca release cloud calculation there was an obvious systematic error that could explain the discrepancy between the two intensities. No such error is apparent in the Ba measurement. The standard errors due to the star calibration and noise in the image put the uncertainty in the measurement around 30%. But it still takes large values of either the charge exchange cross section or the number of neutrals in the release to match the calculated intensity to the measured intensity at 6 seconds after the Ca burst. This indicates that there are other emission processes going on, but this must be reconciled with the ratios from the previous section that are consistent with all of the emissions being from charge exchange.

5.3.1 Electron Impact Emissions

Since the purpose of the releases was to produce a CIV discharge, it is instructive to look at the electron distribution that could produce the intensity measured in the release clouds. *Newell and Torbert* [1985] and *McNiel et al.* [1990] both point out that the excitation cross section for the Ba neutral resonant line at 553.5 nm is very large, and acts as an energy sink during a release. This large cross section implies that it will be a significant emission during a CIV discharge.

A simple model of the electron distribution is used to find the electron density

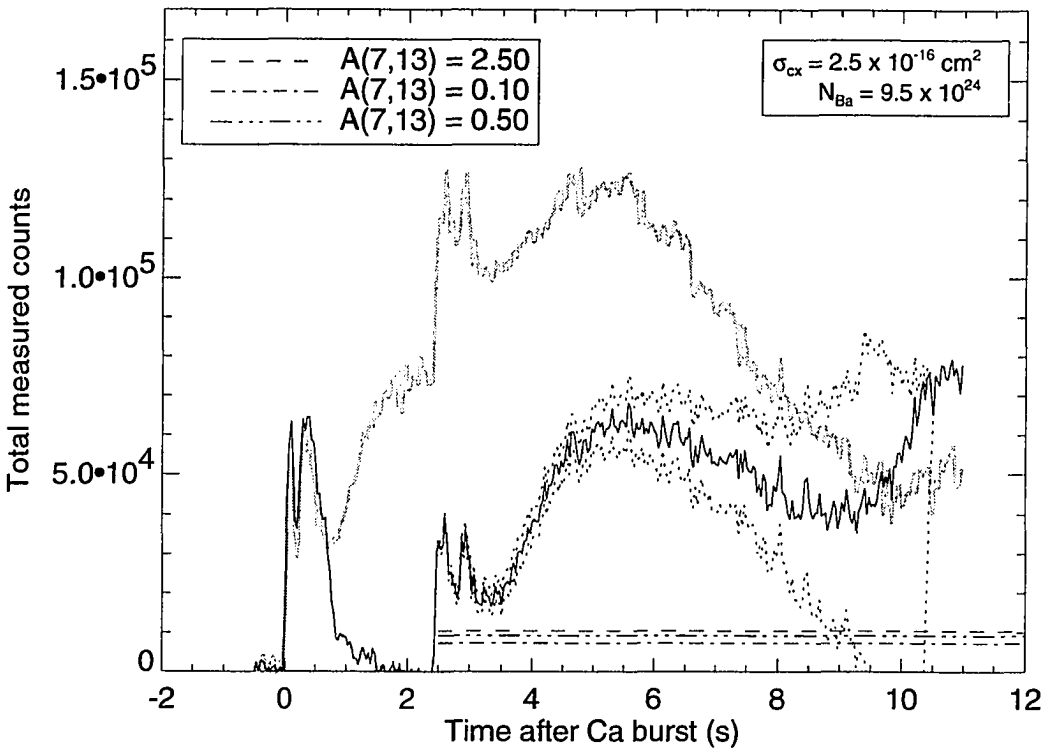

Figure 5.16: Measured and expected signal from charge exchange for Ba. The calculated signal for charge exchange using the nominal release parameters, and for three values of the transition probability $A(7,13)$ are shown as indicated.

needed to produce the emissions measured in the G-14 Ba release cloud. With the detailed cross section for excitation and ionization (see Chapter 3) it is not difficult to calculate the emission rate for Ba atoms for an arbitrary electron distribution. *Torbert et al.* [1992] measured the electron distribution for the CRIT II rocket release and found not only a population of heated electrons, but also two energized tails at 10's of eV. This forms the basis of the electron distribution used for the current model. A heated population of with a tail of 30 eV central energy is used. The overall distribution is the product of the velocity distribution and the number density,

$$f(\mathrm{v}, \mathrm{r}, t) = n_e F(v) \tag{5.18}$$

where n_e is assumed to be a constant, and $F(v)$ gives the 'two-humped' structure,

$$F(v) = \exp\left[-(v/v_{th})^2\right] + \gamma \exp\left[-\frac{(v - v_0)^2}{v_{th}^2}\right] \tag{5.19}$$

The relative density of the tail was set as a parameter, γ,the fraction of the peak of the heated electrons. The velocity is normalized numerically to unity ($e.g. \int F(v)dv = 1$) so that $\int f(v)dv = n_e$. The electron distribution is uniform and isotropic within the Ba cloud, which for lack of more detailed information will act as a zeroth order approximation.

The emission rate per Ba atom per second is found by

$$\epsilon = n_e \int F(v)\sigma(v)vdv \tag{5.20}$$

Two parameters can be adjusted for this model, the electron density, n_e and the relative intensity of the tail electrons, γ. The contours of emission rate for n_e ranging from 0 to 10^4, and γ ranging from 0 to 1, are shown in Figure 5.17. The emission rates calculated for the G-14 Ba cloud from the ICCD images, assuming that the emission were from the Ba 553.5 nm line, are between 0.001 and 0.003 photons per atom per second. For $\gamma > 0.1$ the electron density needed to produce emissions rates in this range are seen to be from 1500 to 5000 cm^{-3}. For $\gamma < 0.1$, when the electron distribution is almost purely heated, the electron densities need to be $\sim 10^4$ or higher to produce emission rates comparable to the ones observed. Note that the ambient densities are $\sim 10^6$, so that energizing 1 in 1000 electrons for large γ or 1 in 100 electrons for small γ would be sufficient to create the observed emissions.

This would imply that CIV of relatively low efficiency could be producing the emissions. As noted before, the collisional processes with heavy particles should be

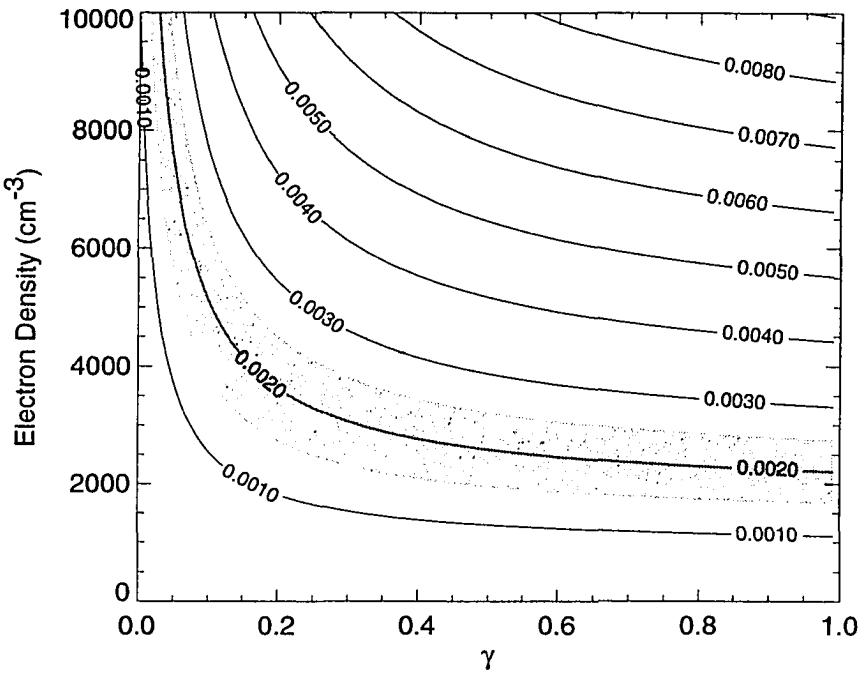

Figure 5.17: Contours of Ba emission rate for electron distribution model. The emission rates for the Ba 553.5 nm resonant emission line are contoured for different values of γ and n_e.

nearly constant. The intensity measured in the ICCD shows a significant change in a matter of a few seconds. An electron distribution could easily respond on this time scale. However, the ratio calculation would indicate that the emissions cannot be primarily from electron impact collisions. The minimum ratio for electron impact is 45, and if 90% of the emissions are from a process that produces a ratio of 45, then the overall ratio should be close to 45. This is not seen.

5.4 Neutral Disks

Just after the Sr burst on G-13, there is an expanding cloud, different than the release cloud, which is seen in all four primary cameras including the filtered IPDs. The cloud seen through the Ba ion filter at 455.4 nm would seemingly indicate that

there are Ba ions present, but this cloud can be seen in the unfiltered ICCD before the Ba cannister has detonated. There is a neutral strontium resonant line at 460.7 nm which is near the band edge of the barium filters that were used (see Chapter 2). The transmission through the filter at 460.7 nm is less than 10% at the optical axis and will be lower toward the edges. The development of the cloud is seen in the three images in Figure 5.18 from the KC-135 filtered IPD.

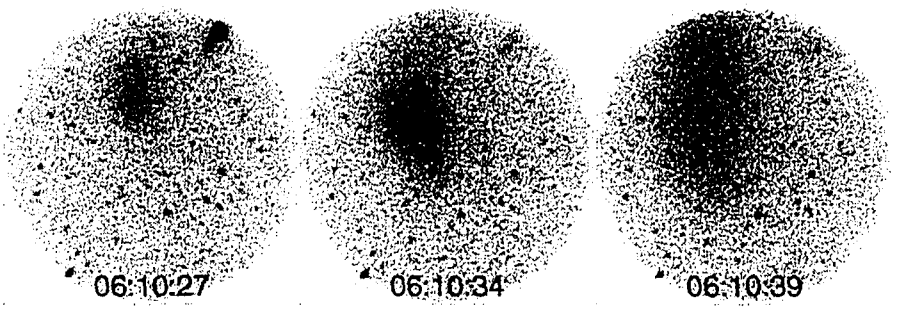

Figure 5.18: Sr neutral disk seen from KC-135 IPD. A sequence of three (negative) images is shown with the Ba burst seen to the upper right in the first image (the Sr burst was not recorded). The Sr disk is seen expanding to the left starting about halfway across each image.

From observations of other CRRES releases in the Caribbean in the summer of 1991, *Delamere et al.* [1996] have found evidence of disks of neutral barium expanding from near the release point. The outer radius of the disk expands with a velocity very near the satellite velocity. The explanation given is that these neutrals are the product of Ba - Ba^+ charge exchange collisions. Ions are created by photoionization and begin gyrating in the magnetic field. These will come into contact with the neutral cloud as it streams by. The charge exchange collision is resonant and so will have a large cross section as seen in the Rapp and Francis calculation in Chapter 3, and as reported by *Sramek* [1980]. The observation of the Sr neutrals in the IPD and ICCD images may be evidence of a similar neutral disk.

To verify that the geometry is correct, the expected location of the cloud had to be mapped on to the images. First, the plane perpendicular to the magnetic field was found. Then a set of concentric rings, with radii at one second time intervals for the release velocity were calculated in this plane. These were mapped from geocentric coordinates to the image pixel positions and are marked on the image in Figure 5.19. The rings are skewed in the image, but are seen to match well the edge of the cloud at the top of the image. The image is from 6 seconds after the

Sr burst, and is seen to be just inside the fifth ring. This indicates that either the velocity is 5/6 of the release velocity or that the disk did not form until one second after the burst.

To estimate the number of Sr neutrals that these intensities would represent the emission rate of the 460.7 nm line of Sr must be known. The full calculation of the emission rate should include an entire hierarchy of states, but is restricted to the 460.7 nm resonant line for simplicity. The uncertainty in intensity of the neutral cloud in the images is much larger than any error due to this simplification. The source of the resonance is solar radiation. For a solar flux of $P_i(v)$ as a function of the neutral velocity in W m^{-2} nm^{-1}, the emission rate per atom is

$$k_{ij} = 4.45 \times 10^{-11} P_i(v) f_i^{\gamma} \lambda^3 \frac{A_j^{\gamma}}{\sum A^{\gamma}} \tag{5.21}$$

Stenbaek-Nielsen [1989], where f_i is the oscillator strength and $A_j/\sum A$ is the branching ratio for the emission and λ is the wavelength of the emission in Ångstroms. The transition for 460.7 nm is from the $^1P_1$ state to the ground state, $^1S_0$. There is only one other allowed transition from the upper state but with a wavelength of about 2 μm. The branching ratio is assumed to be 1. There is a strong Fraunhoffer dip in the solar spectrum near 460.7 nm. For Sr at rest the solar flux will be near 1.1W m^{-2} nm^{-1}, but quickly rises to greater than 2.0. The oscillator strength of the line is 2.0 [*Moore*, 1958]. This results in an emission rate of 10 to 20 photons per second. Using an intermediate value of 15 and a star calibration of camera sensitivity, the cloud inventory is found to be 1.1×10^{22} Sr atoms in sunlight in the field of view of the IPD, for a filter transmission of 0.1. A calculation for the ICCD results similar numbers. It is estimated that the portion of the cloud that is seen represents only a third to a quarter of the entire disk. This means that the number of neutrals in the entire disk may be as large as 4×10^{22}. There were an expected 1.04×10^{24} neutrals in the release cloud so that the disk represents nearly 4% of the available neutrals. This is very close to the results reported by *Delamere et al.* [1996] for Ba releases in sunlight.

A Rapp and Francis charge exchange cross section calculation is shown in Figure 3.6 for resonant collisions of Sr. Similar to Ca, the cross section is on the order of 1×10^{-14} cm^2. Each of the neutrals included in the inventory above was originally an ion below the terminator, which indicates that the ion yield of the release was greater than measured by the ion inventory alone. Further, the number of neutrals in the disk is only a fraction of total number of ions that were created in the release. The calculation of the efficiency is highly density dependent, and

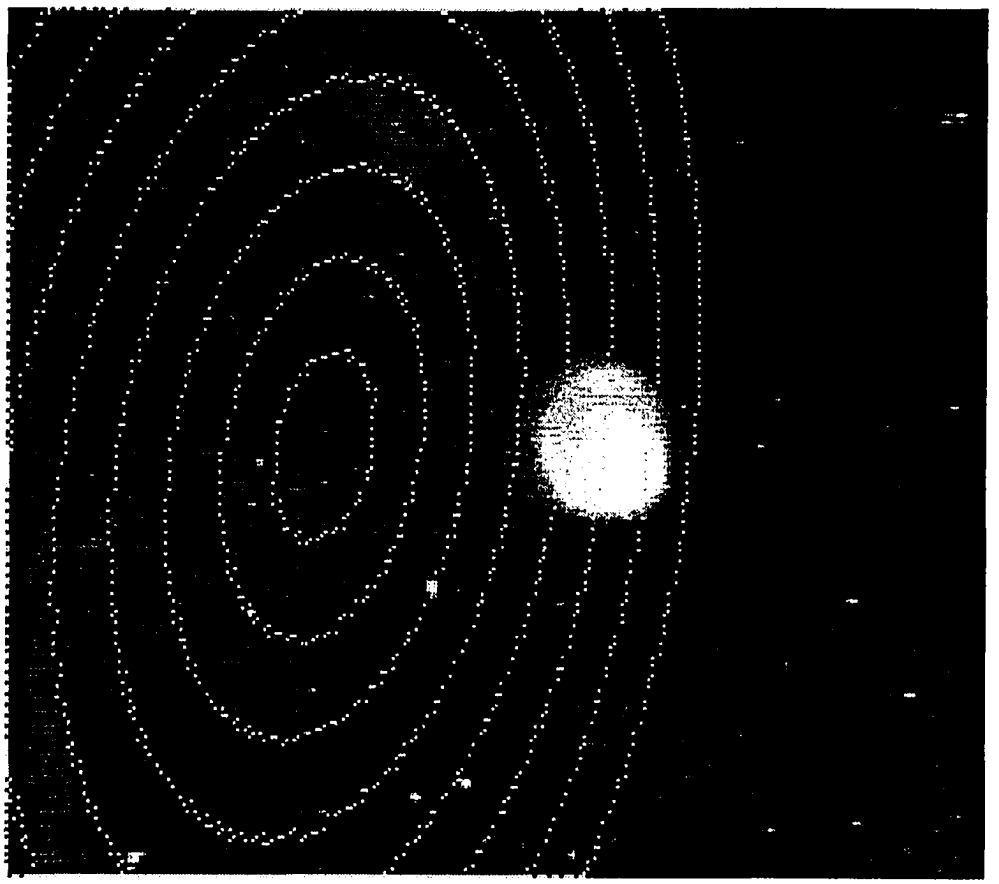

Figure 5.19: Neutral disk map. Points in a plane perpendicular to the magnetic field are mapped onto the image of the release. The rings are points at consecutive radii $v_{sat}t$ for each second up to 8 seconds. The center of the rings is at 1 second along the satellite track. The image is taken at 6 seconds after the release, and the neutral disk is seen just up to the 5 second ring.

occurs at times when the densities are changing rapidly. The calculation would also depend on a detailed ionization rate, which is not available. It still remains, however, that the number calculated above is a lower limit on the ionization in the cloud.

There was a neutral disk observed for the G-14 release as well. It was very low intensity and appeared nearly 10 seconds after the Ca burst. It was also near the edge of images of both ICCD cameras, and was seen in both IPDs. There are no similar neutral Ca lines near the bandpass of the Ba^+ filter on the IPDs, and based on this and the long delay after the Ca burst, this neutral disk is assumed to be of Ba. The signal in the ICCD should be primarily from the 553.5 nm emission line, while the signal seen in the IPDs is from Ba photoionized in sunlight. The low signal in both cameras indicates that the density of this cloud is low. The emission rates for the 553.5 nm line should be similar to that calculated for Sr ($\sim$ 15 per atom per second, *Stenbaek-Nielsen* [1989]), and this emission is close to the peak in the sensitivity of the ICCD. Thus a moderate density of Ba should produce larger signals than are seen.

The appearance of the Sr neutral disk and the large difference in the number of ions that it implies compared to the ion inventory raises many questions. The first is about the assumed mechanism of the disk formation – might the disk not come from a mechanical failure of the release cannister, thus spewing neutral Sr out at velocities close the satellite velocity? The answer to this is that the release cloud is seen to be well formed and of similar intensity to the other three release clouds.

More importantly as it pertains to CIV, why are the ions not seen in the inventory? Charge exchange collisions should result in little or no momentum change during the collision. After the Sr –Sr^+ charge exchange collision, the newly formed ions will have the pitch angle of the neutral particle before the collisions, but now gyrating in the magnetic field. The new ions will be from neutrals that were in the slower part of the release, and their velocity relative to the magnetic field will be lower. The expansion velocity of the Sr release is 1.62 km/s, and the release velocity is 9.4 km/s, so that the minimum velocity (at the peak density) is 7.8 km/s. Projected along the release field line, the velocity along the field line will be about 1.4 km/s. This compares to 0.5 km/s for the speed of the terminator moving along the release fieldline for G-13, as calculated in Chapter 4.

The greatest mystery is discerning where the ions came from in the first place. The disk appears at about 1 second after the release, which means that 4%

of the neutrals had ionized, and charge exchanged by this time. The collisions cross sections for Sr with ambient species are not expected to be significantly greater than for Ba and Ca, and in fact the charge exchange cross section is expected to be much smaller, based on the calculation in Chapter 3. A four percent production rate in one second implies a time constant of 24.5 seconds. Using the simplified $\tau = n_O \sigma(\langle v \rangle)\langle v \rangle$ with n_O being the density of either neutral or ionized oxygen then the cross sections for collisions of Sr with either can be calculated for a time constant of 24.5 seconds. The cross section for collisions with neutral oxygen would be 5.3×10^{-13} cm^2 and the cross section for collisions with O^+ would be 7.4×10^{-12} cm^2. These are clearly unrealistic, and point out that the ionizing mechanism within the first second could well be electron impact ionization due to a population of heated electrons – CIV.

Chapter 6

Discussion and Conclusions

When the experimental plans were defined for the CRRES CIV releases it was assumed that the amount of ionization created would far exceed any other ionization process except possibly photoionization. This expectation was based largely on the results of the Porcupine barium shaped charge release [*Haerendel*, 1982]. The detailed process involved in CIV was not known and the use of elements with different atomic masses, Ca, Sr and Ba, would allow for an investigation of the mass dependence of the CIV process.

As detailed in this thesis, it is now clear that CIV, if present, cannot be expected to provide much ionization and a number of other competing processes have been proposed [*Newell and Torbert*, 1985; *Lai et al.*, 1992b, 1992a; *Swenson et al.*, 1991]. Most of this work has only appeared in print after our CRRES CIV releases. Hence, the CRRES observations were made still expecting significant ionization from CIV. Nevertheless, a good data set was obtained and allows for a critical evaluation of the various ionizing processes.

The set of optical observations and measurements of four below-the-terminator releases from the CRRES satellite has been presented in the previous chapters. There were two major goals of the study; 1) to examine the releases for evidence of CIV, and 2) to examine the collisional processes in chemical releases, and, to the extent possible, measure the cross sections.

Many of the collisions that occur will be accompanied by optical emissions, many with unique signatures. With a comprehensive set of spectral measurements of the release cloud as the collisions are happening, a determination of the efficiency of CIV and each collisional process would be possible. Even with non-optimized instrumentation, the bright CRRES CIV release clouds, seen below the terminator,

allow for a limited set of measurements.

6.1 Cross Sections

Most of the data for collisional cross sections came from literature reviews or modeling. The electron impact excitation and ionization cross sections are well known and have been used in several models before [*Machida and Goertz*, 1988, 1986; *Moghaddham-Taaheri and Goertz*, 1993]. The charge exchange cross section is calculated using the *Rapp and Francis* [1962] two-state method, both here and by *Liou and Torbert* [1995]. The cross section for Ba is less than that predicted by *Swenson et al.* [1991], but is greater than previously thought, and is important for observations. The calculated range is 8×10^{-17} cm^2 to 6×10^{-16} cm^2, which compares quite well to the ionization rate in the plateau of the G-14 Ba^+ cloud. This also agrees with the upper limit of *Stenbaek-Nielsen et al.* [1993] from spectroscopic studies of sunlit releases.

The only evidence for associative ionization that should appear in the observations is a sharp boundary in the ion cloud at the H Lyman-α emissions line terminator, well separated from the visible terminator. This is not seen in the CRRES data, which agrees with the fact that while the associative ionization collision rate may be high (of the same order of magnitude as charge exchange), the dissociation rate of BaO^+ may be very slow, as low as 10^{-3} s^{-1}. Thus associative ionization can result in a loss of neutral Ba in releases, but there should be little contamination of the ion inventory.

Other cross sections which are not available in the literature are neutral-neutral impact excitation and ionization (stripping). The metals are certainly undergoing these collisions, and the emissions may represent a significant portion of the light observed. But, until absolute cross sections are determined (either measured or calculated) the contribution from these processes will have to remain speculative.

From this preliminary examination of the collisions for below-the-terminator releases, the collisions that are important for each species can be addressed. For Ba it is found that the dominant ionizing collision, in the absence of intense fluxes of energetic electrons, will be charge exchange. This comes not only from an examination of the relative cross sections, but from the new measurements of the release clouds below the terminator. Associative ionization may be a large ionizing process,

comparable in rate to charge exchange, but the product, BaO^+ will not be observed with current standard instrumentation for these releases. The dissociation rate of BaO^+ is not expected to be large enough to produce a significant contamination of Ba^+ in the ion clouds.

For Ca the dominant collisional ionizing process will certainly be charge exchange. With a cross section of 1×10^{-14} cm^2, measured by *Rutherford et al.* [1974], charge exchange collisions should out compete associative ionization even for ratios of O to O^+ densities of 10^3.

The lack of near resonant charge exchange reaction channels for Sr in its ground state means that charge exchange will not dominate in producing ions. Stripping should be comparable to charge exchange in producing Sr^+ and again associative ionization may be producing orders of magnitude more SrO^+.

6.2 CRRES Results - Ion Inventories

Ionization was seen in all four of the CRRES CIV releases, with G-14 apparently producing more overall ionization. From the optical ion inventories we found 8.4×10^{21} ions for the G-13 Sr release and 1.4×10^{22} ions for the G-13 Ba release. Assuming 40% neutral vaporization from the canisters, these correspond to 0.02% and 0.15% ionization yield, respectively. Similar analysis for the G-14 releases give 3.1×10^{22} for the Ca release and 1.8×10^{23} ions for the Ba release, corresponding to 0.27% and 1.48% ionization yield. respectively, again using 40% neutral vaporization.

Time histories along the satellite tracks of the Ba ion clouds show an initial enhancement in ionization followed by a decay to a plateau of constant ionization, consistent with the later ionization being from collisional ionization with an ambient species of uniform density. The ionization rate for the plateau of the G-14 Ba release is 3.5×10^{21} s^{-1}. Under the assumption that all the ionization is due to charge exchange this would indicate a charge exchange cross section of 5×10^{-16} cm^2, consistent with the theoretical two-state calculation.

From an examination of the total intensity of the Ba ion clouds, it was found that the G-13 cloud intensity decayed fairly rapidly, with a time constant of 350 seconds. This is probably due to the small dip angle of the release field line, and a slowing of the Ba ions - similar to what was seen in the G-14 Ba release. This in combination with the delay after the burst before the ion cloud was observed

indicates a greater total ion inventory than was measured. This would explain why the inferred ionization rate from the G-13 Ba^+ cloud is less than would be expected for charge exchange collisions. The observation of a Sr neutral disk that forms about 1 second after the Sr burst also indicates a greater amount of ionization than would be measured in an ion inventory. An estimate of the number of neutrals in the disk is 4% of the total number of neutrals released. Each of these neutrals had to be an ion within the release if the charge exchange mechanism proposed by *Delamere et al.* [1996] is correct. Therefore there was at least 4% ionization within the first second of the Sr release. These ions are not seen in the inventory, and where they are remains a mystery.

What also remains a mystery is that, for the Ca release, the ionization rate is less than would be predicted for charge exchange. The measured ionization rate from the ion cloud inventory, is at least a factor of 50 less than the rate predicted for the charge exchange cross section measured by *Rutherford et al.* [1974]. This would imply a charge exchange cross section more on the order of 1×10^{-16} cm^2. Probably the most obvious unknown in the experiment that could explain this discrepancy is the number of neutrals produced in the release. Without independent verification of the neutral production, and until further spectroscopic studies of Ca releases can be made, the discrepancy in Ca^+ production must remain a mystery.

6.3 CRRES Results - Release Clouds and CIV

Most of the conclusions to be drawn about whether CIV was initiated in the releases comes from the examinations of the release clouds seen with low light level TV cameras below the terminator. The greatest information was available for the Ba releases. CIV should be observed as the electron impact excitation and ionization of Ba. The two primary measurements were 1) the ratio of the ICCD white light signal to the filtered IPD signal, and 2) the absolute intensity of the ICCD signal. The ratios and absolute intensities can also be predicted for charge exchange and electron impact and ionization. The two measurements together show conflicting results. The ratio is consistent with the emissions being primarily from charge exchange. The absolute intensity, however, is much greater than expected for charge exchange, even with a broad range of values for the cross section and total number of atoms available. A simple calculation of the electron flux needed to create the signal measured in the ICCD shows that electron impact could easily fill the gap. But, this is in direct contradiction to the ratio measurement, which in essence shows

that much more 455.4 nm emissions is being produced than would be expected for electron impact.

There is no evidence that the extra ICCD signal has to be due to electron impact emissions, but the very small fraction of the ambient electron population (1 part in 10^3) needed to produce the signal is very appealing. Even very inefficient CIV could produce electron fluxes on this order (*e.g.*see *Biasca et al.* [1993]). However, unless the ratio calculation is fundamentally flawed, even this small enhanced electron population production is not happening. This means that according to the ratio measurement there is no CIV discharge in the Ba release of G-13 or G-14.

With no ratio measurement for the other two release, less can be said about the presence of CIV. The absolute intensity measurement of the Ca release shows that there is much more light than can be explained by charge exchange, again indicating that electron impact excitation and ionization, and therefore CIV, may be occurring. But, much less ionization than would be predicted for charge exchange is seen. The ion inventory for the Sr release is very low, but the appearance of the neutral disk early in the release would argue for a much greater amount of ionization at very early times in the release, similar to what would be expected for CIV.

6.4 Other emissions

The contradiction between the ratio calculation and the absolute intensity from the ICCD can be resolved if there is another collisional process producing a significant amount of emissions. The two collisional processes with unknown cross sections, listed in a previous section, are neutral-neutral impact excitation and ionization (stripping) and associative collisions. For an oxygen density of 2×10^7 cm^{-3}, and the release velocity of $\sim$ 10 km/s, a cross section of 1×10^{-16} cm^2 is needed to produce the emission rate of 0.002 for the 553.5 nm emission line. While the only data found for heavy-heavy particle excitation reactions showed much lower cross sections, the electron impact excitation cross section is much larger for the Ba resonant line than for other comparable lines. However, the 455.4 nm emission due to neutral neutral collisions with O would only be energetically possible for 20% of the Ba atoms in the release. So again the ratio measurement would probably eliminate this possible mechanism.

Another process discussed in relation to Ba is associative reaction of the

type

$$Ba + O \rightarrow BaO + h\nu \tag{6.1}$$

sometimes called chemiluminescence. There have been many studies of Ba with O_2 and N_2O [*Reuther and Palmer*, 1982], but none (to my knowledge) with O. The spectrum of the reactions with O_2 and N_2O are broadband in nature. The data recorded by *Reuther and Palmer* [1982] show a peak at around 480 nm, and the intensity has fallen to detectability limits by 550 nm, and 400 nm. This could well produce low values of the ratio measurement if the spectrum of the reaction like 6.1 were similar to those measured by *Reuther and Palmer* [1982]. However, if a similar reaction is taking place in Ca, with a similar broadband spectrum, then there should be signal in the IPD with the Ba^+ filter. From Figure 2.15 it is seen that this is not the case after the first few seconds.

Finally, there has been no discussion of the emissions from Ti, B, their ions and combinations (*c.g.* TiB_2), a result of the burning of the propellant in the release cannister. Boron is not expected to contribute since lines of its neutral and ion are either ultraviolet or infrared. However, Ti and Ti^+ do have many emission lines in the visible, but there is very little information about cross sections for this species. *Szuszczewicz et al.* [1996] have found evidence for Ti ions at very early times in a Ba-Li thermite release over Puerto Rico. The missing intensity in the ICCD could come from collision process involving Ti, and still not show any emissions in the IPD, and thus the Ca release would not be seen (after its initial burst) as in Figure 2.15. But, if the majority of the measured intensity in the ICCD is from collisions involving Ti or Ti^+, this would further lower the ratio for the Ba emissions in the ICCD to the Ba^+ emissions in the IPD, which again argues against CIV in the barium releases.

6.5 Previous and future releases

One may well ask why the release clouds, emitting below the terminator, have not been observed in the past. Probably the main reason has to do with the number of neutrals released and the ability to observe the emissions. For CRIT II the total number of available neutrals in the super critical jet was 6×10^{23}, while the CRRES Ba releases had $\sim 10^{25}$. For video data, while we digitize at 8-bits, the true dynamic range is probably not much better than 50. Thus the factor of 15 in number of neutrals, for all other parameters being the same, the shaped charge releases would be only marginally observable. Reviewing the video tapes from CRIT I and II,

there is some signal from the ICCD for that release as well as from the IPDs, but in both cases the signal is very low. A careful study of these data would be quite useful and could help clarify some of the puzzling results from this study (as well as double the data set for collisions in CIV releases).

An undeniable result of this study is an understanding of what should be done to make a more definitive measurement of the collisional processes in a below-the-terminator chemical release. Therefore in the event that a similar experiment is attempted, there are a few key measurements to be made. For Ba, a camera, or photometer should again be dedicated to the 455.4 nm Ba^+ line. The two green lines, 553.5 for electron/neutral impact excitation, and 499.0 for charge exchange, should also be monitored, but care must be taken to separate the 499.0 lines from the 493.4 nm ion line. In future releases it will be important to have a way to monitor emissions from the release propellant, such as copper or titanium.

Appendix A

Star calibration

Figure A.1 shows the steps that light from a star will take as it enters a detector and is converted into an image. The figure is specifically for a filtered camera, but can be applied to white light cameras as will be discussed later. The light from the star is spread over a wide range of wavelengths. To estimate the amount of light that enters the detector it is important to know two things; the transmission function of the filter and the flux from the star.

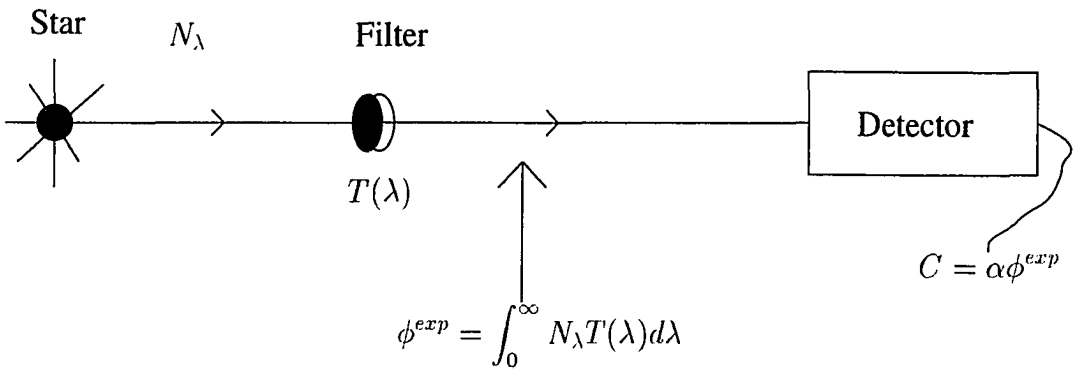

Figure A.1: Star Calibration. The steps included in a star calibration are shown.

The transmission function of the filter is measured in the lab. The filters used for CRRES had bandpasses of 3 nm for Ba, 3 nm for Sr and 7 nm for Ca (in order to get the K and H resonance lines). The peak transmission was about 50% for all the filters.

To make triangulation measurements of the ion clouds it was necessary to use the stars in the image for determining the look angles for that image. The positions of the stars were found in the *Smithsonian Astrophysical Observatory* [1969] catalog

. This catalog also lists the apparent magnitudes and spectral types of the stars in the image. These were used to calculate the flux from the star. The spectra were taken from a library of spectra from 161 stars [*Jacoby et al.*, 1984]. The stars as they are listed in the library had been dereddened to account for scattering by interstellar dust [*Schild*, 1977]. This correction was removed to reflect the actual spectrum that would be measured at the top of the atmosphere.

The quantity reported in the library of stellar spectra is energy flux, F_λ, which has units of ergs per square centimeter per second per Ångstrom (ergs cm^{-2} s^{-1} $Å^{-1}$). It is a simple calculation to convert this into photon flux, N_λ, with units of photons per square centimeter per second per Ångstron (photons cm^{-2} s^{-1} $Å^{-1}$). There is no spectral information in the images, and a number flux with no wavelength dependence is desired. To get this quantity, the star's photon flux, N_λ, and the filter transmission function, $T(\lambda)$, are integrated over all wavelengths,

$$\phi^{exp} = \int_{\lambda=0}^{\infty} N_\lambda T(\lambda)\, d\lambda \qquad (A.1)$$

The expected flux, ϕ^{exp}, has units of (photons cm^{-2} s^{-1}).

Light from a star is recorded by a TV camera as a signal to an analog recording device and by a digital camera as a number of counts in a pixel. The TV image is converted to a digital image by means of any number of digitizing devices. Since the star is for all practical purposes a point source of light, an ideal camera would image each star into a single pixel and the number of counts measured could be obtained by sampling that pixel. In practice this is not the case, and this failure is primarily a function of aberrations in the lens, and spreading in image intensifiers. Therefore finding the number of counts for an individual star in an image requires choosing a small portion of that image that includes the star (and only that star). The image will include a background which can be determined by various means (see section 2.2.2). When the background is subtracted, the count from the star is the number of counts in that portion of the image.

The relationship between the expected flux and the measured counts should be linear. The quantity α is the slope of the least squares fit to counts vs. expected flux. It should be noted that the fit should force the intercept to be at zero, since no counts should result from no incident flux. If C_i is the array of the number of counts per star and ϕ_i^{exp} is the array of the expected flux from each star, then α can be found by,

$$\alpha = \frac{\sum_i C_i \phi_i^{exp}}{\sum_i (\phi_i^{exp})^2} \qquad (A.2)$$

The units of α are cm^2 sec. The quantity α is not easy to interpret physically. In essence it is the quantum efficiency multiplied by the effective aperture of the system and the integration time. The interpretation is unnecessary since it will be applied to the same image where these two parameters are unchanged. It is enough to say that α converts a photon flux at the front of the camera into a measured count in an image.

A.1 Ion Inventory

Figure A.2 shows the application of the star calibration quantity, α, to calculating an ion inventory. An ion cloud in sunlight will be emitting at several different wavelengths. Compared to the bandpasses of the filters, these lines are very narrow and can be represented as delta functions. If λ_i is the wavelength for the emission line to be observed, then N_λ can be represented as,

$$N_\lambda \approx \delta(\lambda - \lambda_i)\phi_i \tag{A.3}$$

where ϕ_i is the flux rate of that line in photons cm^{-2} sec^{-1}. Applying A.1 to the system will result in,

$$\phi_i^{exp} = T(\lambda_i)\phi_i \tag{A.4}$$

where ϕ_i^{exp} is the expected flux for the emission of wavelength λ_i. By the same arguments, the number of counts and the expected flux should be related linearly by α, and so,

$$C = \alpha T(\lambda_i)\phi_i \tag{A.5}$$

For an optically thin cloud of emitters at a distance r, the flux rate is given by,

$$\phi_i = \frac{N\epsilon_i}{4\pi r^2} \tag{A.6}$$

where ϵ_i is the emission rate in photons per ion per second for that emission line and N is the number of emitters within the field of view of the camera.

For ion inventories the number of interest is the number of ions in the cloud.

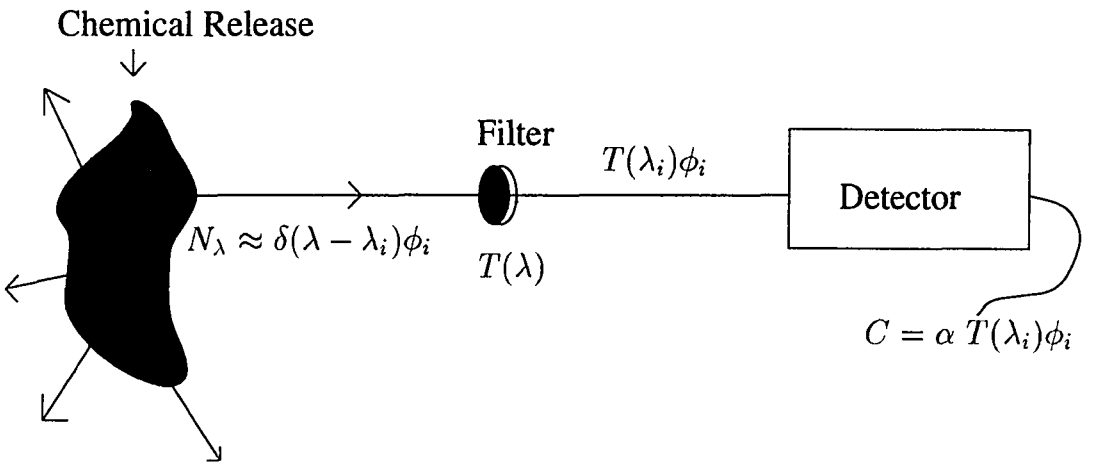

Figure A.2: Ion Inventory. Application of α from the star calibration to an ion inventory is shown.

Rearranging A.6 to get N results in,

$$N = \frac{\phi_i}{\epsilon_i} 4\pi r^2 \tag{A.7}$$

Rearranged A.5 for ϕ_i and inserting into A.7 results in,

$$N = \frac{C}{\alpha T(\lambda_i)\epsilon_i} 4\pi r^2 \tag{A.8}$$

For unfiltered cameras, the filter shown in the figures will be replaced by the normalized spectral response of the camera. The flux ϕ^{exp} will be slightly different, call it $\hat{\phi}^{exp}$, and the resulting linear relationship between the counts and expected flux, α will also be slightly different. However, when applied to the emissions from the same image the results will measure the same quantities.

Difficulties arise when there are multiple emissions that are imaged at any one time. If the relative emission rates are known, the calculation of N can be attempted, but if the emission rates are not known, then the calculations will rely on reasonable assumptions.

Bibliography

Abe, T. and S. Machida, Production of high-energy electrons caused by counter-streaming ion beams in an external magnetic field, *Phys of Fluids*, *28*, 1178–1185, 1985.

Aleksakhin, I. S., I. I. Garga, I. P. Zapesochnii, and V. P. Starodub, Electron impact excitations of alkaline earth atoms. III Strontium (triplets), *Opt. Spectrosc. (USSR)*, *37*, 10–12, 1974.

Aleksakhin, I. S., I. P. Zapesochnii, I. I. Garga, and V. P. Starodub, Excitation of alkaline-earth atoms by electron impact. 5: Barium, *Opt. Spectrosc. (USSR)*, *38*, 126–129, 1975.

Alfvén, H., *On the origin of the solar system.* Oxford University Press, 1954.

Baumback, M. M., P. Rodriguez, D. N. Walker, and C. L. Siefring, LASSII pulsed plasma probe on CRRES, *J. Spacecraft Rockets*, *29*, 607–608, 1992.

Bernhardt, P. A., Probing the magnetosphere using chemical releases from the Combined Release and Radiation Effects Satellite, *Phys of Fluids B*, *4*, 2249–2256, 1992.

Bernhardt, P. A., J. D. Huba, M. B. Pongratz, D. J. Simons, and J. H. Wolcott, Plasma irregularities caused by cycloid bunching of the CRRES G-2 barium release, *J. Geophys. Res.*, *98*, 1613–1627, 1993.

Biasca, R., D. Hastings, and D. Cooke, Upper bound estimates of anomalous ion production in space-based critical ionization velocity experiments, *J. Geophys. Res.*, *98*, 17569–17581, 1993.

Blifford, I. H., Factors affecting the performance of commercial interference filters, *Applied Optics*, *5*, 105–111, 1966.

Boulmer, J., P. Camus, J.-M. Gagné, and P. Pillet, Laser-microwave ionisation mass spectroscopy of ion Rydberg states: Ba^+ spectrum, *J. Phys. B*, *20*, L143–L147, 1987.

Brenning, N., Review of the CIV phenomenon, *Space Sci. Rev.*, *59*, 209–314, 1992.

Brush, S. G., Prediction and theory evaluation: Alfvén on space plasma phenomena, *EOS*, *71*, 19–33, 1990.

Carlsten, J. L., Photoionization of barium clouds via the ^3D metastable levels, *Planet. Space Sci.*, *23*, 53–60, 1975.

Chamberlain, J. W. and D. M. Hunten, *Theory of Planetary Atmospheres, 2nd Edition.* Academic Press, San Diego, 1987.

Chen, S. T. and A. Gallagher, Excitation of the Ba and Ba^+ resonance lines by electron impact on Ba atoms, *Phys. Rev. A*, *14*, 593–601, 1976.

Danielsson, L., Review of the critical velocity of gas-plasma interaction I: experimental observations, *Astrophys. Space Sci.*, *24*, 459–485, 1973.

Deehr, C. S., E. M. Wescott, H. C. Stenbaek-Nielsen, G. J. Romick, T. J. Hallinan, and H. Föppl, A critical velocity interaction between fast barium and strontium ions in the terrestrial ionospheric plasma, *Geophys. Res. Lett.*, *9*, 195–198, 1982.

Delamere, P. A., H. C. Stenbaek-Nielsen, D. L. Hampton, and E. M. Wescott, Optical observations of the early ($t < 5$ s) ion dynamics of the CRRES G1, G9 and G11A releases, Submitted to *J. Geophys. Res.*, 1995.

Djerad, M. T., Atomic parameters for transitions involving Rydberg states of singly ionized alkaline earths, *Journal de Physique II*, *1*, 1–9, 1991.

Drapatz, S. W., The radiative transfer problem in freely expanding gaseous clouds and its application to barium cloud experiments, *Planet. Space Sci.*, *20*, 663–682, 1971.

Eather, R. H. and D. L. Reasoner, Spectrophotometry of faint light sources with a tilting-filter photometer, *Applied Optics*, *8*, 227–242, 1969.

Firsov, O. B., Stripping cross sections, *JETP*, *9*, 1076, 1959.

Fite, W. L., T. A. Patterson, and M. W. Siegel, Cross sections for thermal reactions between uranium atoms and atmospheric species, Technical Report AFGL-TR-77-0030, Air Force Geophys. Lab., Hanscom Air Force Base, Mass., 1977.

Fleishmann, H. H., R. C. Dehmel, and S. K. Lee, Direct-transition features in stripping collisions of heavy neutral atoms and ions, *Phys. Rev. A*, *5*, 1784–1798, 1972.

Frieden, B. R., *Probability, Statistical Optics, and Data Testing.* Springer Verlag, New York, 1991.

Garga, I. I., I. S. Aleksakhin, V. P. Starodub, and I. P. Zapesochnii, Electron impact excitation of alkaline earth atoms iv: calcium, *Opt. Spectrosc. (USSR)*, *37*, 482–485, 1974.

Goertz, C. K., S. Machida, and G. Lu, On the theory of CIV, *Astrophys. Space Sci.*, *10*(7), 33–45, 1990.

Haerendel, G., Alfvéns critical velocity effect tested in space, *Z. Naturforsch.*, *37*, 728–735, 1982.

Hallinan, T. J., Observed rate of ionization in shaped-charge releases of barium in the ionosphere, *J. Geophys. Res.*, *93*, 8705–8712, 1988.

Hedin, A. E., MSIS-86 thermospheric model, *J. Geophys. Res.*, *92*, 4649–4662, 1987.

Hoch, E. L. and T. J. Hallinan, Measurements of time constant for steady ionization in shaped-charge barium releases, *J. Geophys. Res.*, *98*, 7765–7773, 1993.

Huba, J. D., P. A. Bernhardt, and J. G. Lyon, Preliminary study of CRRES magnetospheric barium release, *J. Geophys. Res.*, *97*, 11–24, 1992.

Hunton, D. E., Charge transfer reactions of metastable Ba(I) and Sr(I) in the CRRES G-11B chemical release experiment, *Geophys. Res. Lett.*, *22*, 2115–2118, 1995.

Jacoby, G. H., D. A. Hunter, and C. A. Christian, A library of stellar spectra, *Astrophy. J. Supplementary Series*, *56*, 257–281, 1984.

Kallenback, A., M. Kock, and G. Zierer, Absolute cross sections for photoionization of laser-excited BaI states measured on a thermionic diode, *Phys. Rev. A*, *38*, 2356–2360, 1988.

Kelley, M. C., *The Earth's Ionosphere.* Academic Press, San Diego, 1989.

Kostelecký, V. A. and M. M. Nieto, Analytic wave functions for atomic quantum-defect theory, *Phys. Rev. A*, *32*, 3243–3246, 1985.

Lai, S., W. J. McNiel, and E. Murad, The role of metastable states in critical ionization velocity discharges, *J. Geophys. Res.*, *93*(6), 5871–5878, 1988.

Lai, S. T., E. Murad, and W. J. McNiel, An overview of atomic and molecular processes in critical velocity ionization, *IEEE Trans. on Plasma Science*, *17*, 124–134, 1989.

Lai, S. T., E. Murad, and W. J. McNiel, Amplification of critical velocity ionization by associative ionization, *J. Geophys. Res.*, *97*, 4099–4107, 1992a.

Lai, S. T., W. J. McNiel, and E. Murad, The importance of seed ionization in CIV space experiments, *Cambridge Workshop in Theoretical Geoplasma*, *0*, 1–2, 1992b.

Liou, K. and R. B. Torbert, On Ba^+ production in the CRIT II experiment, *J. Geophys. Res.*, *100*, 5811–5818, 1995.

Liu, B. and R. E. Olson, Potential energies for Ca_2^+ : Cross sections for collisions of Ca^+ and Rydberg Ca^{**} with Ca, *Phys. Rev. A*, *18*, 2498–2505, 1978.

Lyon, I. C., B. Peart, J. B. West, and K. Dolder, Measurement off absolute cross section for the photoionisation of Ba^+ ions, *J. Phys. B*, *19*, 4137–4145, 1986.

Machida, S. and C. K. Goertz, A simulation study of the critical ionization velocity process, *J. Geophys. Res.*, *91*, 11,965–11976, 1986.

Machida, S. and C. K. Goertz, The electromagnetic effect on the critical ionization process, *J. Geophys. Res.*, *93*, 11,495–11,506, 1988.

Machida, S., T. Abe, and T. Terasawa, Computer simulation of critical velocity ionization, *Phys of Fluids*, *27*, 1928–1931, 1984.

McNiel, W. J., S. T. Lai, and E. Murad, Interplay between collective and collisional processes in critical velocity ionization, *J. Geophys. Res.*, *95*, 10,345–10,356, 1990.

Miles, B. M. and W. L. Wiese, Critical evaluation of transitions probabilities for Ba I and Ba II, *Atomic Data*, *1*, 1–17, 1969.

Milinevsky, G. P., A. I. Kashirin, Y. A. Romanovsky, H. C. Stenbaek-Nielsen, and M. C. Kelley, Long-lived artificial ion clouds in the Earth's ionosphere, *JGR*, *20*, 1019–1022, 1993.

Möbius, E., Critical velocity experiments in space, in *Active experiments in space*. 1983.

Moghaddham-Taaheri, E. and C. K. Goertz, Numerical quasi-linear study of the critical ionization velocity phenomenon, *J. Geophys. Res.*, *98*, 1443–1460, 1993.

Moore, C. E., *Atomic Energy Levels: As Derived From the Analyses of Optical Spectra*. National Bureau of Standards – Circular #467, 1958.

Murad, E., The role of atomic and molecular processes in the critical ionization effect, in A. E. Kingston (ed.), *Recent Studies in Atomic and Molecular Processes*, pp. 79–90. Plenum Press, New York, NY, 1987.

Murad, E. and S. Lai, Effect of dissociative electron-ion recombination on the propagation of critical ionization discharges, *J. Geophys. Res.*, *91*, 13745–13749, 1986.

Newell, P. T. and R. B. Torbert, Competing atomic processes in Ba and Sr injection critical velocity experiments, *Geophys. Res. Lett.*, *12*, 835–838, 1985.

Peddie, N. W., International geomagnetic reference field: the third generation, *J. Geomag. Geoelec.*, *34*, 309–326, 1982.

Person, J. C., D. Resendes, H. Petschek, and D. E. Hastings, Effects of collisional processes on the critical velocity hypothesis, *J. Geophys. Res.*, *94*, 4039–4055, 1990.

Phaneuf, R. A., Experiments on electron-impact excitation and ionization of ions, in F. Brouillard (ed.), *Atomic Processes in Electron-Ion and Ion-Ion Collisions*, pp. 117–156. Plenum Press, New York, 1985.

Rapp, D. and W. E. Francis, Charge exchange between gaseous ions and atoms, *J. Chem. Phys.*, *37*, 2631–2645, 1962.

Rapp, D. and I. B. Ortenburger, Interchange of charge between gaseous molecules, *J. Chem. Phys.*, *33*, 1230–1233, 1960.

Reasoner, D. L., Chemical-release mission of CRRES, *J. Spacecraft Rockets*, *29*, 580–584, 1992.

Rees, D., I. McWhirter, P. A. Rounce, and F. E. Barlow, Miniature imaging photon detectors II. Devices with transparent photocathodes, *J. Phys. E Sci. Instruments*, *14*, 229–233, 1981.

Rees, M. H., *Physics and Chemistry of the Upper Atmosphere*. Cambridge University Press, Cambridge, 1989.

Reuther, J. J. and H. B. Palmer, Identification of the the many-line visible emissions spectrum of BaO, *JCP*, *77*, 83–91, 1982.

Ringer, G. and W. R. Gentry, A merged molecular beam study of the endoergic associative ionization reaction $N(^2D) + O(^3P) \rightarrow NO^+ + e$, *J. Chem. Phys.*, *71*, 1902–1909, 1979.

Rutherford, J. A., R. F. Mathis, B. R. Turner, and D. A. Vroom, Formation of calcium ions by charge transfer, *J. Chem. Phys.*, *57*, 3087–3090, 1974.

Rybicki, G. B. and A. P. Lightman, *Radiative Processes in Astrophysics*. Wiley Interscience, New York, 1979.

Schild, R. E., Interstellar reddening law, *Astrophy. J.*, *82*, 337–344, 1977.

Shpenik, O. B., A. N. Zavilopulo, and I. P. Zapeochnyi, Inelastic collisions of slow alkali or alkaline-earths ion with cadmium atoms, *JETP*, *35*, 466–471, 1972.

Smithsonian Astrophysical Observatory, *Star Atlas of Reference Stars and Nonstellar Objects*. MIT Press, Cambridge Massachusetts, 1969.

Sramek, S. J., Something to do with Sr charge exchange, *Phys. Rev. A*, *22*, 2630, 1980.

Starodub, V. P., I. S. Aleksakhin, I. I. Garga, and I. P. Zapesochnii, Electron impact excitations of alkaline earth atoms. Part 2: Strontium singlets, *Opt. Spectrosc. (USSR)*, *35*, 603–606, 1973.

Stenbaek-Nielsen, H. C., Calculated emission rates for barium releases in space, *Planet. Space Sci.*, *37*, 1441–1452, 1989.

Stenbaek-Nielsen, H. C., E. M. Wescott, D. Rees, A. Valenzuela, and N. Brenning, Non-solar UV produced ions observed optically from the CRIT I critical velocity ionization experiment, *J. Geophys. Res.*, *95*, 7749–7757, 1990a.

Stenbaek-Nielsen, H. C., E. M. Wescott, G. Haerendel, and A. Valenzuela, Optical observations on the CRIT-II critical ionization velocity experiment, *Geophys. Res. Lett.*, *17*, 1601–1604, 1990b.

Stenbaek-Nielsen, H. C., E. M. Wescott, and T. J. Hallinan, Observed barium emission rates, *J. Geophys. Res.*, *98*, 17,491–17,500, 1993.

Stokes, C., Report on crres thermite chemical release cannisters, Technical report, Ball Aerospace, 1989.

Swenson, G. R., S. B. Mende, R. E. Meyerott, and R. L. Rairden, Charge exchange contamination of CRIT-II barium CIV experiment, *Geophys. Res. Lett.*, *18*, 401–403, 1991.

Szuszczewicz, E. P., G. Earle, T. Bateman, Z. Klos, A. Kiraga, and R. W. Schunk, An *in situ* investigation of early-time multi-ion expansion processes in an F-Region chemical release, Submitted to *J. Geophys. Res.*

Tanaka, M. and K. Papadopoulos, Creation of high-energy electron tails by means of the modified two-stream instability, *Phys of Fluids*, *26*, 1697–1699, 1983.

Taylor, P. O. and G. H. Dunn, Absolute cross sections and polarization for electron-impact excitation of the *K* and *H* resonance lines of the Ca^+ ion, *Phys. Rev. A*, *8*, 2304–2321, 1973.

Torbert, R. B., M. Kletzing, and K. Liou, Prompt ionization in the CRIT II barium releases, *Geophys. Res. Lett.*, *19*, 973–976, 1992.

Vampola, A. L., Combined Release and Radiation Effects Satellite, *J. Spacecraft Rockets*, *29*, 555, 1992.

Vaĭnshteĭn, L. A., V. I. Ochkur, V. I. Rakhovskiĭ, and A. M. Stepanov, Absolute values of electron impact ionization cross section for magnesium, calcium, and barium, *JETP*, *34*, 271–275, 1972.

Wescott, E. M., H. C. Stenbaek-Nielsen, T. Hallinan, H. Föppl, and A. Valenzuela, Star of Condor: a strontium critical velocity experiment, Peru, 1983, *J. Geophys. Res.*, *91*, 9933–9938, 1986a.

Wescott, E. M., H. C. Stenbaek-Nielsen, T. J. Hallinan, H. Föppl, and A. Valenzuela, Star of Lima: overview and optical diagnostics of a barium Alfvén critical velocity experiment, *J. Geophys. Res.*, *91*, 9923–9931, 1986b.

Wescott, E. M., H. C. Stenbaek-Nielsen, D. W. Swift, A. Valenzuela, and D. Rees, SR90, strontium shaped-charge critical ionization velocity experiment, *J. Geophys. Res.*, *95*, 21,069–21,075, 1990.

Wescott, E. M., H. C. Stenbaek-Nielsen, and D. L. Hampton, Xenon critical velocity releases from the ACTIVNY satellite: discussion of attempted optical observations, *Geophys. Res. Lett.*, *19*, 2079–2081, 1992.

Wescott, E. M., H. C. Stenbaek-Nielsen, D. L. Hampton, and P. A. Delamere, Results of critical velocity experiments with barium, strontium and calcium releases from CRRES satellite, *J. Geophys. Res.*, *99*, 2145–2158, 1994.

Zapesochnyi, I. P., V. A. Kel'man, A. I. Imre, A. I. Dashchenko, and F. F. Danch, Excitation of the Mg^+, Ca^+, Sr^+, and Ba^+ resonance levels in electron-ion collisions, *JETP*, *42*, 989–992, 1976.